Hydrological impact of Middle Miocene Antarctic ice-free areas coupled to deep ocean temperatures

Catherine D. Bradshaw[1,2,3,4], Petra M. Langebroek[5], Caroline H. Lear[6], Daniel J. Lunt[3], Helen K. Coxall[4], Sindia M. Sosdian[6], Agatha M. de Boer[4]

[1]Met Office Hadley Centre, Fitzroy Road, Exeter EX1 3PB, UK

[2]The Global Systems Institute, University of Exeter, North Park Road, Exeter, EX4 4QE

[3]BRIDGE, School of Geographical Sciences, University of Bristol, Bristol BS8 1SS, UK

[4]Department of Geological Sciences, Stockholm University, SE-106 91, Stockholm, Sweden;

[5]NORCE Norwegian Research Centre, Bjerknes Centre for Climate Research, 5007 Bergen, Norway;

[6]School of Earth and Ocean Sciences, Cardiff University, Main Building, Park Place, Cardiff, CF10 3AT, UK

catherine.bradshaw@metoffice.gov.uk

Oxygen isotopes from ocean sediments ($\delta^{18}O$) used to reconstruct past continental ice volumes additionally records deep water temperatures (DWT). Traditionally, these are assumed to be coupled (ice volume changes cause DWT changes). However, $\delta^{18}O$ records during peak mid-Miocene warmth (~16-15 Ma) document large rapid fluctuations (~1-1.5 ‰) difficult to explain as huge Antarctic ice sheet (AIS) volume changes. Here, using climate modelling and data comparisons, we show DWTs are coupled to AIS spatial extent, not volume, because Antarctic albedo changes modify the hydrological cycle, affecting Antarctic deep-water production regions. We suggest the mid-Miocene AIS had retreated significantly from previous Oligocene maxima. The residual ice sheet varied spatially more

rapidly on orbital timescales than previously thought, enabling large DWT swings (up to 4°C). When mid-Miocene warmth terminated (~13 Ma) and a continent-scale AIS had stabilized, further ice volume changes were predominantly in height rather than extent, with little impact on DWT. Our findings imply a shift in ocean sensitivity to ice sheet changes occurs when AIS retreat exposes previously ice-covered land; associated feedbacks could reduce the Earth system's ability to maintain a large AIS. This demonstrates ice sheet changes should be characterized not only by ice volume, but also spatial extent.

Knowledge of Earth's glacial history and evolution through past warm periods is crucial for understanding cryosphere dynamics and future ice sheet stability. However, the magnitude and timing of ice sheet variations remains uncertain, even for the largest Cenozoic shifts[1]. Glacial history is commonly reconstructed from the oxygen isotope composition of fossil calcareous benthic foraminifera shells ($\delta^{18}O_c$), a proxy for seawater temperature and ice volume[2]. A rapid coeval increase in global $\delta^{18}O_c$ records is indicative of major ice growth events. Over the last 40 million years, rapid expansion of the Antarctic ice sheet (AIS) during the middle Miocene Climatic Transition (MMCT; ~14-13.8 Ma)[3] stands out as one of the three periods of major ice growth in the $\delta^{18}O_c$ record[1].

The MMCT is particularly fascinating because of the hypothesized transition from a less stable small wet-based AIS[4] where meltwater encourages basal sliding and fast moving ice, to a more stable large dry-based AIS where the base is frozen to the bedrock[5]. The major ice growth event is well marked in palaeorecords by a ~1‰ increase in $\delta^{18}O_c$ (Fig. 1), and thereafter $\delta^{18}O_c$ values have remained at, or above, these levels to the present day[1] because a climatic threshold was crossed[6]. From $\delta^{18}O_c$, inferred MMCT ice growth is equivalent to the size of the entire present day AIS, or larger[7–11], but ice sheet isotopic composition changes accounts for some of the amplitude[12,13]. Sequence stratigraphic estimates of sea level (independent from $\delta^{18}O_c$) indicate ~20-60 m changes[14–17]. Previous studies conclude this magnitude of ice growth implies the pre-MMCT AIS volumes must have been very small[18,19]. There is little evidence for notable contemporary Northern Hemisphere glaciation[20] and although Antarctic topography has changed with time because of tectonics, isostatic adjustments and glacial erosion, topographic changes likely account for ~8 m sea level equivalent (S.L.E.) greater magnitude of ice growth for the same forcing[13], leaving an additional 12-52 m necessary to explain observations.

In stark contrast to the MMCT glaciation, the preceding Miocene Climatic Optimum (MCO; ~16.8-14.8 Ma) contains the lowest $\delta^{18}O_c$ values of the last 25 million years and fossil evidence for significant tundra and woody Antarctic vegetation[21,22]; thereby the globally warmest period/least amount of continental ice. Evidence points to a much reduced size of the dynamic wet-based AIS in the MCO, compared with its early Oligocene counterpart[14–17] and large amplitude $\delta^{18}O_c$ fluctuations combined with sea level estimates imply a highly dynamic cryosphere (Fig. 1, Extended Data Fig. 1).

Differing ice growth-deep water temperature relationships

Some key observations from the mid Miocene Antarctic cryosphere still require explanation. There is a long-held assumption that continental ice volume is inherently coupled to deep water temperatures (DWT) because expanding ice sheets are assumed to cool high latitude regions of deep convection[1,3,23]. We would therefore expect both the MCO and MMCT to be associated with DWT changes, yet the $\delta^{18}O_c$ record, combined with independent temperature reconstructions (Fig. 1), reveals some challenging observations. During the MCO, both $\delta^{18}O_c$ and DWT were highly variable (70% of $\delta^{18}O_c$ variability attributed to changes in DWT[24]). During the MMCT,

$\delta^{18}O_c$ was highly variable but DWT variations reduced in amplitude. During the MMCT glaciation, $\delta^{18}O_c$ was highly variable but DWT variations were small (70% of the $\delta^{18}O_c$ variability attributed to changes in ice volume[24,25]). After the MMCT, $\delta^{18}O_c$ and DWT were variable, but less variable than during the MCO.

Interpreting $\delta^{18}O_c$ is complicated because both temperature and the ambient seawater isotopic composition ($\delta^{18}O_{sw}$) are recorded. $\delta^{18}O_{sw}$ itself is dependent on global continental ice volume, the isotopic composition of this ice, and localized salinity effects[26]. Paired independent reconstructions can isolate the temperature signal and analysis of spatially distributed $\delta^{18}O_c$ records can reduce the salinity component. However, for the MMCT glaciation there remains the observation of a large ice increase but little DWT cooling, raising the question: if there is a strong coupling between ice volume and DWT as assumed[1,3,23], why did DWT vary so much less during the MMCT when ice sheet growth was most rapid? Here we present new climate model results assessing the impact of ice sheet size on DWT across the MCO and MMCT. Our results confirm the findings of a previous modelling study that DWT is insensitive to ice sheet growth at the MMCT[27]. While the previous study explains the MMCT ice volume-DWT decoupling in terms of strong feedbacks in the coupled atmosphere-ocean-sea ice system[27], our study provides further mechanistic understanding of the differing degrees of middle Miocene ice volume-DWT coupling by proposing a key role for the hydrological cycle. We here advance our understanding of the paradigm by highlighting the important role, not only of ice sheet volume, but also of spatial ice sheet coverage in determining the DWT response to glaciation, during the MMCT and the MCO.

We use a fully coupled atmosphere-ocean-vegetation general circulation model, HadCM3LB-M2.1a[28] configured with middle Miocene palaeogeography (see Methods and Fig. 2). For our initial assessment using preindustrial CO_2 concentrations, we find that AIS expansion from

ICE_{FREE} to ICE_{PART}22m and from ICE_{PART}22m to ICE_{FULL}55m reduces DWT by ~0.5°C for each step, thus here ice growth and DWT are coupled (Fig. 3a). However, AIS expansion from ICE_{FULL}55m to ICE_{FULL}90m does not cause further deep ocean cooling (in contrast a slight temperature increase is seen), thus here ice growth and DWT are decoupled (ice volume changes do not affect DWT).

We propose that coupling between ice sheet volume and DWT only occurs until the ice sheet reaches the coast because the ice-albedo feedback mechanism and vegetation-climate interactions invoke additional feedback processes identified here for the first time. To demonstrate it is ice sheet spatial extent (rather than height/volume) that is coupled to DWT, we carry out a non-realistic sensitivity study imposing AIS configurations spanning extreme endmembers from ice-free to ice-covered but keep ice volume constant. We assume the ice sheet is of "skin-thickness" (no effective change in elevation as compared to the ice-free state, nominally 1 m S.L.E when fully ice-covered; "ICE_{FULL}1m"), and vary the ice extent longitudinally, latitudinally and topographically. We use preindustrial CO_2 concentrations throughout and conduct an additional high CO_2 sensitivity test (~850 ppm; Fig. 4). Combining our results, we find a strong relationship between ice-free extent and DWT, with no evidence of non-linearity (Fig. 3b).

The mechanism linking ice cover to deep water temperatures

Our modelling results suggest summertime "ice-free" Antarctica (ICE_{FREE}, Fig 3, column 1) would be warm and wet, because the land-sea thermal contrast drives monsoon winds, which transport moisture into the Antarctic continental interior from the Southern Ocean (Fig. 5a-c). This moisture falls over the relatively warm continent as rain, not snow, during the summer months (Fig. 5b), and over much of the continent during the winter months for the two highest

CO_2 scenarios. Summertime Antarctic temperatures and precipitation are similar to proxy reconstructions for a vegetated Antarctica[4,21,22,29–31]. A comprehensive model-data comparison (Supplementary Note) indicates peak CO_2 would need to be > 850 ppm for a complete overlap with proxy reconstructions, in agreement with recent MCO reconstructions[32]. ICE_{FREE} also results in the warmest freshest deep ocean of all the simulations (Fig. 5d-e). Surface runoff from the active hydrologic cycle, being less saline and thus less dense than the seawater it drains into, forms a polar halocline at the surface. This halocline reduces ventilation of the deep ocean (Fig. 5d), weakening overturning. In our simulations, deep water is in all cases primarily produced in the Southern Ocean, thus DWTs are determined by southern sinking regions. Antarctic Bottom Water (AABW) production never ceases completely in the model for any scenario (Supplementary Discussion B).

In ICE_{FULL}1m, ICE_{FULL}55m and ICE_{FULL}90m (Fig 3, columns 3-5), cold surface temperatures near the ice sheet and the large increase in albedo causes localized radiative cooling of the air column and a reduction in vapour holding capacity. The land-sea thermal contrast reduces (Fig. 5a) and the summer monsoon system ceases to operate. Katabatic winds form as the cold dense air flows away from the elevated areas towards the coast (Fig. 5c). The interaction between the winds and sea-ice is complex and dependent upon background CO_2 (Fig. 5b; Supplementary Discussion A). Reduced precipitation (Fig. 5b) and subsequent runoff reduces ocean stratification (Fig. 5d), permitting the cold surface waters to sink more freely from the continental shelf into the abyss (Fig. 5e). Increased AABW production invigorates ocean ventilation.

Empirical studies show a clear relationship between ice sheet volume and spatial extent[33], implying ice sheet thickness is limited by spatial extent. Therefore, in order to grow vertically, an ice sheet must also grow spatially (Supplementary Discussion C). After the ice sheet reaches the ocean, additional growth is necessarily predominantly vertical. Although a thickening ice sheet is accompanied by further cooling and drying of the air, this does not significantly affect runoff because precipitation has already been reduced to a low level and is falling as snow, not rain. Consequently, the surface ocean salinity does not change much and hence neither does deep water production, ocean ventilation or, crucially, DWT. This explains the ice volume-DWT decoupling between ICE_{FULL}1m, ICE_{FULL}55m and ICE_{FULL}90m. The global mean DWTs begin to rise slowly as ice volume (height) increases (in the absence of CO_2 changes) because the higher topography reduces the amount of summertime low clouds around the Antarctic coastline by 10-15% (not shown), allowing more solar radiation to reach the surface and reducing sea ice, which locally causes greater absorption of solar radiation into the ocean.

Our model has a fairly linear response to both a gradually increasing and decreasing ice sheet extent. However, we note in a dynamic ice sheet model, ice-melt in the decreasing ice sheet scenario would result in additional surface runoff that would likely impact AABW production, at least temporarily, as demonstrated in a studies of the modern AIS[34].

Sensitivity to atmospheric CO_2 and orbit

Our model does not have an interactive AIS, so the response of the ice sheet to CO_2 forcing is not included and our study is limited to a single model with mid-range CO_2 sensitivity[35]. However, our results show that atmospheric CO_2 has a much smaller impact on the hydrological regime than ice sheet configuration (Supplementary Discussion A). CO_2 impacts sea-ice extent and sea surface temperatures which in turn affect the deeper layers via vertical mixing, in a process that is complex and non-linear (Supplementary Discussion A).

For the MCO, the most recent CO_2 record suggests an average range of concentrations between 630 and 470 ppm[32]. Using the relationship between CO_2 and DWT calculated from our simulations, we infer a consequent ~0.8 °C mean temperature change in the 2-3 km deep layer in the Southern Hemisphere (Fig. 6), which is about 80% of the ~1.0 °C impact from increasing ice-extent (Fig. 3, ICE_{FULL}1m - ICE_{FREE}) in the same layer. This provides a picture of the average DWT changes. The site-specific temperature changes (of 2-4 °C, Fig. 1), will depend also on local dynamics. At Site 761, our simulations estimate a contribution of 0.5 °C from CO_2 variations compared to a 0.9-1.9 °C contribution from ice extent changes, and at Site 1171, the contribution from CO_2 is between 0.5-0.6 °C compared to 1.0-1.5 °C from ice extent (Supplementary Discussion D and E). Our results show that CO_2 changes alone cannot explain the observed DWT range at the MCO and moreover, for both the mean layer and the specific sites, our model suggests that ice-extent had a larger impact on DWT than CO_2. For the MMCT glaciation, the most recent CO_2 reconstructions show at most a 170 ppm reduction from ~570 to 400 ppm[32], for which we infer from our ice-covered model simulations a temperature drop of 0.5–0.8 °C at the two sites (Supplementary Discussion E). This is consistent with the reconstructions (Fig. 1) if we assume Antarctica was ice-covered prior to the MMCT glaciation (i.e. little DWT change occurred as a result of increasing ice sheet extent). In the absence of ice sheet changes, we find a minimal effect of orbital configuration on DWT (Supplementary Discussion F).

From thin and vulnerable to thick and established

We introduce the hydrological cycle as a crucial mechanism mediating the link between the DWT and the ice spatial extent (rather than absolute volume), thus explaining the different degrees of coupling between ice sheet changes and DWT during the MMCT and MCO.

Our new results lead us to propose that DWT varied by up to 4°C during the MCO because the spatial extent of ice and vegetation rapidly altered. Taken together with existing $\delta^{18}O_c$, temperature, vegetation and CO_2 reconstructions, this implies the AIS had retreated significantly during the MCO, when average CO_2 concentrations were likely 470-630 ppm, reaching 780-1100 ppm at times[32]. Previous work clearly demonstrates the dynamic behaviour of a small AIS when driven by CO_2 changes combined with orbital forcing[7]. How far exactly the ice sheet retreated during these warmest intervals, however, is unknown. Ice sheet modelling suggests a retreat exposing 60-70% of the Antarctic land surface is consistent with the paleorecord[13]. Other work concludes a retreat even greater than this[36,37], perhaps even ice-free[11]. The evidence for vegetation, including trees, growing on the continent throughout the MCO[22,29] implies both warm and wet conditions, and it is suggested the moisture supply derived from the Southern Ocean[29]. To achieve this, our results indicate a greater reduction of ice is needed than the ICE_{PART}22m scenario ice sheet extent, because the Wilkes Land winds are directed landward in ICE_{FREE}, but seaward for ICE_{PART}22m (Figure 3c). We suggest these monsoon moisture-carrying winds induced by spatial ice retreat could provide an explanation for major ice advance onto the continental shelf in the Ross Sea[38,39] during the MCO occurring at the same time as open water and woody vegetation in the Wilkes Land[22] (Supplementary Discussion G).

We further infer DWT varied so much less during the MMCT when the AIS volume was growing rapidly because it had already extended to cover most of the continent prior to the major ice growth event, in agreement with previous findings[27]. Thus, the ice sheet subsequently increased mainly in thickness, not area, and so DWTs were largely unaffected because, without the additional ice-albedo feedback, changes to the hydrological cycle were much smaller. Post-MMCT (label 1 in Fig. 1), both $\delta^{18}O_c$ and DWT are variable, but less so than during the MCO.

The exact degree of coupling, and its mechanism, needs to be explored in a model set-up that includes marine-based ice sheets and ice shelves, not included in this study. However, the physical limits on seawater temperatures (-1.8°C) will set the lower boundary on possible temperature changes as climate cools.

Interpretation of our results leads us to support a highly dynamic MCO AIS, and state, alongside CO_2, it was changes in ice sheet area and proximity to the coast, not volume, that were of key importance for global DWTs. This fundamentally changes the way we should characterize ice sheet changes and how we must view the long-term $\delta^{18}O_c$ records spanning greenhouse-icehouse transitions. In the absence of independent temperature proxies, it must not be assumed that DWTs scale with ice volume changes.

Whilst we do not propose the MCO Antarctica was ever completely ice-free, our results demonstrate any spatial retreat of the AIS can increase precipitation causing associated warming of the deep ocean - changes perhaps having the ability to both accelerate ice melt of ice shelves and glaciers through hydrofracturing from increased precipitation falling into cravasses[40,41] and to accelerate ice melt of marine-based subglacial basins[34,41]. Although the temperature changes resulting from changing ice sheet extent are similar to those resulting from CO_2 changes, our study does not include feedbacks to the carbon cycle or to the ice sheet itself and therefore the significance of our results could be greater than indicated here. Our non-realistic sensitivity studies using only a skin-thickness of ice demonstrate the importance of both surface albedo and roughness for a hydrologic control on DWT evolution. It is therefore possible that our mechanism could operate in areas even without complete ice-loss if these two factors change significantly. For example: in regions of debris-covered glaciers, rock glaciers, vegetation-covered rock glaciers and “glacier mice”, which all increase in the context of retreating ice glaciers[42–45], in regions of accumulating dark particles (dust and soot)[46] and in regions of glacier algae, which bloom in supraglacial meltwater[47].

References

1. Zachos, J., Pagani, M., Sloan, L., Thomas, E. & Billups, K. Trends, rhythms, and aberrations in global climate 65 Ma to present. *Science.* **292**, 686–693 (2001).

2. Chappell, J. & Shackleton, N. Oxygen isotopes and sea level. *Nature* **324**, 137 (1986).

3. Shackleton, N. J. & Kennett, J. P. Paleotemperature history of the Cenozoic and the initiation of Antarctic glaciation: oxygen and carbon isotope analyses in DSDP Sites 277,279, and 281. *Initial Reports of Deep Sea Drilling Project* **29**, (U.S. Government Printing Office, 1975).

4. Lewis, A. R. *et al.* Mid-Miocene cooling and the extinction of tundra in continental Antarctica. *Proc. Natl. Acad. Sci.* **105**, 10676–10680 (2008).

5. Kleman, J. & Glasser, N. F. The subglacial thermal organisation (STO) of ice sheets. *Quat. Sci. Rev.* **26**, 585–597 (2007).

6. Levy, R. H. *et al.* Antarctic ice-sheet sensitivity to obliquity forcing enhanced through ocean connections. *Nat. Geosci.* **12**, 132–137 (2019).

7. Langebroek, P. M., Paul, A. & Schulz, M. Antarctic ice-sheet response to atmospheric CO_2 and insolation in the Middle Miocene. *Clim. Past* **5**, 633–646 (2009).

8. Lear, C. H., Mawbey, E. M. & Rosenthal, Y. Cenozoic benthic foraminiferal Mg/Ca and Li/Ca records: Toward unlocking temperatures and saturation states. *Paleoceanography*

25, (2010).

9. Lear, C. H. *et al.* Neogene ice volume and ocean temperatures: Insights from infaunal foraminiferal Mg/Ca paleothermometry. *Paleoceanography* **30**, 1437–1454 (2015).

10. de Boer, B., van de Wal, R. S. W., Lourens, L. J. & Bintanja, R. Transient nature of the Earth's climate and the implications for the interpretation of benthic $\delta^{18}O$ records. *Palaeogeogr. Palaeoclimatol. Palaeoecol.* **335**, 4–11 (2012).

11. Miller, K. G. *et al.* Cenozoic sea-level and cryospheric evolution from deep-sea geochemical and continental margin records. *Sci. Adv.* **6**, eaaz1346 (2020).

12. Langebroek, P. M., Paul, A. & Schulz, M. Simulating the sea level imprint on marine oxygen isotope records during the middle Miocene using an ice sheet–climate model. *Paleoceanography* **25**, (2010).

13. Gasson, E., DeConto, R. M., Pollard, D. & Levy, R. H. Dynamic Antarctic ice sheet during the early to mid-Miocene. *Proc. Natl. Acad. Sci.* **113**, 3459–3464 (2016).

14. Kominz, M. A. *et al.* Late Cretaceous to Miocene sea-level estimates from the New Jersey and Delaware coastal plain coreholes: An error analysis. *Basin Res.* **20**, 211–226 (2008).

15. Miller, K. G. *et al.* The Phanerozoic record of global sea-level change. *Science.* **310**, 1293–1298 (2005).

16. Kominz, M. A., Miller, K. G., Browning, J. V, Katz, M. E. & Mountain, G. S. Miocene relative sea level on the New Jersey shallow continental shelf and coastal plain derived from one-dimensional backstripping: A case for both eustasy and epeirogeny. *Geosphere* **12**, 1437–1456 (2016).

17. John, C. M. *et al.* Timing and magnitude of Miocene eustasy derived from the mixed siliciclastic-carbonate stratigraphic record of the northeastern Australian margin. *Earth Planet. Sci. Lett.* **304**, 455–467 (2011).

18. Pekar, S. F. & DeConto, R. M. High-resolution ice-volume estimates for the early Miocene: Evidence for a dynamic ice sheet in Antarctica. *Palaeogeogr. Palaeoclimatol. Palaeoecol.* **231**, 101–109 (2006).

19. Lear, C. H., Elderfield, H. & Wilson, P. A. Cenozoic deep-sea temperatures and global ice volumes from Mg/Ca in benthic foraminiferal calcite. *Science.* **287**, 269–272 (2000).

20. Bierman, P. R., Shakun, J. D., Corbett, L. B., Zimmerman, S. R. & Rood, D. H. A persistent and dynamic East Greenland Ice Sheet over the past 7.5 million years. *Nature* **540**, 256–260 (2016).

21. Warny, S. *et al.* Palynomorphs from a sediment core reveal a sudden remarkably warm Antarctica during the middle Miocene. *Geology* **37**, 955–958 (2009).

22. Sangiorgi, F. *et al.* Southern Ocean warming and Wilkes Land ice sheet retreat during the mid-Miocene. *Nat. Commun.* **9**, 317 (2018).

23. De Boer, B., de Wal, R. S. W., Bintanja, R., Lourens, L. J. & Tuenter, E. Cenozoic global ice-volume and temperature simulations with 1-D ice-sheet models forced by benthic $\delta^{18}O$ records. *Ann. Glaciol.* **51**, 23–33 (2010).

24. Kochhann, K. G. D., Holbourn, A., Kuhnt, W. & Xu, J. Eastern equatorial Pacific benthic foraminiferal distribution and deep water temperature changes during the early to middle Miocene. *Mar. Micropaleontol.* **133**, 28–39 (2017).

25. Shevenell, A. E., Kennett, J. P. & Lea, D. W. Middle Miocene ice sheet dynamics, deep-sea temperatures, and carbon cycling: A Southern Ocean perspective. *Geochemistry, Geophys. Geosystems* **9**, (2008).

26. Waelbroeck, C. *et al.* Sea-level and deep water temperature changes derived from benthic foraminifera isotopic records. *Quat. Sci. Rev.* **21**, 295–305 (2002).

27. Knorr, G. & Lohmann, G. Climate warming during Antarctic ice sheet expansion at the Middle Miocene transition. *Nat. Geosci.* **7**, 376 (2014).

28. Valdes, P. J. *et al.* The BRIDGE HadCM3 family of climate models: HadCM3@ Bristol v1. 0. *Geosci. Model Dev.* **10**, 3715–3743 (2017).

29. Feakins, S. J., Warny, S. & Lee, J.-E. Hydrologic cycling over Antarctica during the middle Miocene warming. *Nat. Geosci.* **5**, 557 (2012).

30. Rees-Owen, R. L. *et al.* The last forests on Antarctica: Reconstructing flora and temperature from the Neogene Sirius Group, Transantarctic Mountains. *Org. Geochem.* **118**, 4–14 (2018).

31. Passchier, S. *et al.* Early Eocene to middle Miocene cooling and aridification of East Antarctica. *Geochemistry, Geophys. Geosystems* **14**, 1399–1410 (2013).

32. Sosdian, S. M. *et al.* Constraining the evolution of Neogene ocean carbonate chemistry using the boron isotope pH proxy. *Earth Planet. Sci. Lett.* **498**, 362–376 (2018).

33. Paterson, W. S. B. *The physics of glaciers*. (Elsevier, 2016).

34. Phipps, S. J., Fogwill, C. J. & Turney, C. S. M. Impacts of marine instability across the

East Antarctic Ice Sheet on Southern Ocean dynamics. *Cryosphere* **10**, 2317–2328 (2016).

35. Rugenstein, M. *et al.* Equilibrium climate sensitivity estimated by equilibrating climate models. *Geophys. Res. Lett.* **47**, e2019GL083898 (2020).

36. Frigola, A., Prange, M. & Schulz, M. Boundary conditions for the Middle Miocene Climate Transition (MMCT v1. 0). *Geosci. Model Dev.* **11**, 1607–1626 (2018).

37. Hamon, N. *et al.* Growth of subtropical forests in Miocene Europe: The roles of carbon dioxide and Antarctic ice volume. *Geology* **40**, 567–570 (2012).

38. Levy, R. *et al.* Antarctic ice sheet sensitivity to atmospheric CO_2 variations in the early to mid-Miocene. *Proc. Natl. Acad. Sci.* **113**, 3453–3458 (2016).

39. Colleoni, F. *et al.* Spatio-temporal variability of processes across Antarctic ice-bed--ocean interfaces. *Nat. Commun.* **9**, 2289 (2018).

40. Van der Veen, C. J. Fracture mechanics approach to penetration of surface crevasses on glaciers. *Cold Reg. Sci. Technol.* **27**, 31–47 (1998).

41. DeConto, R. M. & Pollard, D. Contribution of Antarctica to past and future sea-level rise. *Nature* **531**, 591 (2016).

42. Deline, P. Change in surface debris cover on Mont Blanc massif glaciers after the 'Little Ice Age'termination. *The Holocene* **15**, 302–309 (2005).

43. Fickert, T., Friend, D., Grüninger, F., Molnia, B. & Richter, M. Did debris-covered glaciers serve as Pleistocene refugia for plants? A new hypothesis derived from observations of recent plant growth on glacier surfaces. *Arctic, Antarct. Alp. Res.* **39**, 245–

257 (2007).

44. Zale, R. *et al.* Growth of plants on the Late Weichselian ice-sheet during Greenland interstadial-1? *Quat. Sci. Rev.* **185**, 222–229 (2018).

45. Dickson, J. H. & Johnson, R. E. Mosses and the beginning of plant succession on the Walker Glacier, southeastern Alaska. *Lindbergia* **37**, 60–65 (2014).

46. Gölles, T., Bøggild, C. E. & Greve, R. Ice sheet mass loss caused by dust and black carbon accumulation. *Cryosph.* **9**, 1845–1856 (2015).

47. Williamson, C. J. *et al.* Algal photophysiology drives darkening and melt of the Greenland Ice Sheet. *Proc. Natl. Acad. Sci.* (2020).

48. De Vleeschouwer, D., Vahlenkamp, M., Crucifix, M. & Pälike, H. Alternating Southern and Northern Hemisphere climate response to astronomical forcing during the past 35 m.y. *Geology* **45**, 375–378 (2017).

49. Pekar, S. F., Christie-Blick, N., Kominz, M. A. & Miller, K. G. Calibration between eustatic estimates from backstripping and oxygen isotopic records for the Oligocene. *Geology* **30**, 903–906 (2002).

50. DeConto, R. M. & Pollard, D. Rapid Cenozoic glaciation of Antarctica induced by declining atmospheric CO_2. *Nature* **421**, 245 (2003).

Acknowledgements

C.D.B., D.J.L. were supported by NERC grant NE I006281/1. C.H.L. and S.M.S were supported by NERC grant NE/I006427/1. A.d.B. and C.D.B. gratefully acknowledge support from the

Swedish Research Council project [2016-03912]. This work was carried out using the computational facilities of the Advanced Computing Research Centre, University of Bristol - http://www.bristol.ac.uk/acrc/. We thank the reviewers for their constructive comments on our manuscript. We thank Dan Suri, Chief Operational Meteorologist, Met Office and Galia Guentchev, Senior Scientist, Met Office, Sarah Feakins and Tim Naish for feedback on earlier drafts of this manuscript. We also thank Edward Gasson for providing a plot of his ice sheet model results[13].

Author Contributions

C.D. B., C.H.L. and D.J.L. conceived the project and directed the research with the assistance of A.M.d.B. C.D.B. conducted and interpreted the modelling with the assistance of D.J.L., A.M.d.B, and P.M.L. C.D.B compiled and interpreted the proxy records with the assistance of C.H.L., A.M.dB., H.K.C. and S.M.S. C.D.B. led writing of the paper. All of the authors contributed to writing the manuscript.

Author Information

The authors declare no competing interests. Correspondence should be addressed to C.D.B.
Catherine.bradshaw@metoffice.gov.uk

Fig. 1. Mid-Miocene benthic (*Cibicidoides* spp.) oxygen isotope, deep water temperatures (DWT) and sea level changes. a $\delta^{18}O_c$ splice[48], **b** Site 1171 DWT[25], Southern Ocean (Antarctica-proximal), **c** Site 761 DWT[8], Indian Ocean (Antarctica-distal but in AABW path). Data locations shown on right of panels. DWTs are Mg/Ca reconstructions (uncertainty ±4°C; relative values are considered more robust than absolutes). Other available DWT records are too low resolution/short. Data are plotted on their respective age models (full details: Supplementary

Table S11). **d** Sea level[11,14] (Eustatic estimates[14] x1.48 c.f.[49]). Shading: Miocene Climatic Optimum (MCO, yellow), middle Miocene Climatic Transition (MMCT, blue+grey), major ice growth event (MMCT, blue). Vertical lines are indicative of the typical maximum $\delta^{18}O_c$/DWT amplitudes during the MCO (4), MMCT prior to the major ice growth event (3), MMCT major ice growth event (2) and post- MMCT (1). Since the data cover different times and resolutions, these lines are not coincident in time between panels a-c.

Fig. 2. Orography and ice sheet configurations. a Orography for the different ice volume scenarios simulated (sea level equivalent, S.L.E.). **b** Ice cover fraction for the different scenarios simulated. The latitudinal, longitudinal, topographical and DeConto and Pollard 2003[50] ice sheet extents all use the 1m S.L.E. orography from **a**. The percentage of ice cover is shown under each thumbnail. Refer also to Methods for more information.

Fig. 3. Annual mean Southern Hemisphere deep water temperatures estimates averaged between 2 and 3 km, simulated with different sized Antarctic ice sheets. a Changing ice sheet volume: ice-free (ICE_{FREE}), the 22 m sea level equivalent (S.L.E.) regional scale ice sheet configuration (ICE_{PART}22m), the 55 m S.L.E. continental ice sheet configuration (ICE_{FULL}55m), and the 90 m S.L.E. continental scale ice sheet configuration (ICE_{FULL}90m), **b** Changing ice sheet extent: different scenarios between 0% and 100% ice covered (refer to Fig. 2 for details). CO_2 is 280 ppm in all cases unless specified and a modern orbit assumed; refer to Methods for more information.

Fig. 4. Middle Miocene atmospheric CO_2 reconstructions. Data provided in Supplementary Table S5 plotted on respective age models. Shading: Miocene Climatic Optimum (MCO, yellow), middle Miocene Climatic Transition (MMCT, blue+grey), major ice growth event (MMCT, blue). Note: the Boron isotope-based CO_2 reconstructions from Sosdian et al., 2018[32] plotted are from the L02 scenario and shows two error ranges: the 66% (thicker blue lines) and 95% (thinner blue lines) confidence intervals. This dataset supercedes the data from some other publications as documented in Supplementary Table S5 (the reconstructions from the original publications are not plotted).

Fig. 5. Simulated atmospheric and oceanographic conditions with different sized Antarctic ice sheets. a, Summer (DJF) air temperature, **b**, Summer precipitation (land only shown) and sea ice fraction, **c**, Summer windspeed and prevailing directions, **d**, Annual mean Southern Hemisphere meridional mean ocean salinity, **e**, Annual mean Southern Hemisphere meridional mean ocean temperature. Scenario ICE_{FREE} has no ice sheet, ICE_{PART}22m is a regional scale 22m S.L.E. ice sheet, and ICE_{FULL}1m, ICE_{FULL}55m and ICE_{FULL}90m are 1m S.L.E., 55m and 90m S.L.E. continental size ice sheets respectively. Refer to Methods and Fig. 2 for more details of the boundary conditions used. CO_2 is 280 ppm in all cases.

Fig. 6. Annual mean Southern Hemisphere simulated with different sized Antarctic ice sheets and CO_2 concentration. Deep water temperatures are averaged between 2 and 3 km water depth. Ice sheet configurations as in Fig. 5. Refer to Methods and Fig. 2 for more details of the boundary conditions used.

Methods

The model used in these experiments is fully coupled atmosphere-ocean GCM HadCM3LB-M2.1[28] with the interactive vegetation model TRIFFID[51]. This is the low resolution ocean version of HadCM3[52] and both the atmosphere and the ocean components have a resolution of 2.5° latitude by 3.75° longitude. The model is run without the need for flux adjustments in the modern configuration by the now-standard practice of removing Iceland from the land-sea mask[53]. Eddies in the model are parameterized using a spatially constant coefficient of 1000 $m^2\ s^{-1}$ according to the Gent-Williams scheme[54]. Vertical diffusion is parameterized using the Richardson number-dependent formulation and a background diffusivity of $1\times10^{-5}\ m^2s^{-1}$ at the surface which increases linearly at a rate of $2.8\times10^{-8}\ m^2s^{-1}m^{-1}$ with depth[55]. A linear mixing profile with depth has been shown to be able to capture that vertical mixing is strongest over topography[56]. Of all the PMIP1.5 and PMIP2 models, only the HadCM3-based models, which had such a linear scheme, managed to correctly simulate the Last Glacial Maximum inverse relationship between the volume and production rate of AABW[56]. As such, we have confidence key processes determining the transfer of surface climate signals to depth are represented well in the ocean component of our model.

The background palaeogeography[57] is representative of middle Miocene conditions. Notable features as compared to modern are that the Panama Gateway and the Indonesian Seaway are open, Australia is located 4° farther south, and the Barents Sea and the Bering Strait are closed. Note that in all experiments, the Eastern Tethys Seaway is also closed. Land topography also differs from modern in that the Tibetan Plateau and the Andes are more than 2000 m lower than at present, and the Rockies Mountains are about 1000 m higher. Greenland is also more than 2000m lower than modern, and is ice free.

To investigate middle Miocene climate we used a suite of CO_2 and Antarctic ice cover sensitivity studies. Four Antarctic ice cover configurations were each simulated at 5 CO_2 concentrations: 180, 280, 400, 560 and ~850 ppm (in accordance with the uncertainty and temporal variability in CO_2 reconstructions for the middle Miocene; Fig. 4), giving a total of 20 simulations. The 4 ice sheet configurations are defined as follows. Firstly, an ice-free Antarctica using an Antarctic bedrock configuration appropriate for the Late Oligocene[57], referred to as "ICE_{FREE}". Ice free Antarctica is initialised in the TRIFFID model as covered in in the plant functional type 'shrubs'. Although unrealistic for the mid Miocene, as the extreme end member scenario, this scenario helps to place our findings into context. Secondly, a skin-thickness ice-covered Antarctica (< 1m sea level equivalent) where the topography is kept the same as in the ice-free case in 1, referred to as "ICE_{FULL}1m". Thirdly, a modern-like ice-covered Antarctica (~55 m sea level equivalent) using the palaeogeographic configuration for the middle Miocene[57], referred to as "ICE_{FULL}55m". Finally, a larger-than-modern ice-covered Antarctica (~90 m sea level equivalent), referred to as "ICE_{FULL}90m".

Configurations 2-4 have the same areal extent and differ in ice sheet height only. In accordance with the proposed 90m drop in sea level over the MMCT[9], boundary conditions for an ice sheet of this proportion were developed by assuming one-third of the ice is associated with isostatic depression and then applying a uniform increase in elevation across the continent to obtain a 90 m sea level equivalent. Additionally simulated at 280 ppm (using the topography of the ICE_{FULL}55m scenario) is the spatial extent of the regional scale ice sheet simulated by a model that includes ice-shelf hydrofracture and ice cliff collapse of 22 m S.L.E., [13], referred to as "ICE_{PART}22m". See Fig. 2 for more details of the Antarctic boundary conditions. Outside of Antarctica, the paleogeography remains constant at the middle Miocene reconstruction. Apart from the prescribed CO_2 changes, all other greenhouse gases, solar and orbital parameters remain at modern settings.

To investigate the sensitivity of the hydrological cycle to the extent of Antarctic ice-free area, an additional series of simulations were carried out with a gradually increasing Antarctic ice sheet area, from no ice to the maximum ice sheet extent for scenario 2 above. These intermediate area ice sheets expand latitudinally, longitudinally or topographically as demonstrated in Fig. 2. No change was made to the elevation from the ice-free condition and therefore all of these simulations represent a skin-thickness of ice cover. Two sets of scenarios were run for each of the longitudinal ice growth boundary conditions: Firstly, beginning from an ice-free initial condition (as described above) and secondly, beginning from a 100% ice-covered initial condition and decreasing towards zero. The rest of the scenarios were initiated from the 100% ice-covered state and therefore lose ice only. The longitudinal ice growth scenario also included 4 configurations simulated at ~850 ppm CO_2 (20%, 40%, 60% and 80% ice-covered, refer to Fig. 2).

All simulations assume a modern orbit except for 4 sensitivity test cases. A cold orbital configuration favorable for Antarctic glaciation (low obliquity (22.1°), high eccentricity (0.054), perihelion during boreal summer, 374 W/m^2 summer insolation at 70°S) and a warm orbital configuration favourable for Antarctic deglaciation (high obliquity (24.5°), high eccentricity (0.054), perihelion during austral summer, 483 W/m^2 summer insolation at 70°S) were identified. Cold and warm orbit sensitivity tests were carried out for the "ICE_{FREE}" and the "ICE_{FULL}55m" configurations.

All of the middle Miocene simulations continue from a 2100 year integration under late Miocene boundary conditions[58] and have been run for a further 2000 years. Supplementary Figures S65-

S68 show the evolution of deep water temperatures throughout the simulations and give us confidence that they have stabilised sufficiently for us to draw conclusions.

References

51. Cox, P. M. Description on the TRIFFID Dynamic Global Vegetation Model. *Technical Report 24* (Hadley Centre, Met Office, 2001).

52. Gordon, C. *et al.* The simulation of SST, sea ice extents and ocean heat transports in a version of the Hadley Centre coupled model without flux adjustments. *Clim. Dyn.* **16**, 147–168 (2000).

53. Jones, C. A fast ocean GCM without flux adjustments. *J. Atmos. Ocean. Technol.* **20**, 1857–1868 (2003).

54. Gent, P. R. & McWilliams, J. C. Isopyncnal mixing in ocean circulation models. *J. Phys. Oceanogr.* **20**, 150–155 (1990).

55. Pacanowski, R. & Philander, S. Parameterization of vertical mixing in numerical models of tropical oceans. *J. Phys. Oceanogr.* **11**, 1443–1451 (1981).

56. De Boer, A. M. & Hogg, A. M. Control of the glacial carbon budget by topographically induced mixing. *Geophys. Res. Lett.* **41**, 4277–4284 (2014).

57. Markwick, P. J. The palaeogeographic and palaeoclimatic significance of climate proxies for data-model comparisons. in *Deep-Time Perspectives on Climate Change: Marrying the Signal from Computer Models and Biological Proxies* 251–312 (The Geological Society, 2007).

58. Bradshaw, C. D. *et al.* The relative roles of CO_2 and palaeogeography in determining late Miocene climate: results from a terrestrial model-data comparison. *Clim. Past* **8**, 715–786 (2012).

Code Availability

The UK Met Office made available the source code of HadCM3 via the Ported Unified Model release (http://www.metoffice.gov.uk/research/collaboration/um-partnership). Enquiries regarding the use of HadCM3 should be directed in the first instance to the UM Partnership team, who can be contacted at um_collaboration@metoffice.gov.uk. The main repository for the Met Office Unified Model (UM) version corresponding to the model presented here can be viewed at http://cms.ncas.ac.uk/code_browsers/UM4.5/UMbrowser/index.html. The code detailing the changes required to update HadCM3 to HadCM3LB-M2.1 are available as a Supplement to Valdes et al. (2017)[28].

Data Availability

The climate model output data is available for analysis and download at https://www.paleo.bristol.ac.uk/ummodel/scripts/papers/Bradshaw_et_al_2021.html. It is possible to reproduce the information in Fig. 2, Fig. 3, Fig. 5 and Fig. 6 via this interface as well as download the data itself and the ancillary information (paleogeography and ice sheet configuration).

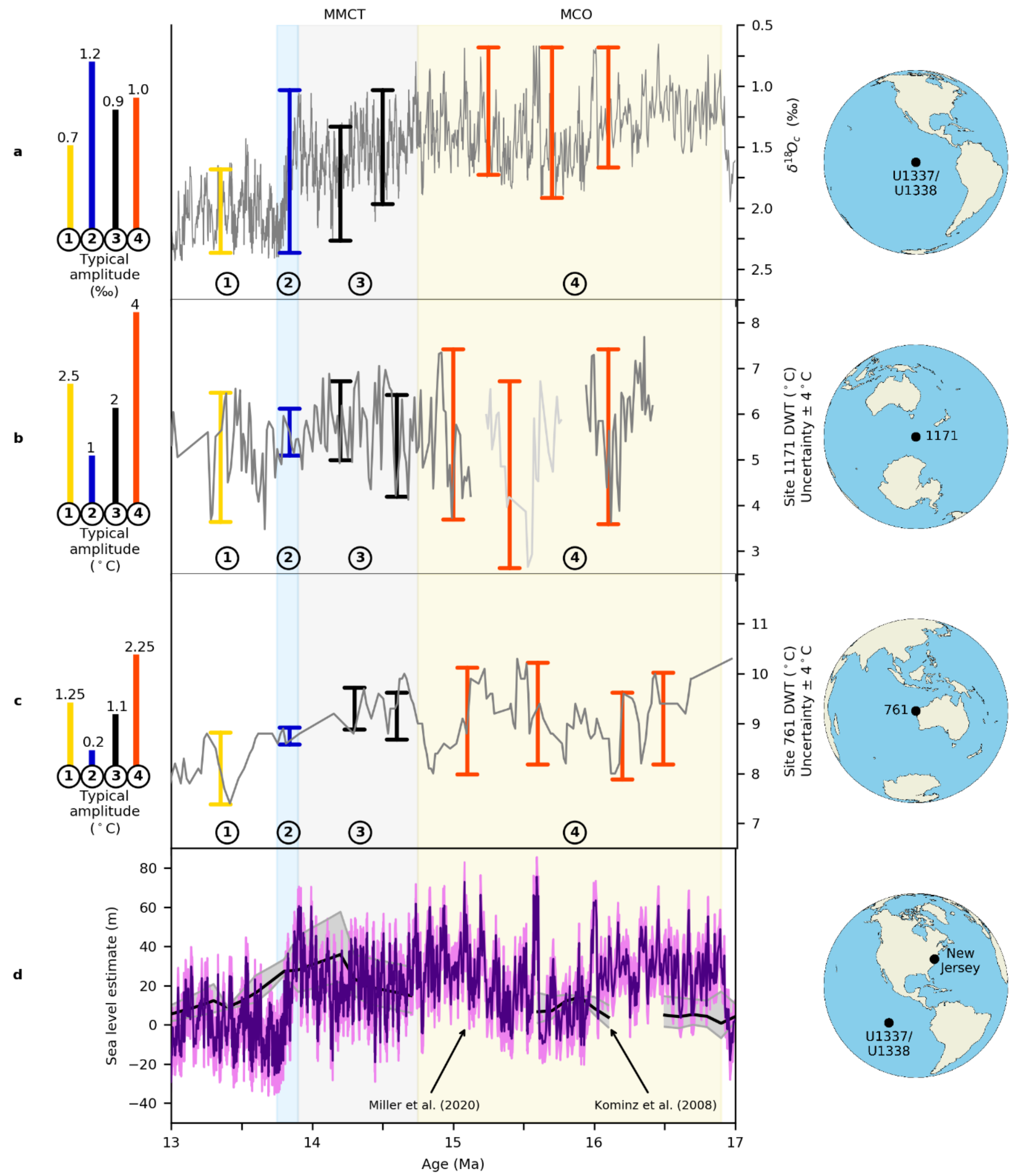

Fig. 1. Mid-Miocene benthic (*Cibicidoides* spp.) oxygen isotope, deep water temperatures (DWT) and sea level changes. a $\delta^{18}O_c$ splice[48], **b** Site 1171 DWT[25], Southern Ocean (Antarctica-proximal), **c** Site 761 DWT[8], Indian Ocean (Antarctica-distal but in AABW path). Data locations shown on right of panels. DWTs are Mg/Ca reconstructions (uncertainty ±4°C; relative values are considered more robust than absolutes). Other available DWT records are too low resolution/short. Data are plotted on their respective age models (full

details: Supplementary Table S11). **d** Sea level[11,14] (Eustatic estimates[14] x1.48 c.f.[49]). Shading: Miocene Climatic Optimum (MCO, yellow), middle Miocene Climatic Transition (MMCT, blue+grey), major ice growth event (MMCT, blue). Vertical lines are indicative of the typical maximum $\delta^{18}O_c$/DWT amplitudes during the MCO (4), MMCT prior to the major ice growth event (3), MMCT major ice growth event (2) and post- MMCT (1). Since the data cover different times and resolutions, these lines are not coincident in time between panels a-c.

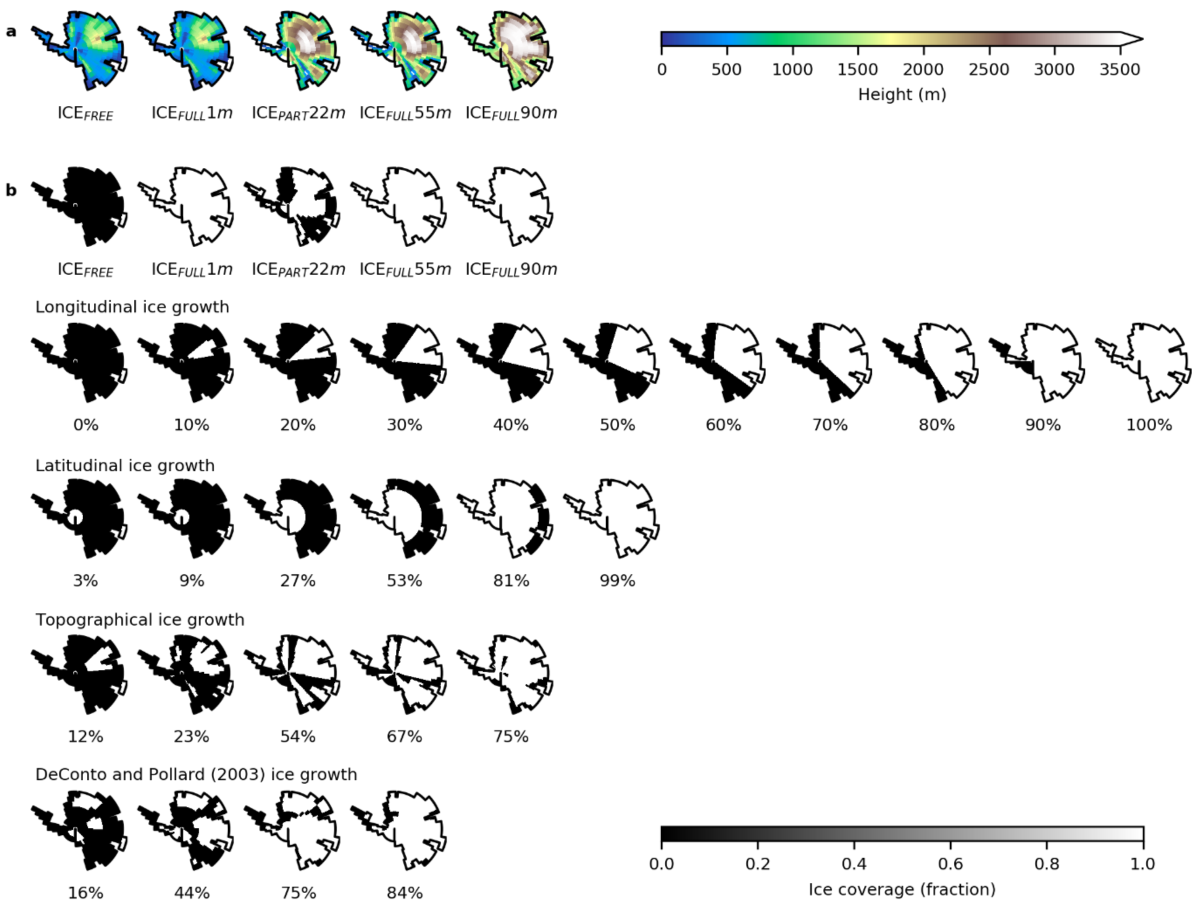

Fig. 2. Orography and ice sheet configurations. a Orography for the different ice volume scenarios simulated (sea level equivalent, S.L.E.). **b** Ice cover fraction for the different scenarios simulated. The latitudinal, longitudinal, topographical and DeConto and Pollard 2003[50] ice sheet extents all use the 1m S.L.E. orography from **a**. The percentage of ice cover is shown under each thumbnail. Refer also to Methods for more information.

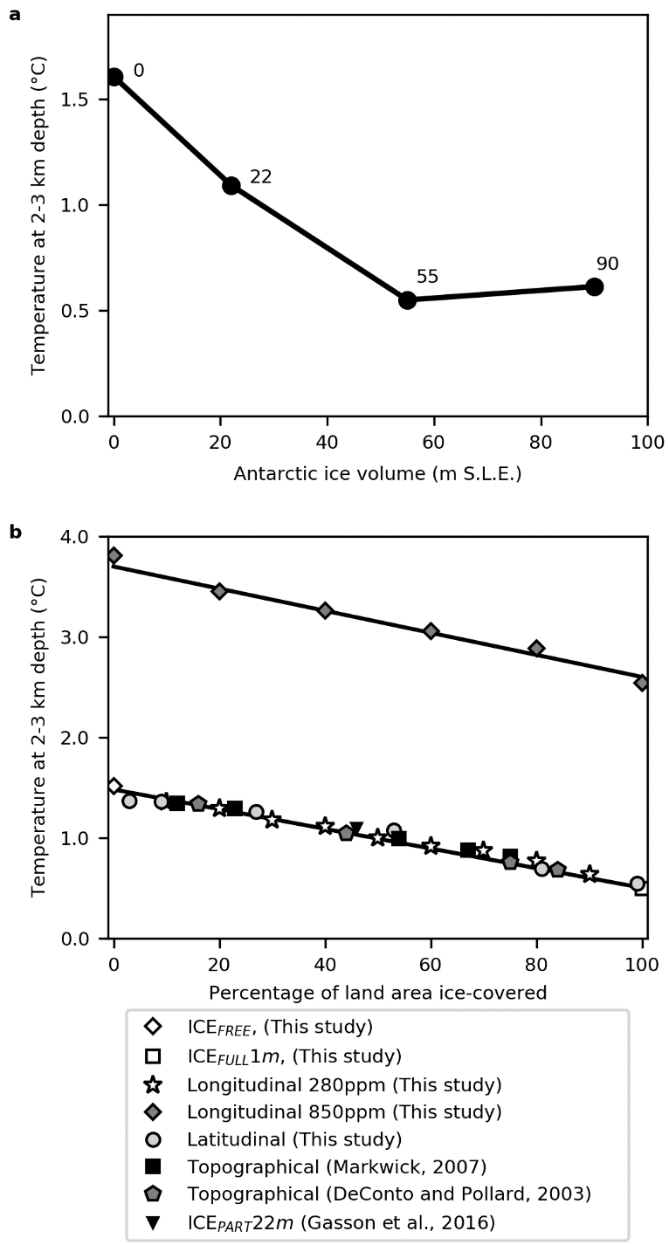

Fig. 3. Annual mean Southern Hemisphere deep water temperatures estimates averaged between 2 and 3 km, simulated with different sized Antarctic ice sheets. a Changing ice sheet volume: ice-free (ICE_{FREE}), the 22 m sea level equivalent (S.L.E.) regional scale ice sheet configuration (ICE_{PART}22m), the 55 m S.L.E. continental ice sheet configuration (ICE_{FULL}55m), and the 90 m S.L.E. continental scale ice sheet configuration (ICE_{FULL}90m), **b** Changing ice sheet extent: different scenarios between 0% and 100% ice covered (refer to Fig. 2 for details). CO_2 is 280 ppm in all cases unless specified and a modern orbit assumed; refer to Methods for more information.

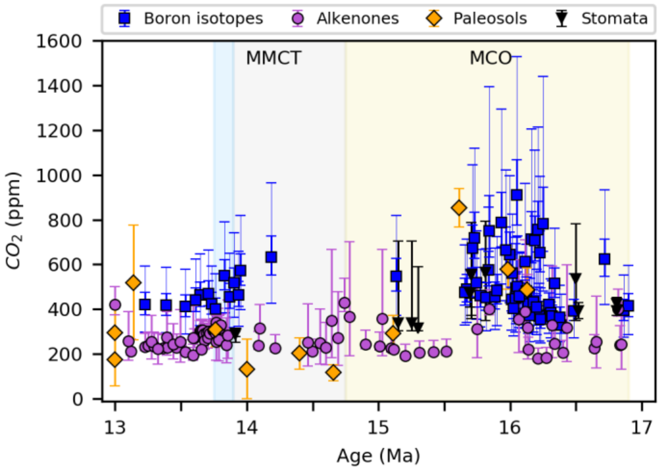

Fig. 4. Middle Miocene atmospheric CO_2 reconstructions. Data provided in Supplementary Table S5 plotted on respective age models. Shading: Miocene Climatic Optimum (MCO, yellow), middle Miocene Climatic Transition (MMCT, blue+grey), major ice growth event (MMCT, blue). Note: the Boron isotope-based CO_2 reconstructions from Sosdian et al., 2018[32] plotted are from the L02 scenario and shows two error ranges: the 66% (thicker blue lines) and 95% (thinner blue lines) confidence intervals. This dataset supercedes the data from some other publications as documented in Supplementary Table S5 (the reconstructions from the original publications are not plotted).

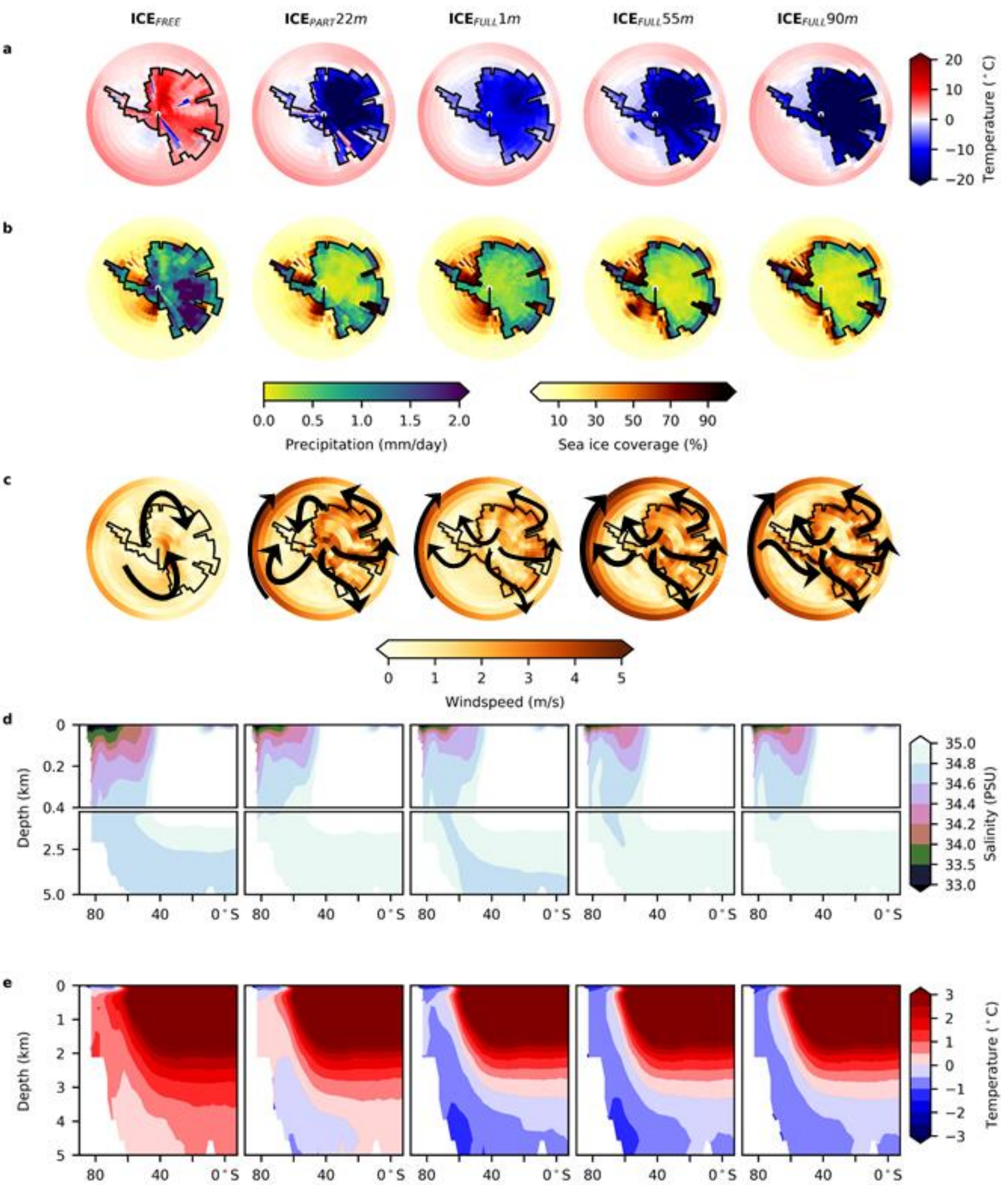

Fig. 5. Simulated atmospheric and oceanographic conditions with different sized Antarctic ice sheets. a, Summer (DJF) air temperature, **b**, Summer precipitation (land only shown) and sea ice fraction, **c**, Summer windspeed and prevailing directions, **d**, Annual mean Southern Hemisphere meridional mean ocean salinity, **e**, Annual mean Southern Hemisphere meridional mean ocean temperature. Scenario ICE_{FREE} has no ice sheet, ICE_{PART}22m is a regional scale 22m S.L.E. ice sheet, and ICE_{FULL}1m, ICE_{FULL}55m and ICE_{FULL}90m are 1m

S.L.E., 55m and 90m S.L.E. continental size ice sheets respectively. Refer to Methods and Fig. 2 for more details of the boundary conditions used. CO_2 is 280 ppm in all cases.

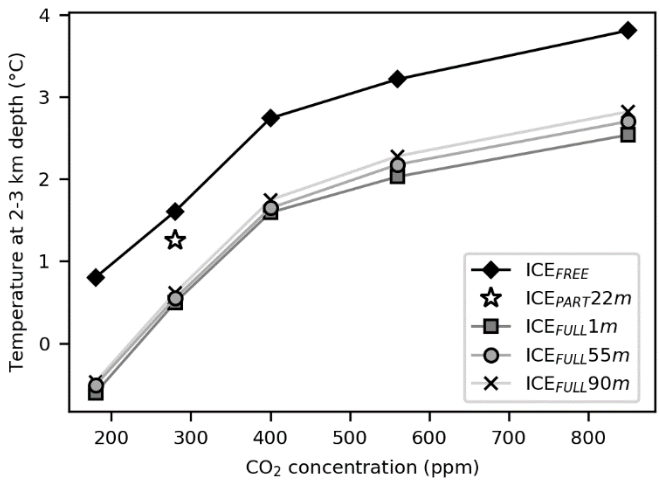

Fig. 6. Annual mean Southern Hemisphere simulated with different sized Antarctic ice sheets and CO_2 concentration. Deep water temperatures are averaged between 2 and 3 km water depth. Ice sheet configurations as in Fig. 5. Refer to Methods and Fig. 2 for more details of the boundary conditions used.

Hydrological impact of Middle Miocene Antarctic ice-free areas coupled to deep ocean temperatures: Supplementary Information

Catherine D. Bradshaw, Petra M. Langebroek, Caroline H. Lear, Daniel J. Lunt, Helen K. Coxall, Sindia M. Sosdian, Agatha M. de Boer.

Contents:

S1. Supplementary Note

Model-Data Comparison

Methodology

There are many difficulties associated with developing a model-data comparison methodology, and in the interpretation of results. The model-data comparison methodology adopted follows previous work for the late Miocene[1,2]. Terrestrial data reconstructions are given in Supplementary Tables S6-9, sea surface temperature (SST) estimates are given in Supplementary Table S10 and deep water temperature (DWT) estimates are given in Supplementary Table S11. Due to the higher temporal resolution of the marine data as compared to the terrestrial data, two slightly different approaches are used. Core-based terrestrial data, being of higher resolution and better age constaint, are additionally treated the same as SST data.

For the terrestrial data:

- Mean annual temperature and precipitation reconstructions are split into two timeslices of 13-14.5 Ma (icehouse) and 14.5 -16.75 Ma (greenhouse) in order to attempt to identify any differences between the MMCT and the MCO. Where age uncertainty is large data will appear in both timeslices and these data are treated separately.
- Within each timeslice, the minimum and maximum temperature and precipitation estimates for each site are retained, and the calibration uncertainty added (where the calibration uncertainty has not been stated by the original author, an uncertainty of 1°C has been assumed).
- Each individual proxy location has been translated back to an estimated paleolocation as dictated by the age control. With the exception of the data taken from Goldner et al., 2014[3] (which is used as is because the original latitude and longitude values were not provided), the same paleorotation has been used as the construction of the Middle Miocene paleogeography[4] to ensure consistency with the model results. Given the uncertainties in the dating of most terrestrial data, the middle of the age ranges has been used.

- All grid cells adjacent to the grid cell containing the paleodata are used to derive the model values. Taking this approach allows for data location uncertainties such as transportation and paleorotation, and allows for model uncertainties in the placement of largescale climate features (it is unreasonable to expect a GCM to reconstruct the exact climate at a single grid cell; greater reliance should be placed on broad-scale patterns).
- Where terrestrial reconstructions have been derived from marine core data, the datapoint location has been manually moved to the nearest land grid cell.
- We remove one of the data from the Goldner et al., 2014[3] synthesis for the Falkland Islands since this is not resolved as land in our model.

For the marine data:

- Uncertainty estimates are added to the seawater temperature estimate at each datapoint at each site. Although there are many different calibration equations, assumptions about the past seawater conditions and dissolution depth-corrections, we have used the temperature estimates from the original sources. An element of the remaining inconsistencies between the model output and the data could therefore be related to these uncertainties unaccounted for here. For example, the uncertainty in DWT in the Mg/Ca proxy reconstructions at Site 1171 arising just from using a different calibration equation are of the order ~2°C[5].
- Typically, calibration uncertainties derived from modern Mg/Ca-temperature calibrations are on the order of ±1˚C. However, there are other controls on foraminiferal Mg/Ca that have been dealt with in different ways in the literature. For example, variations in seawater Mg/Ca will impact both benthic and planktonic foraminiferal Mg/Ca. Epifaunal species of benthic foraminifera may be sensitive to changes in bottom water carbonate saturation state[6]. Planktonic foraminiferal Mg/Ca may be sensitive to change in sea surface pH and salinity[7]. It is impossible to correct all previously published records for such effects, as they have not been published with the required additional data (e.g., benthic foraminiferal B/Ca, planktonic foraminiferal $\delta^{11}B$). Instead, we therefore increase the uncertainty on absolute temperature estimates from ±1˚C to ±4˚C to include any potential bias from these sources. This large uncertainty window applies to absolute

temperatures – reconstructed relative changes in downcore temperatures such as those shown in Fig. 1 have smaller uncertainties.

- Each individual proxy location has been translated back to an estimated paleolocation as dictated by the age control.
- All grid cells adjacent to the grid cell containing the paleodata are used to derive the model values (horizontally and vertically).
- The SST reconstructions are compared to the simulated mean annual temperatures of the surface ocean. In addition, to allow for any seasonal bias in production, the high latitude sites are also compared to the simulated maximum temperatures of the surface ocean.
- The DWT reconstructions are compared to the simulated mean annual temperature at the estimated paleodepths of the core sites.
- As the authors do not specify which of the reconstructed DWT relationships to use, both reconstructions suggested by Lear et al., 2010[8] (adjusted and unadjusted for assumed changes in saturation state) and both reconstructions suggested by Lear et al., 2015[9] (linear-fitted and exponential-fitted curves) have been plotted.

To reflect the uncertainties in the data reconstructions and the model results, both are treated as a range of possible values and the term overlap is defined as consistency between model and data if their uncertainty ranges overlap (Supplementary Figure S1a). Where the data and model overlap, it is not possible to determine that they are different; it does not necessarily follow that the data and the model are in agreement if the uncertainty ranges are large (Supplementary Figure S1b). Reference made to any differences between the data reconstructions and the model output in this study therefore refer to the minimum possible difference only. No attempt has been made to try to correct for any GCM bias with respect to modern observations. Such a correction is very difficult because of the large gap in age, it is not considered robust to assume that biases in the model for present day conditions would be the same as any biases in the model for conditions ~15 million years ago because of differences in the land-sea mask affecting ocean circulation, and the removal of continental ice from both Greenland and Antarctica in this study.

Results

Mean annual air temperature

The model-data comparisons show that the 853ppm CO_2 concentration simulations all overlap with the icehouse subset data reconstructions (Supplementary Figure S2). There is more data available in the terrestrial greenhouse subset and the subset of data with poor age control, and both of these show the closest overall match to the data occurs with the 560 ppm CO_2 concentration scenario with no Antarctic ice sheet (Supplementary Figures S3 and S4). For the individual sites, the higher CO_2 concentrations scenarios also show the best model-data fit (Supplementary Figures S5 to S7). Notwithstanding the sparse closely-clustered terrestrial data available for the icehouse period, there is, therefore, no evidence from the terrestrial model-data comparison to support a lowering of CO_2 for the MMCT as compared to the MCO. The data reconstructions are mixed though, between being warmer than the model simulations in the high latitudes and colder than the model simulations in the mid-latitudes of Asia, and it is therefore unlikely that there would be a single CO_2 concentration that could improve the terrestrial model-data comparison.

Mean annual precipitation

The limited mean annual precipitation data suggests that all CO_2/ice sheet scenarios overlap with the data reconstructions from the icehouse subset (Supplementary Figure S8) and the subset with poor age control (Supplementary Figure S10). The same is true for the Antarctic data precipitation data reconstructions in the greenhouse subset, but data reconstructions from the New Zealand locations in that timeslice are wetter than the models can reproduce (Supplementary Figure S9).

Summer mean air temperature

All of the CO_2/ice sheet configuration scenarios overlap with the summer mean temperature data reconstructions on Antarctica when the data is considered as a timeslice mean (Supplementary Figures S11). The warmest of the individual datapoints, however, only overlap with the ICE_{FREE} scenario for the 400, 560 and 853 ppm CO_2 concentrations (Supplementary Figure S12).

Summer total precipitation

None of the CO_2/ice sheet configuration scenarios overlap with the summer precipitation data reconstructions on Antarctica when the data is considered as a timeslice mean (Supplementary Figures S13) but the highest CO_2 concentration scenario shows the closest fit (Supplementary Figure S14).

Mean annual sea surface temperature

The marine SST model-data comparison shows that the warmest data reconstructions are typically warmer than the model simulations at high latitudes even at the highest CO_2 concentrations tested, but the data reconstructions typically overlap with the model simulations at the lower latitudes, athough here it is often restricted to the lower CO_2 concentrations (Supplementary Figures S15 to S29). The model simulations therefore show the same difficulties in reproducing the equator-to-pole temperature gradients reconstructed by the data as other models[3,10,11].

Maximum monthly sea surface temperature

If the high latitude data are assumed to contain a warm-season bias, the cooler icehouse records typically overlap with the model simulations at 280 ppm CO_2 or higher, but the warmer greenhouse records still prove difficult to simulate (Supplementary Figures S30 to S38).

Annual mean deep water temperatures

The model simulated deep water temperatures typically overlap with the data reconstructions for all but the warmest of temperatures for the higher CO_2 concentration assumptions (Supplementary Figures S39 to S46).

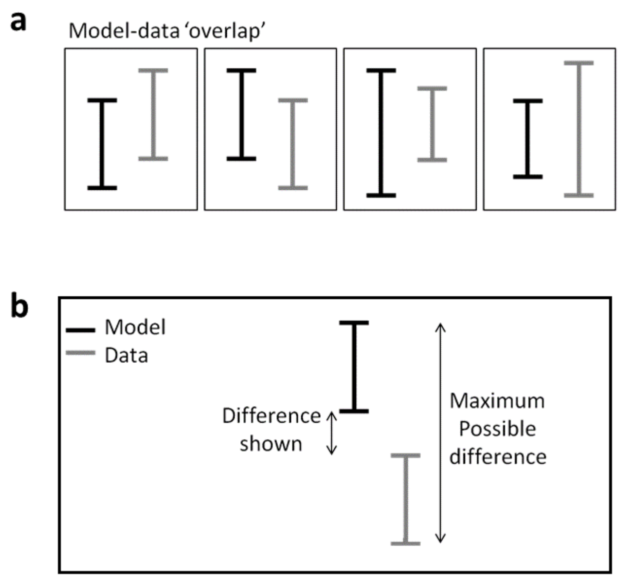

Supplementary Figure S1. Model-data comparison definitions. **(a)** The definition for "overlap" used in the comparison (all four instances shown are considered as an overlap), **(b)**: Although data-model mismatch is defined as the minimum possible distance to overlap, the maximum possible differences could be much greater if the true values for both the model and the data were to lie at the extremes of the uncertainty ranges.

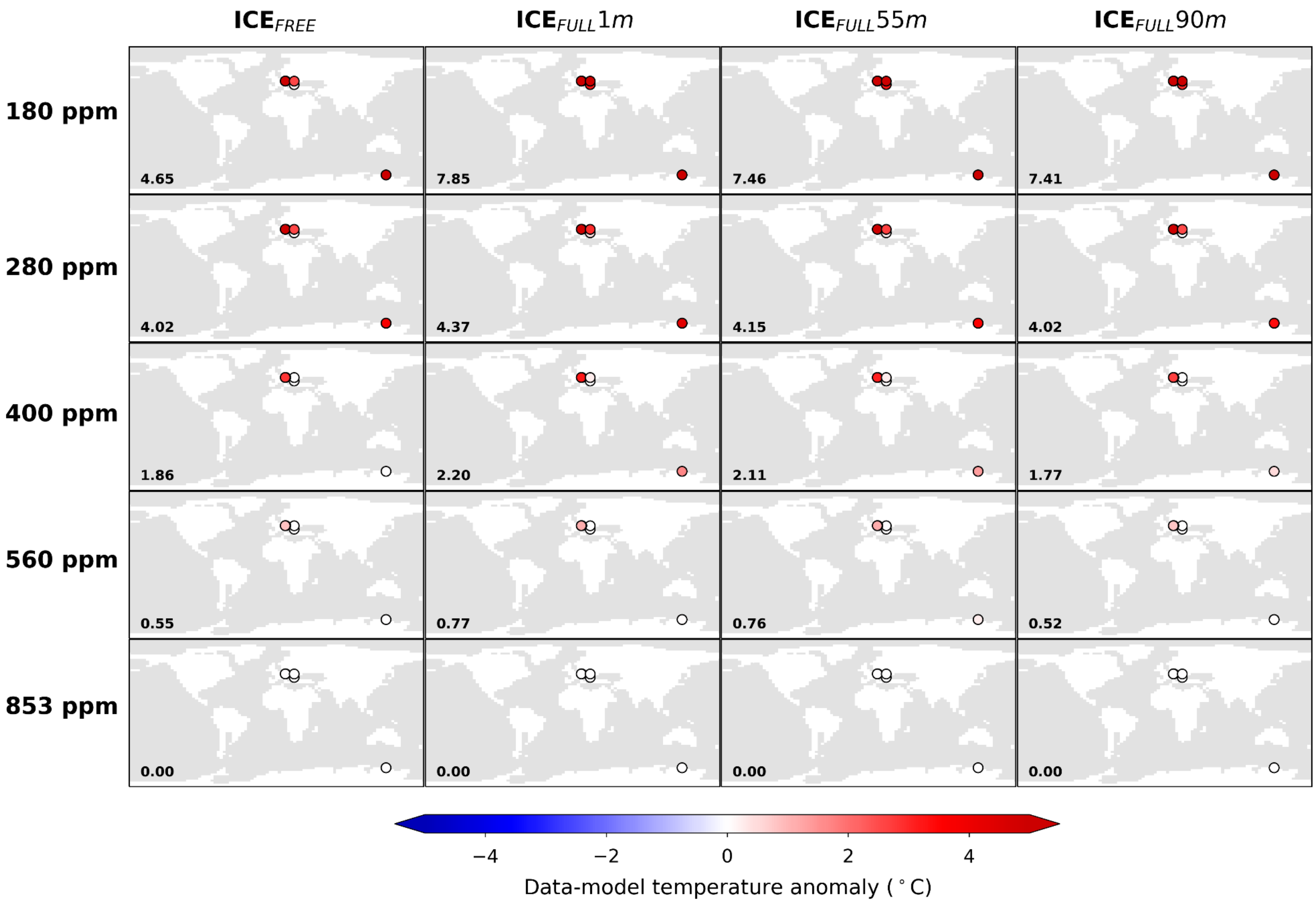

Supplementary Figure S2. Annual mean air temperature model-data comparison for icehouse (13-14.5 Ma) data reconstructions given in Supplementary Table S6. The columns show results for an ice-free Antarctica, a 1m, a 55m and a 90m sea level equivalent Antarctic ice sheet from left to right respectively. The rows show results for atmospheric CO_2 set to 180ppm, 280ppm, 400ppm, 560ppm and 853ppm from top to bottom respectively. The markers are positioned at the mean data reconstruction ages and coloured according to the data-model anomaly (red indicates the data reconstruction is warmer than the model simulates, blue indicates it is cooler and white indicates overlap between the data reconstruction and the model simulation). The RMSE value for the whole synthesis is in the bottom left-hand corner for each scenario.

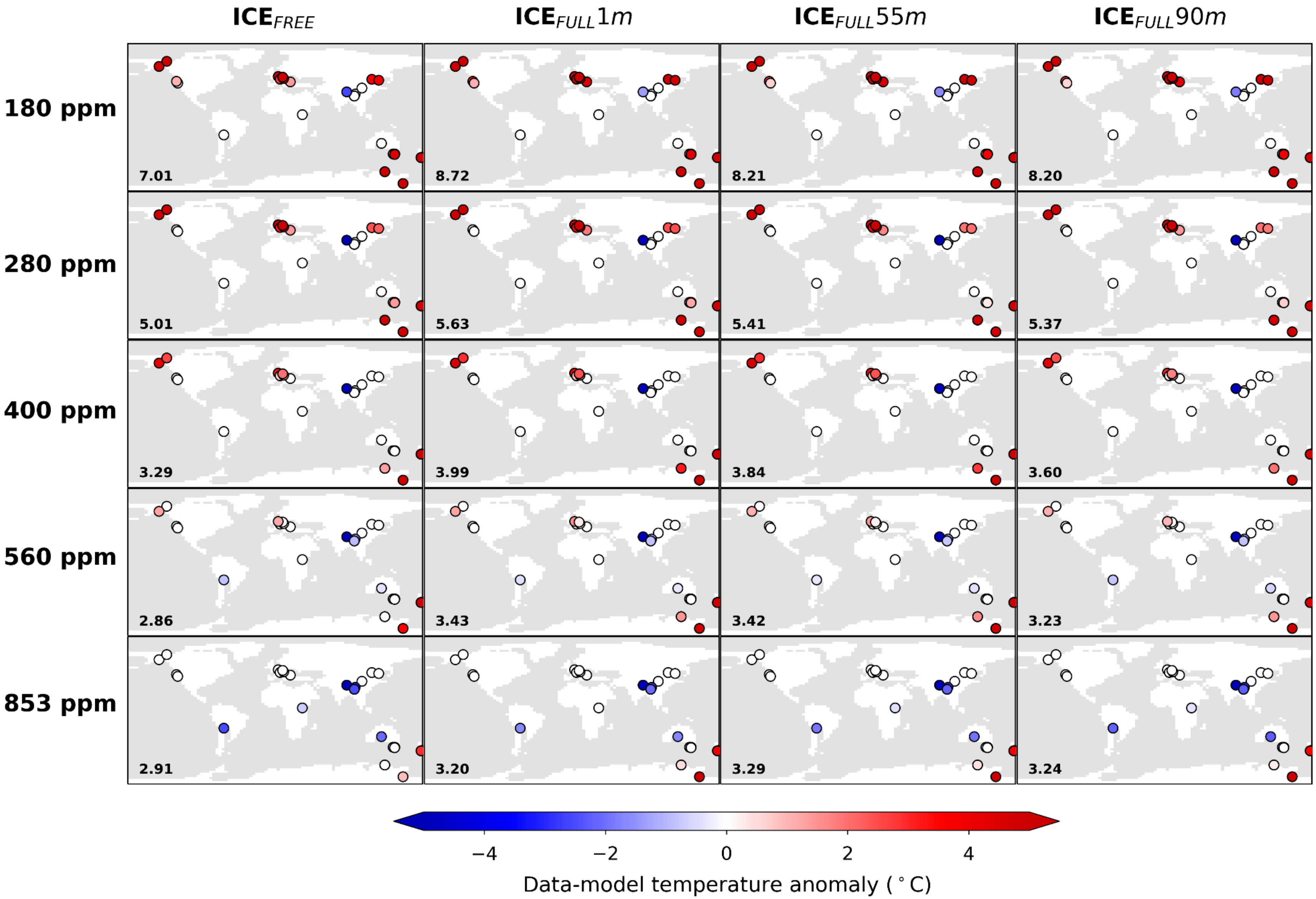

Supplementary Figure S3. Annual mean air temperature model-data comparison for greenhouse (14.5-16.75 Ma) data reconstructions given in Supplementary Table S6. Legend information as in Supplementary Figure S2.

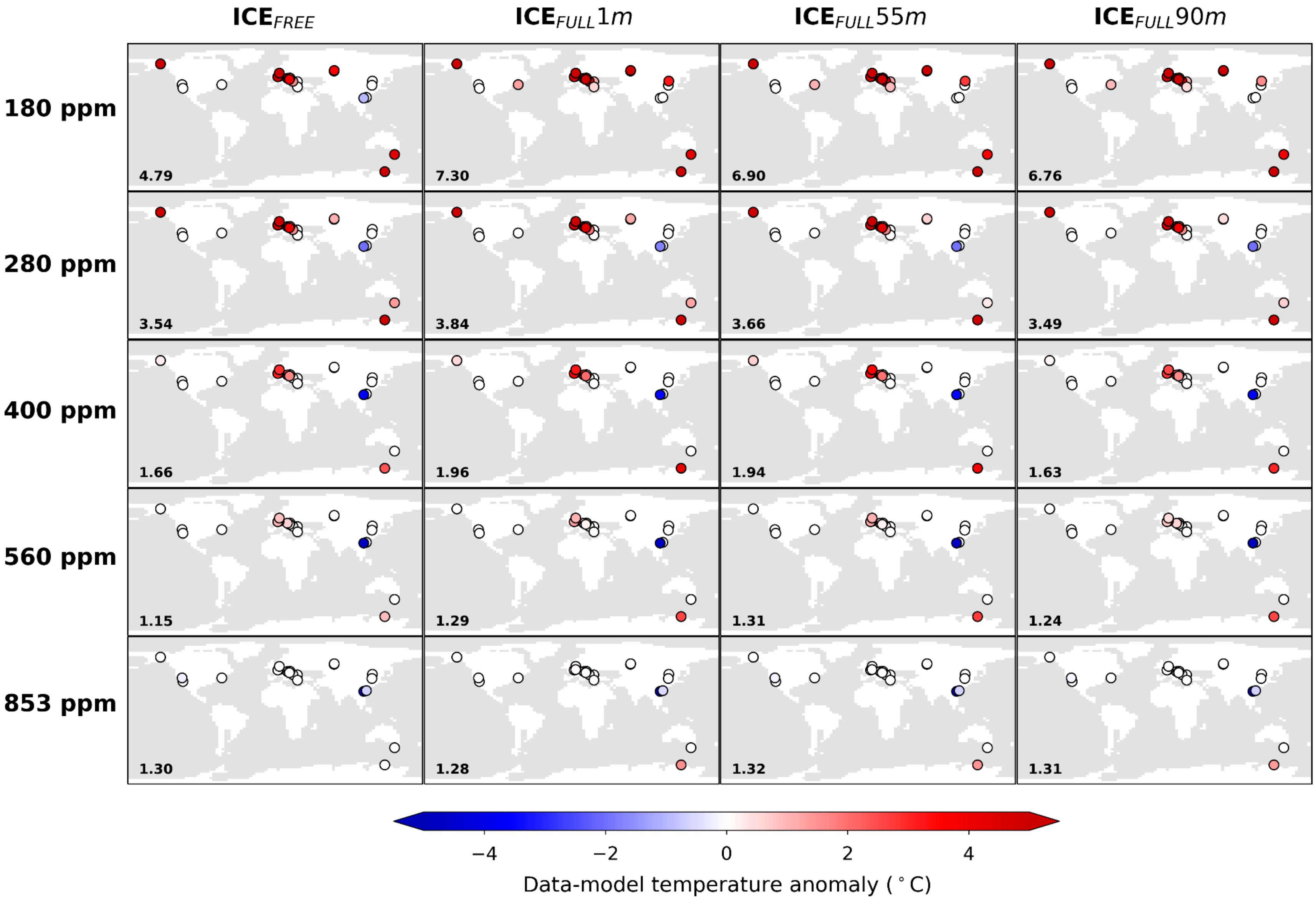

Supplementary Figure S4. Annual mean air temperature model-data comparison for middle Miocene data reconstructions given in Supplementary Table S6 with poor age control. Legend information as in Supplementary Figure S2.

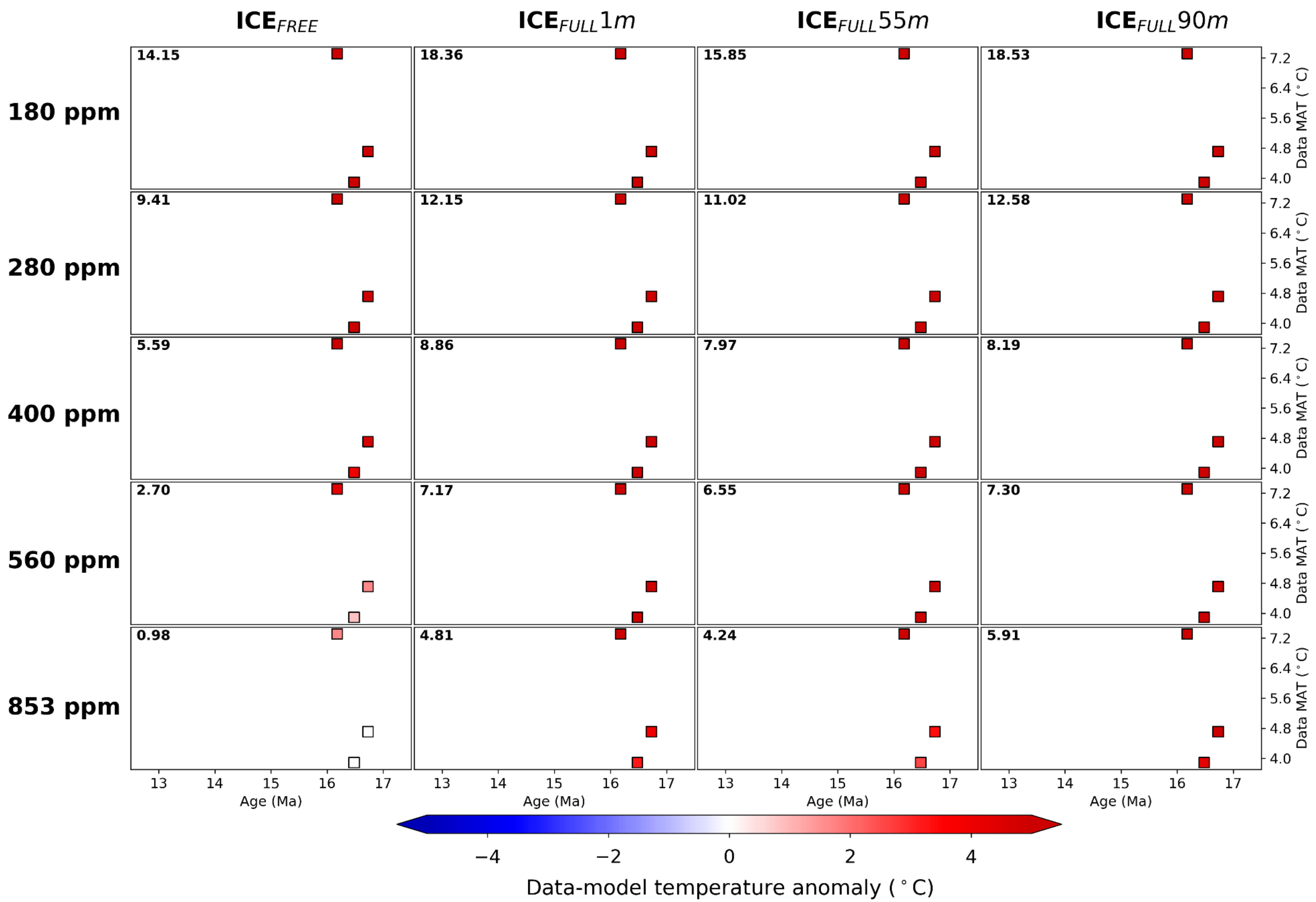

Supplementary Figure S5. Annual mean air temperature model-data comparison for middle Miocene data reconstructions for Site CRP-1 in the Ross Sea. Data from Paschier et al., 2013[12] as given in Supplementary Table S6. Legend information as in Supplementary Figure S2.

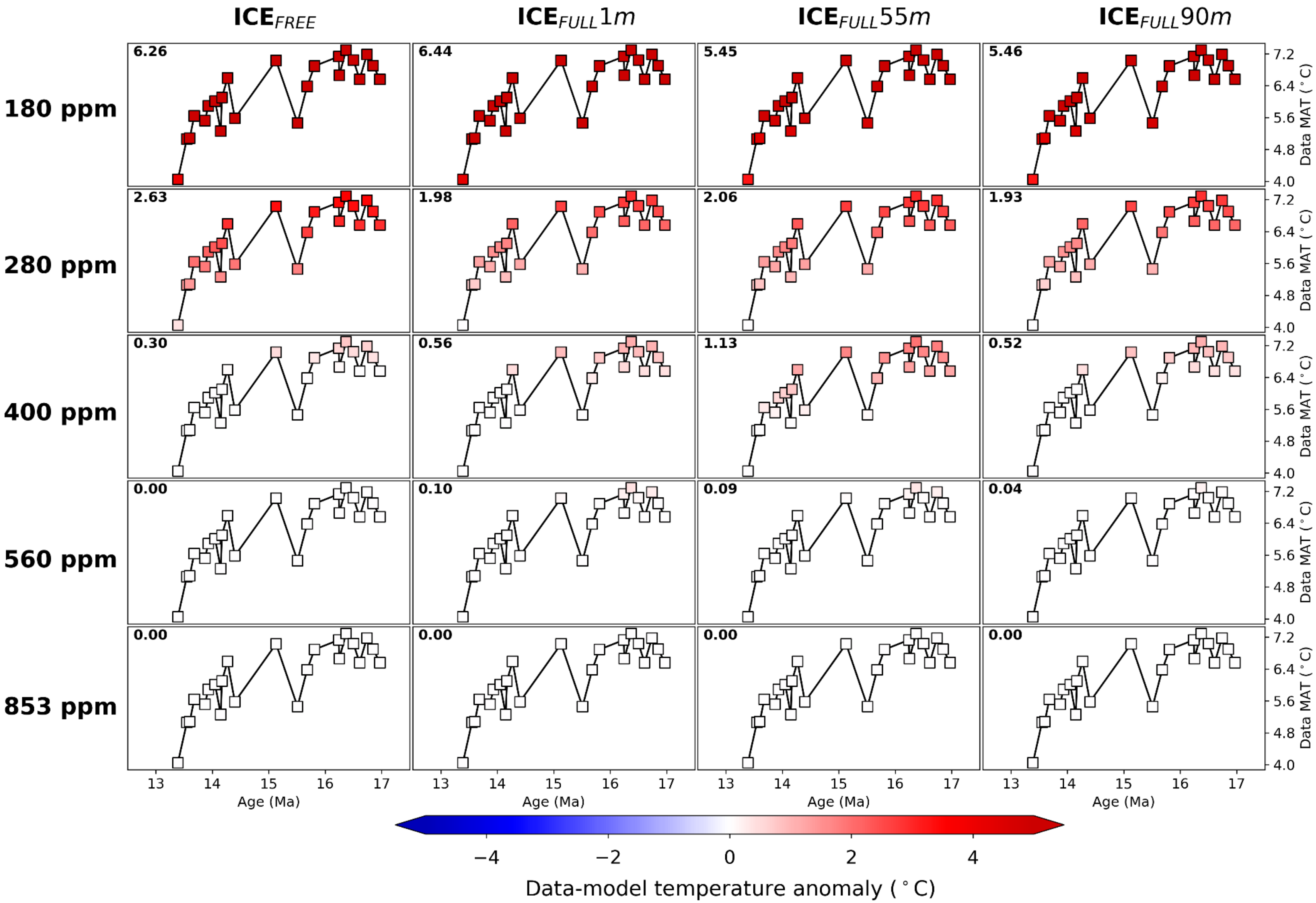

Supplementary Figure S6. Annual mean air temperature model-data comparison for middle Miocene data reconstructions for Site U1356A in the Wilkes Land Continental Margin. Data from Paschier et al., 2013[12] as given in Supplementary Table S6. Legend information as in Supplementary Figure S2.

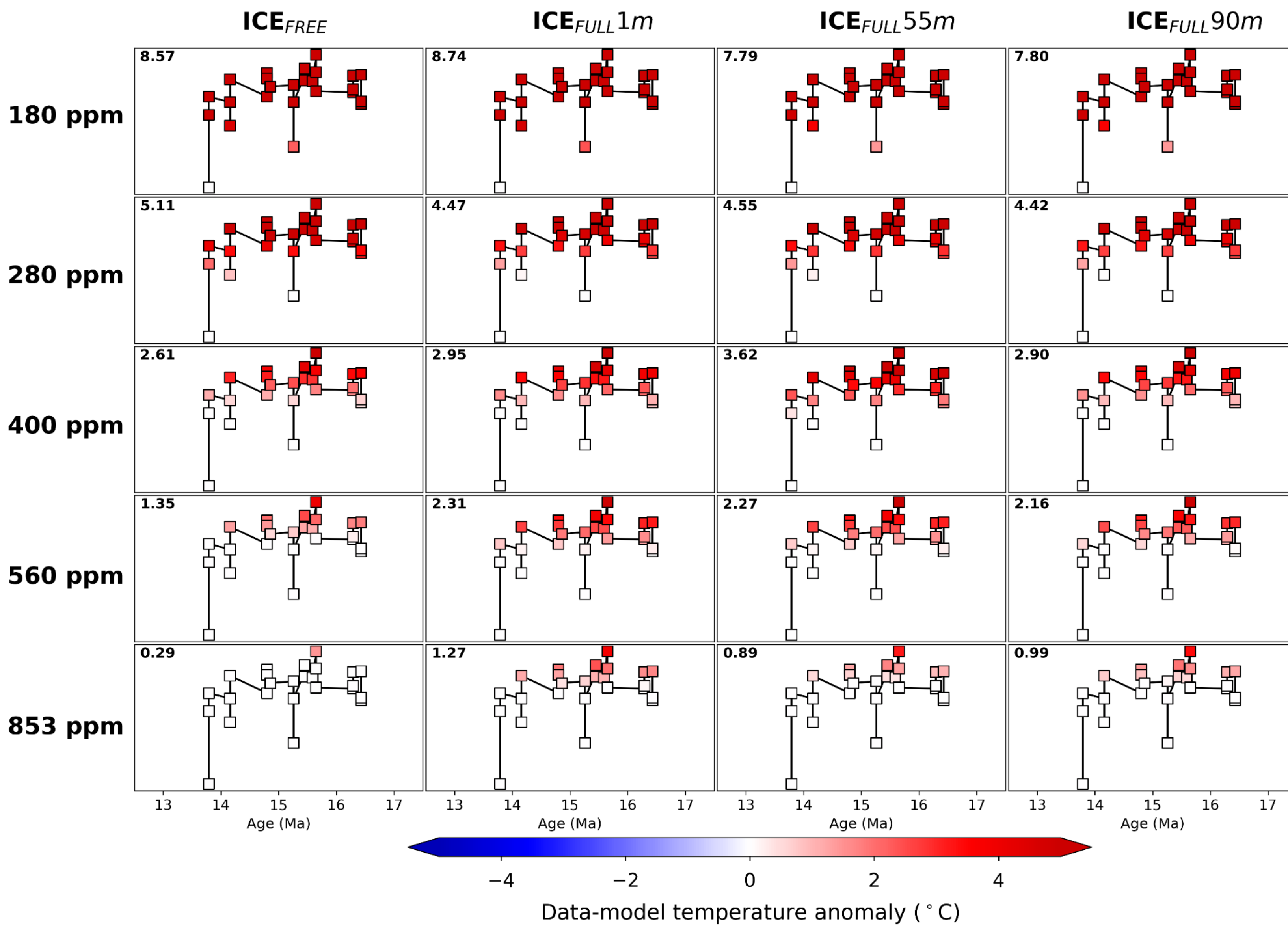

Supplementary Figure S7. Annual mean air temperature model-data comparison for middle Miocene data reconstructions for Site U1356 in the Wilkes Land Continental Margin. Data from Sangiorgi et al., 2018[13] as given in Supplementary Table S6. Legend information as in Supplementary Figure S2.

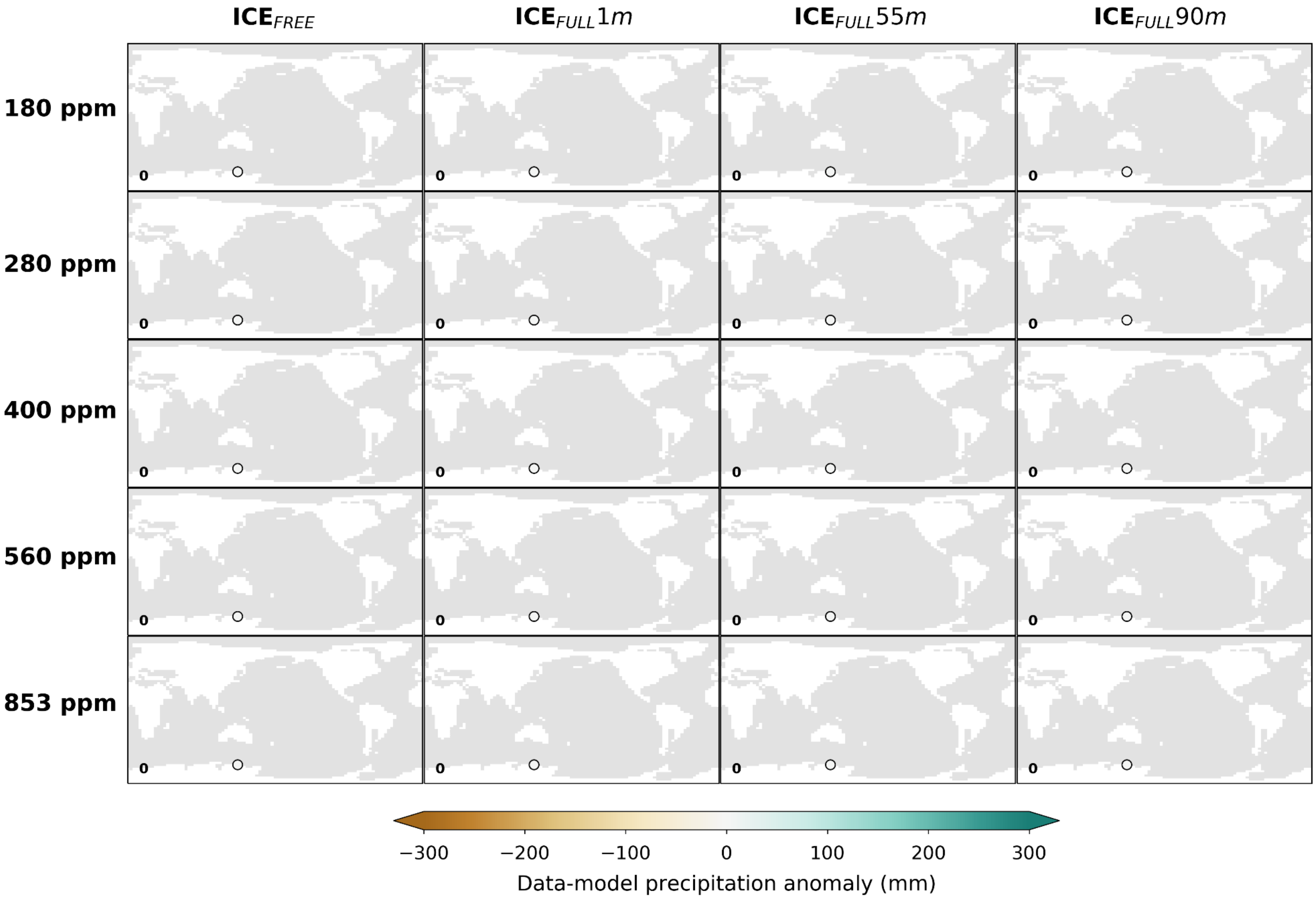

Supplementary Figure S8. Annual mean preciptation model-data comparison for icehouse (13-14.5 Ma) data reconstructions given in Supplementary Table S7. Legend information as in Supplementary Figure S2.

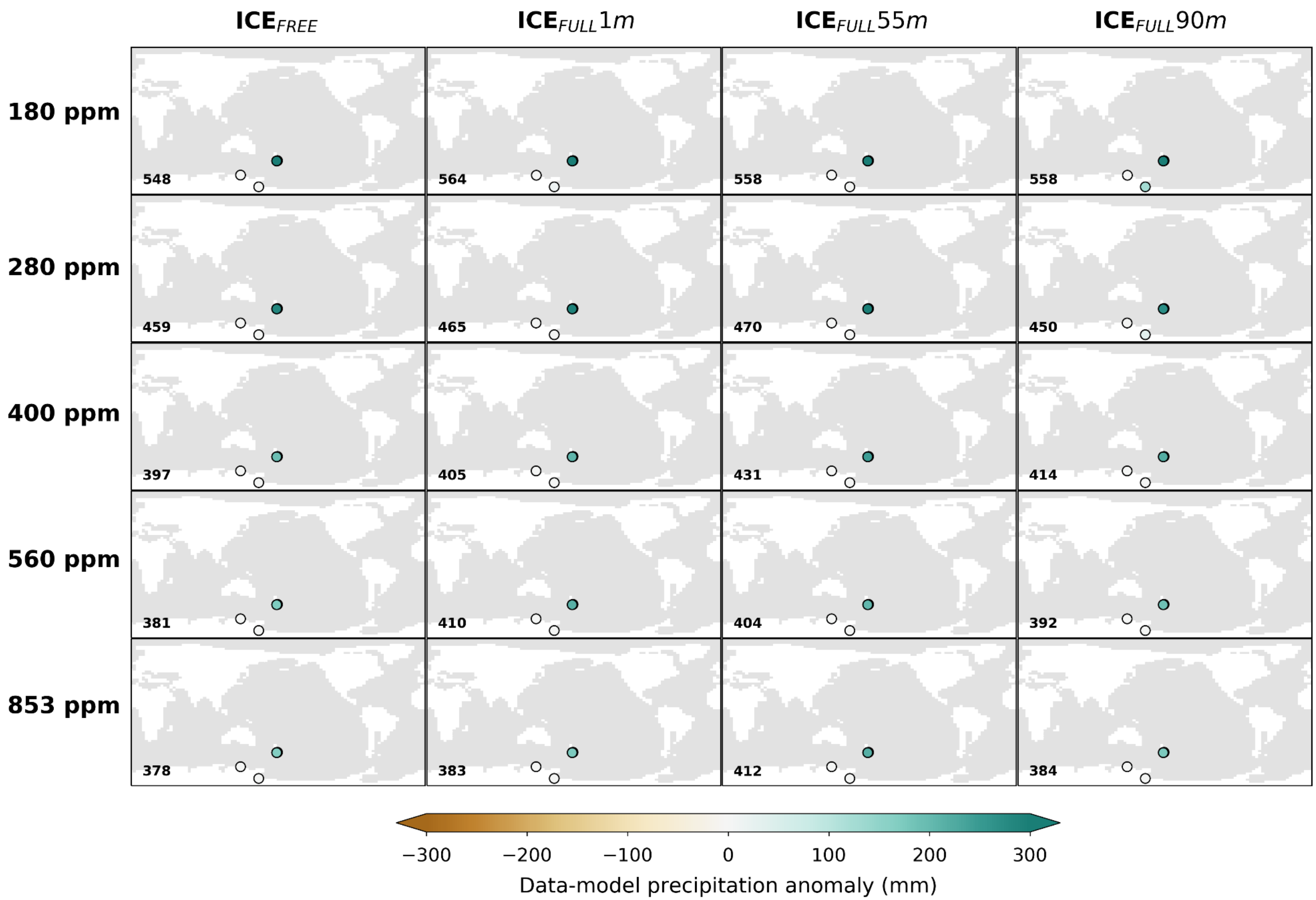

Supplementary Figure S9. Annual mean precipitation model-data comparison for greenhouse (14.5-16.75 Ma) data reconstructions given in Supplementary Table S7. Legend information as in Supplementary Figure S2.

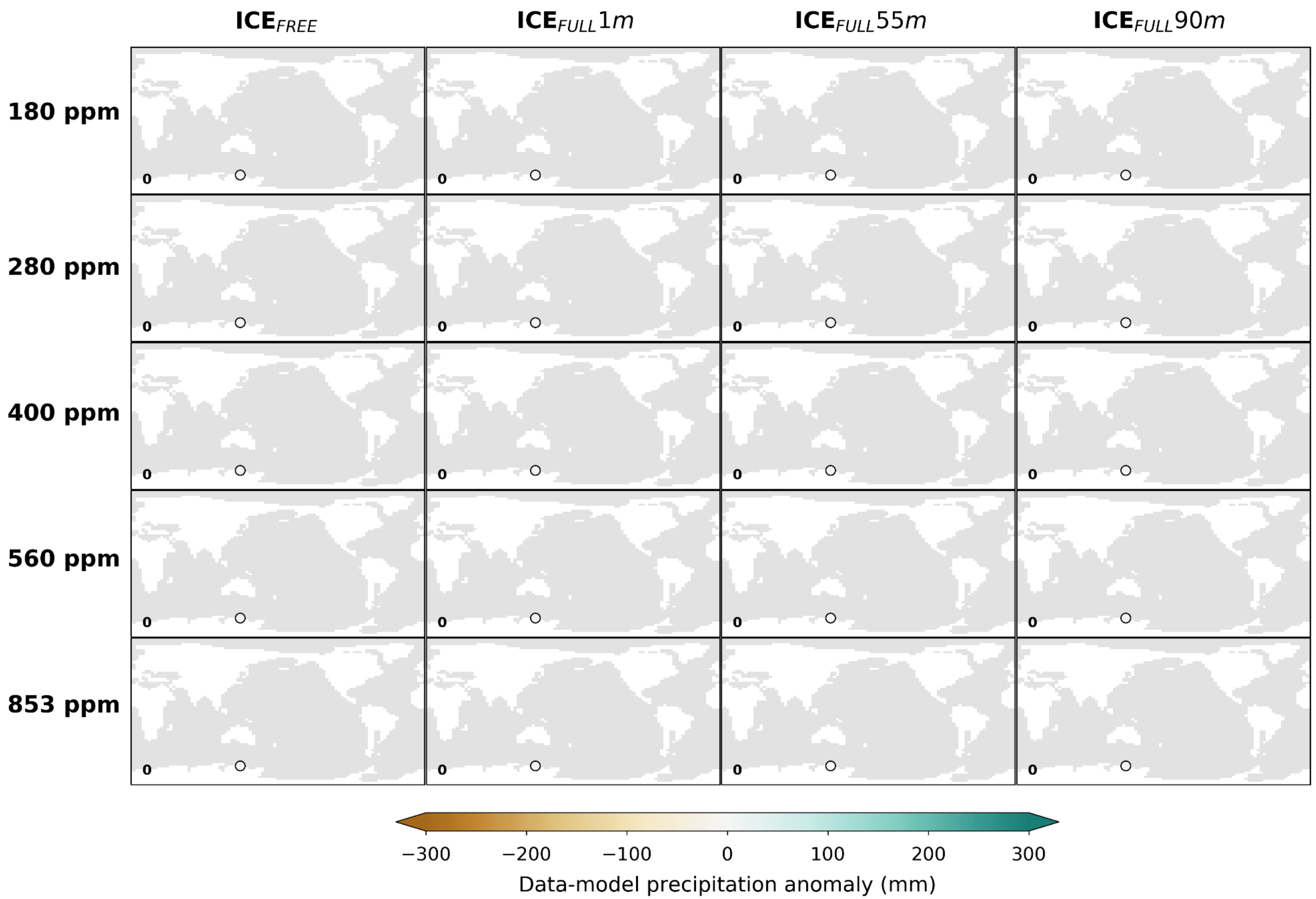

Supplementary Figure S10. Annual mean precipitation model-data comparison for middle Miocene data reconstructions given in Supplementary Table S7 with poor age control. Legend information as in Supplementary Figure S2.

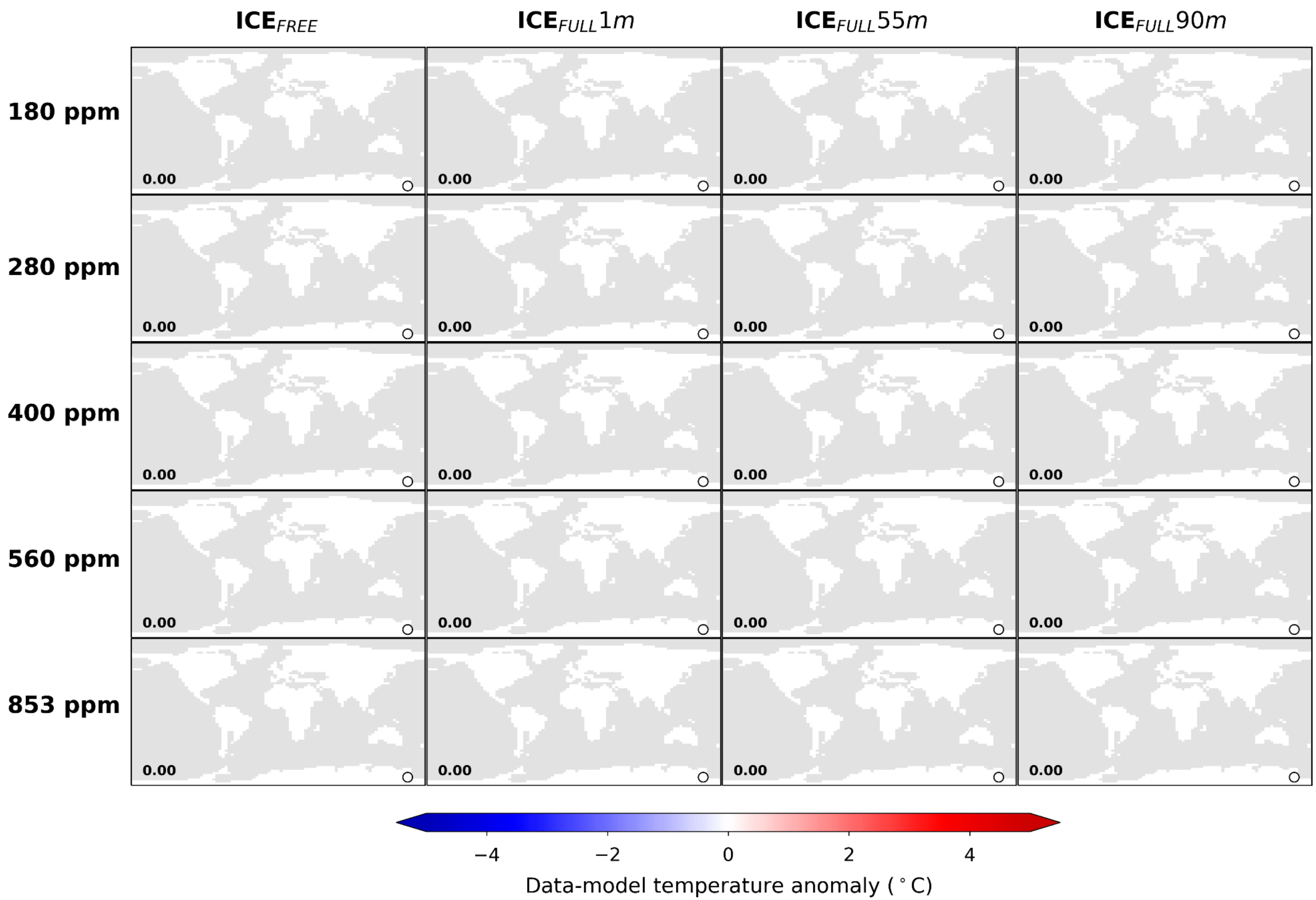

Supplementary Figure S11. Summer (DJF) mean air temperature model-data comparison for greenhouse (14.5-16.75 Ma) data reconstructions given in Supplementary Table S8. Legend information as in Supplementary Figure S2.

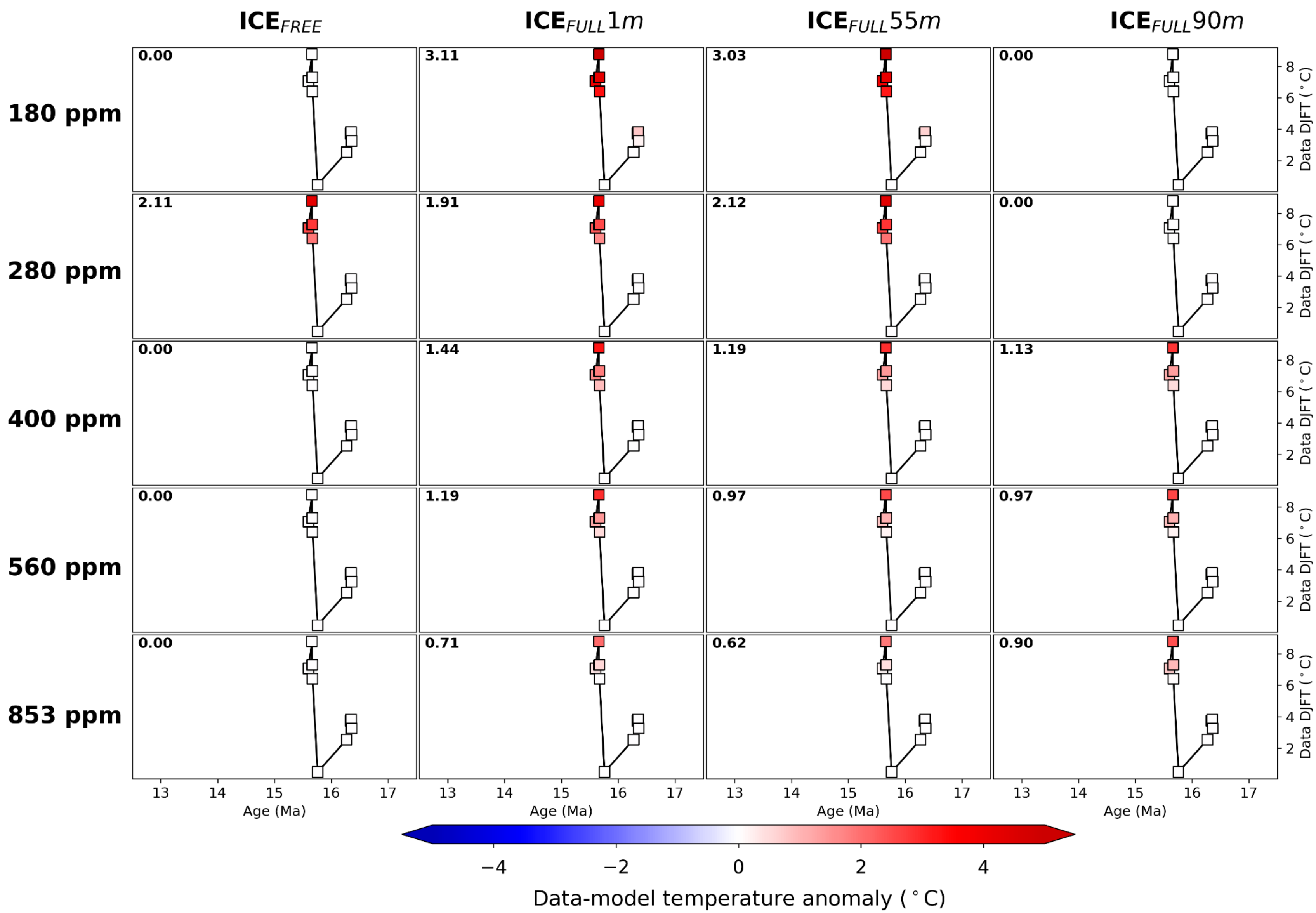

Supplementary Figure S12. Summer (DJF) mean air temperature model-data comparison for middle Miocene data reconstructions for Site AND-2A in the Ross Sea. Data from Feakins et al., 2012[14] as given in Supplementary Table S8. Legend information as in Supplementary Figure S2.

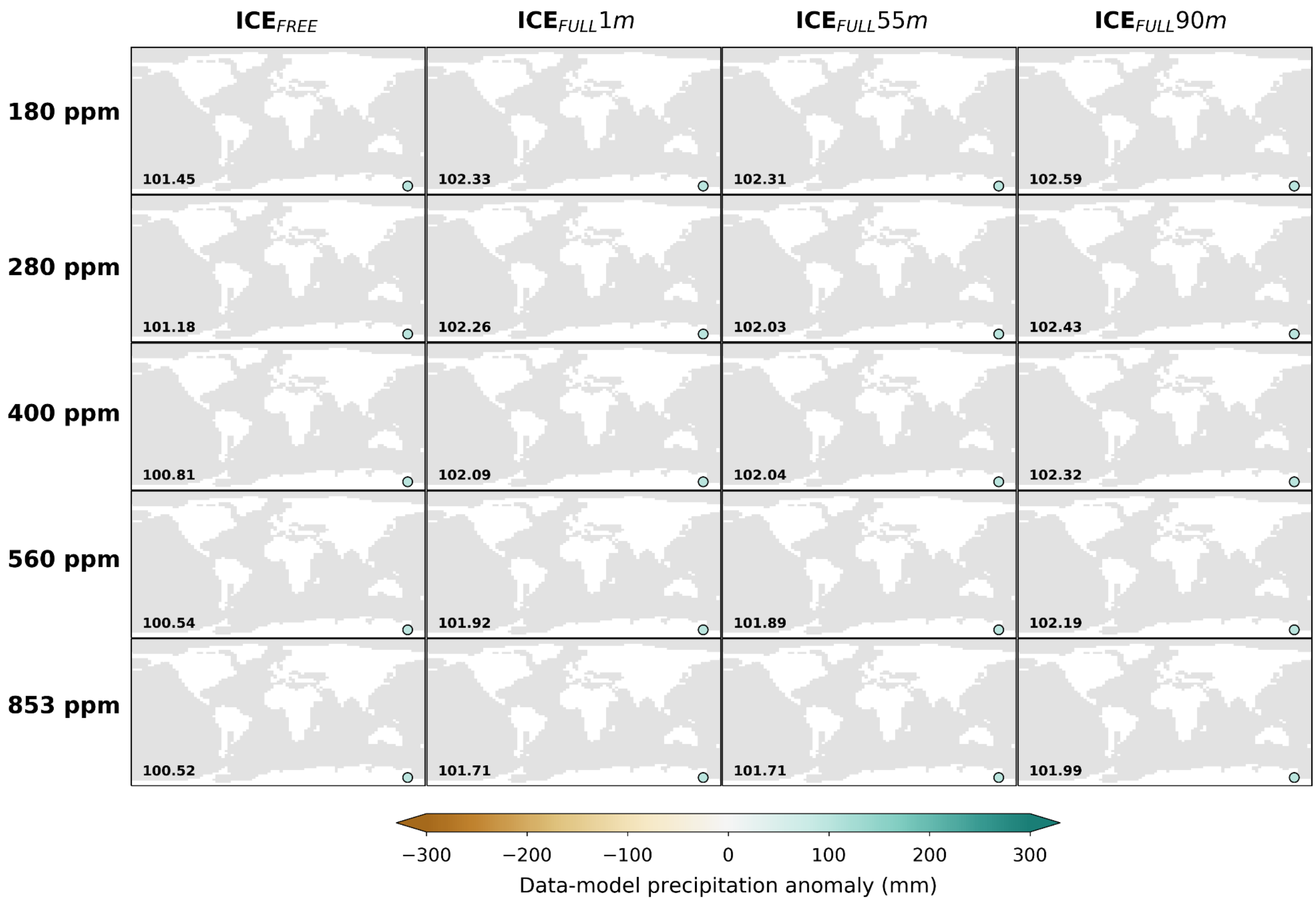

Supplementary Figure S13. Summer (DJF) total precipitation model-data comparison for greenhouse (14.5-16.75 Ma) data reconstructions given in Supplementary Table S9. Legend information as in Supplementary Figure S2.

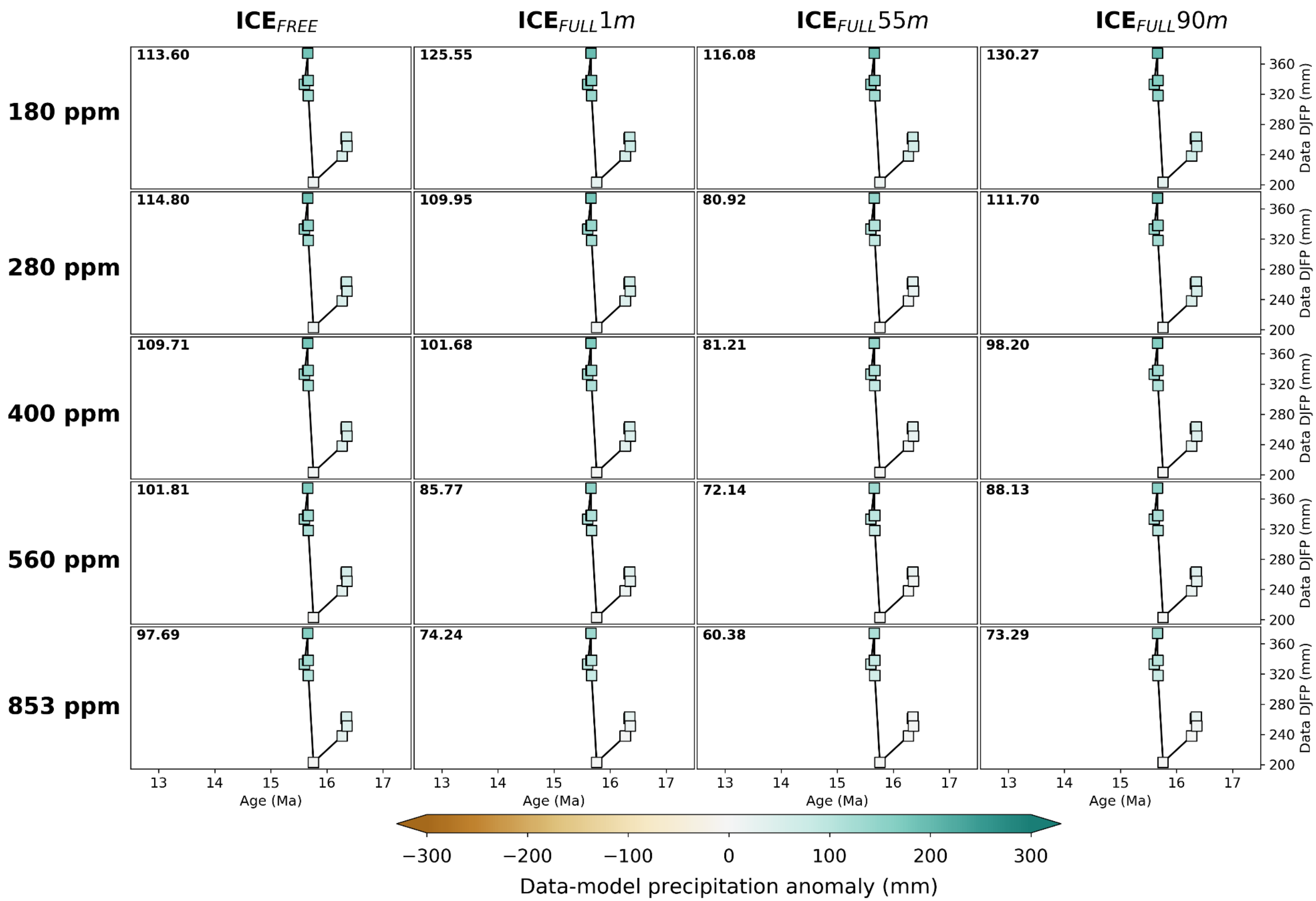

Supplementary Figure S14. Summer (DJF) mean precipitation model-data comparison for middle Miocene data reconstructions for Site AND-2A in the Ross Sea. Data from Feakins et al., 2012[14] as given in Supplementary Table S9. Legend information as in Supplementary Figure S2.

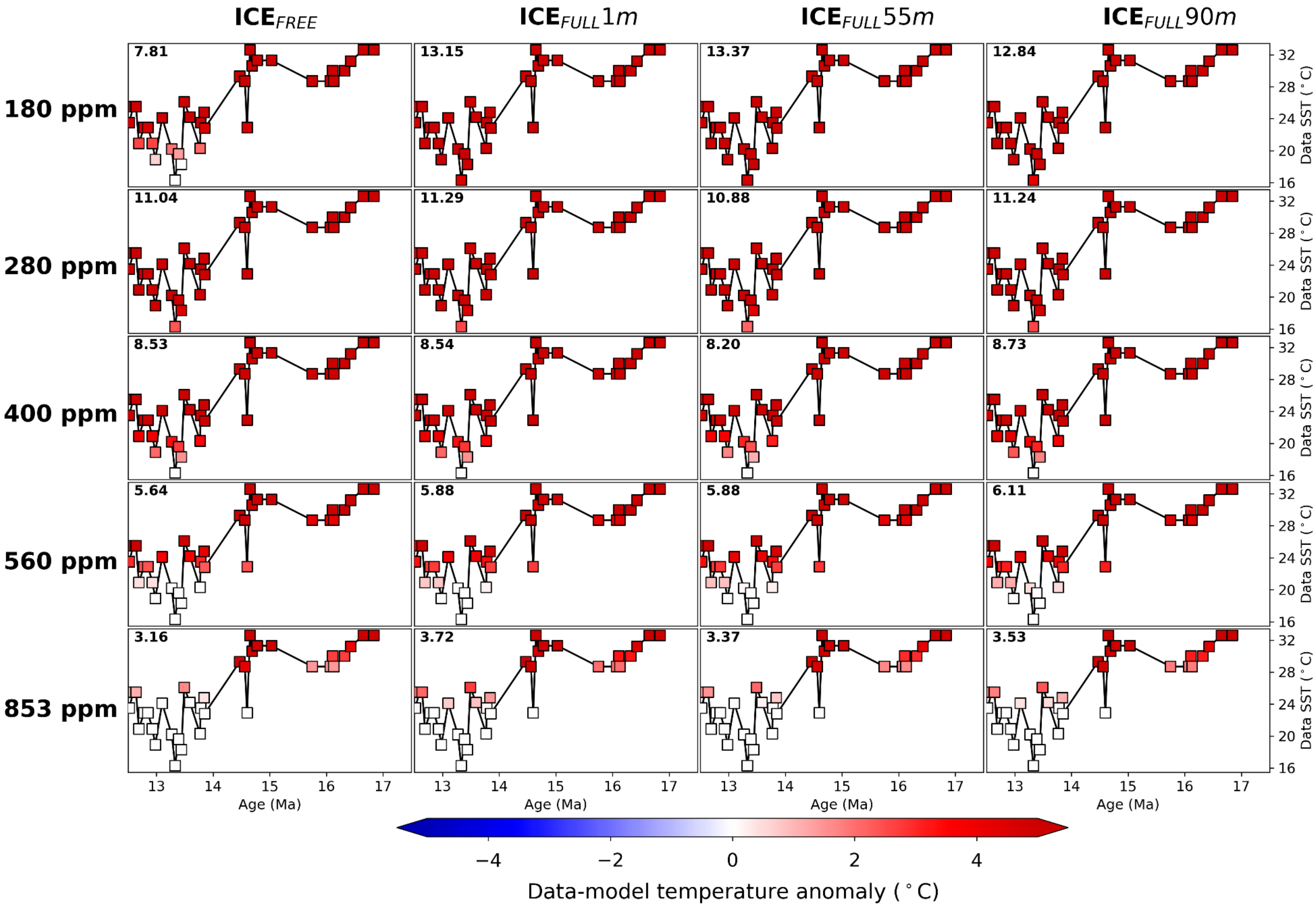

Supplementary Figure S15. Annual mean sea surface temperature model-data comparison for Site 608 in the North Atlantic (TEX$_{86}$). Data from Super et al., 2018[15] as given in Supplementary Table S10. Legend information as in Supplementary Figure S2.

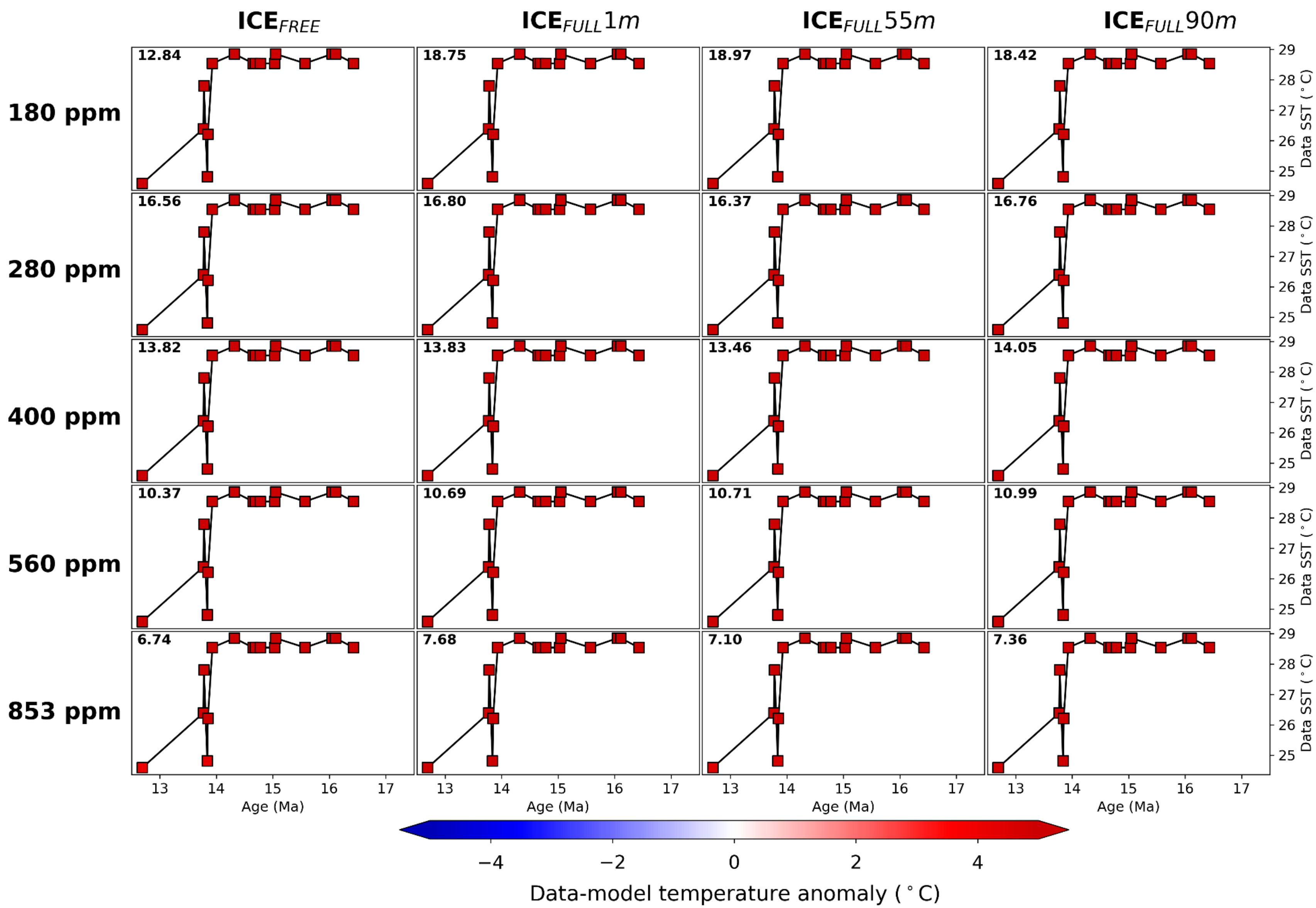

Supplementary Figure S16. Annual mean sea surface temperature model-data comparison for Site 608 in the North Atlantic ($U^{K'}_{37}$). Data from Super et al., 2018[15] as given in Supplementary Table S10. Legend information as in Supplementary Figure S2

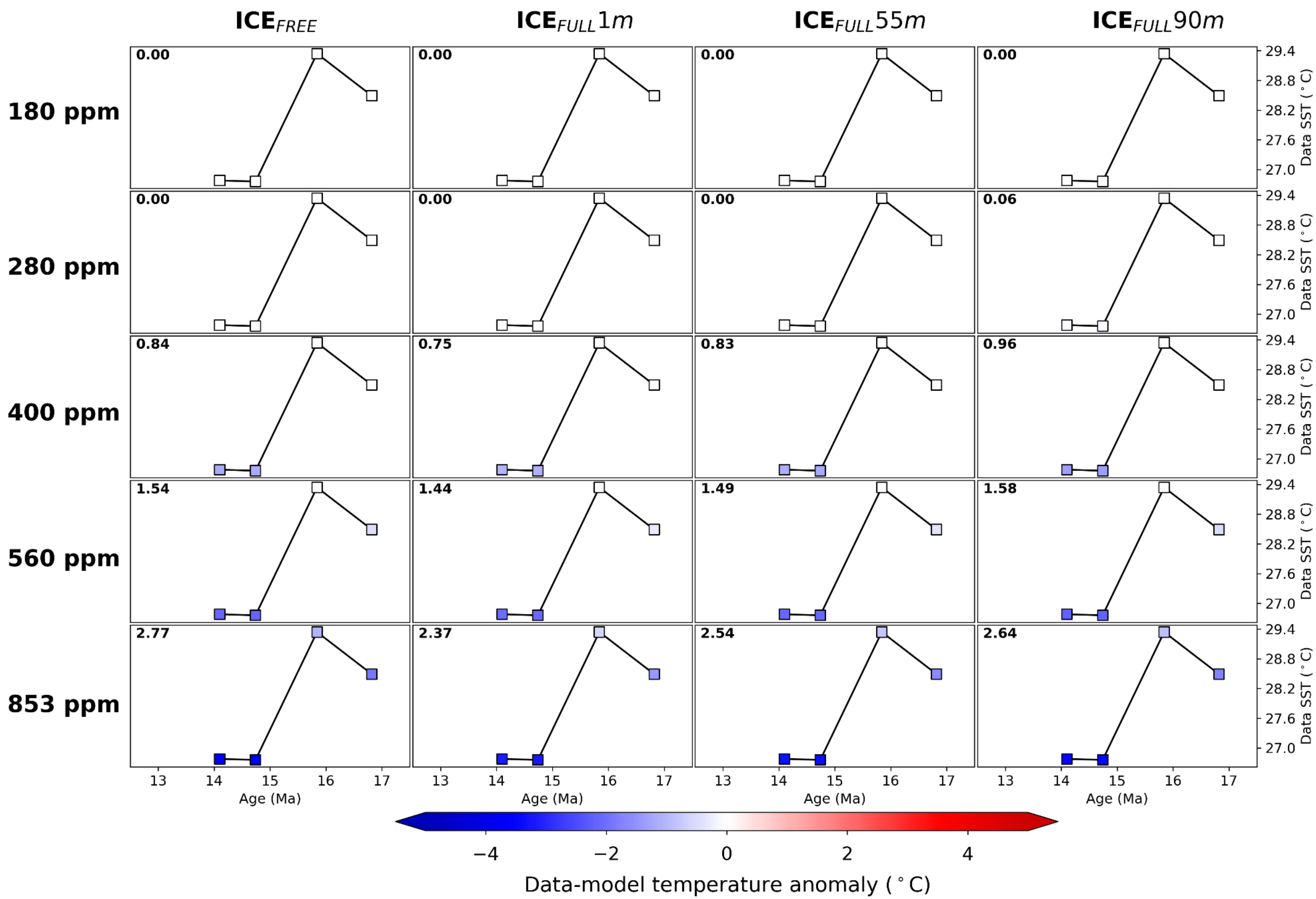

Supplementary Figure S17. Annual mean sea surface temperature model-data comparison for Site 925 in the Tropical Atlantic (TEX$_{86}$). Data from Zhang et al. 2013[16] as given in Supplementary Table S10. Legend information as in Supplementary Figure S2.

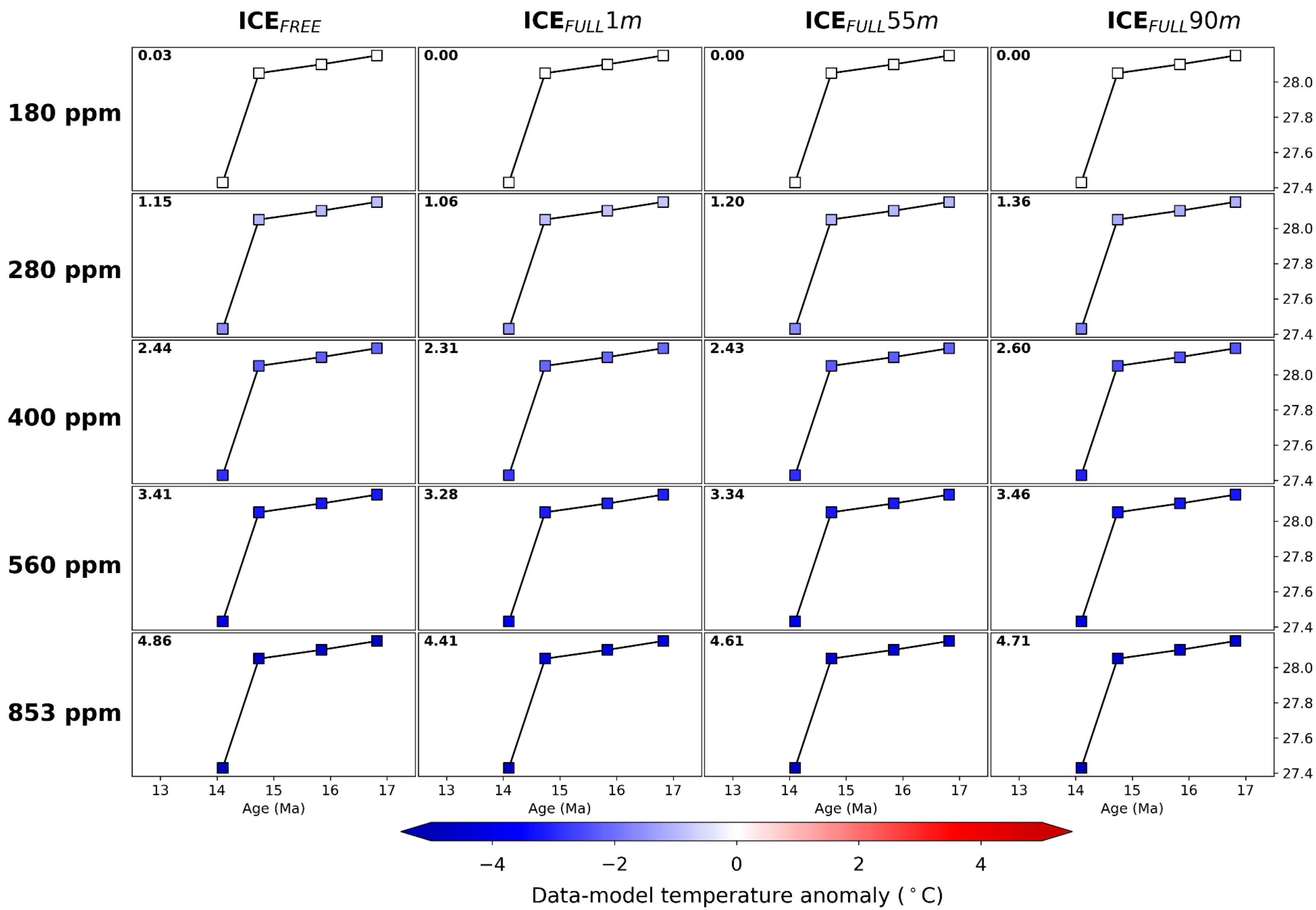

Supplementary Figure S18. Annual mean sea surface temperature model-data comparison for Site 925 in the Tropical Atlantic ($U^{K'}_{37}$). Data from Zhang et al. 2013[16] as given in Supplementary Table S10. Legend information as in Supplementary Figure S2

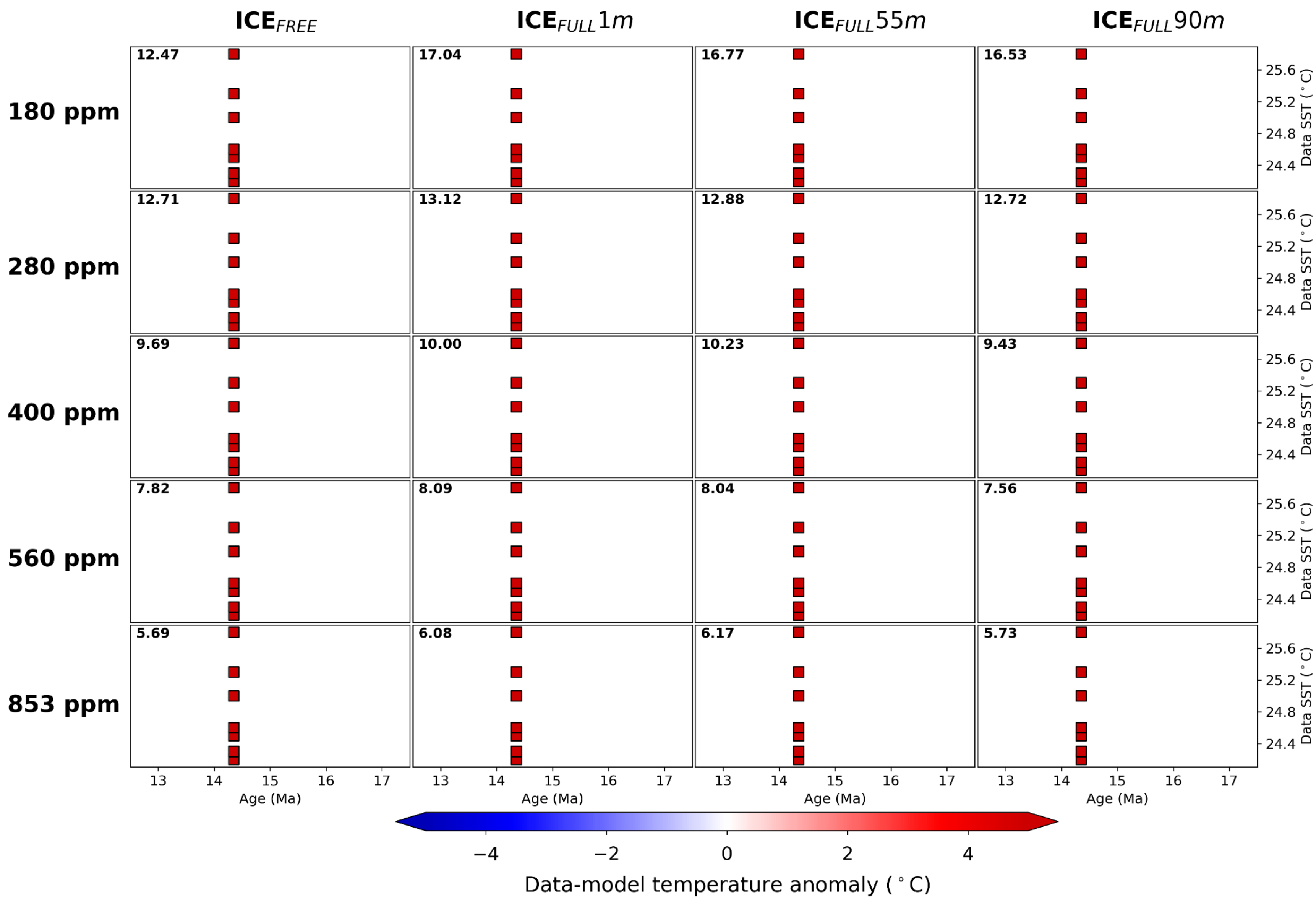

Supplementary Figure S19. Annual mean sea surface temperature model-data comparison for Site LOM-1 in the Mediterranean (Mg/Ca). Data from Scheiner et al. 2018[17] as given in Supplementary Table S10. Legend information as in Supplementary Figure S2.

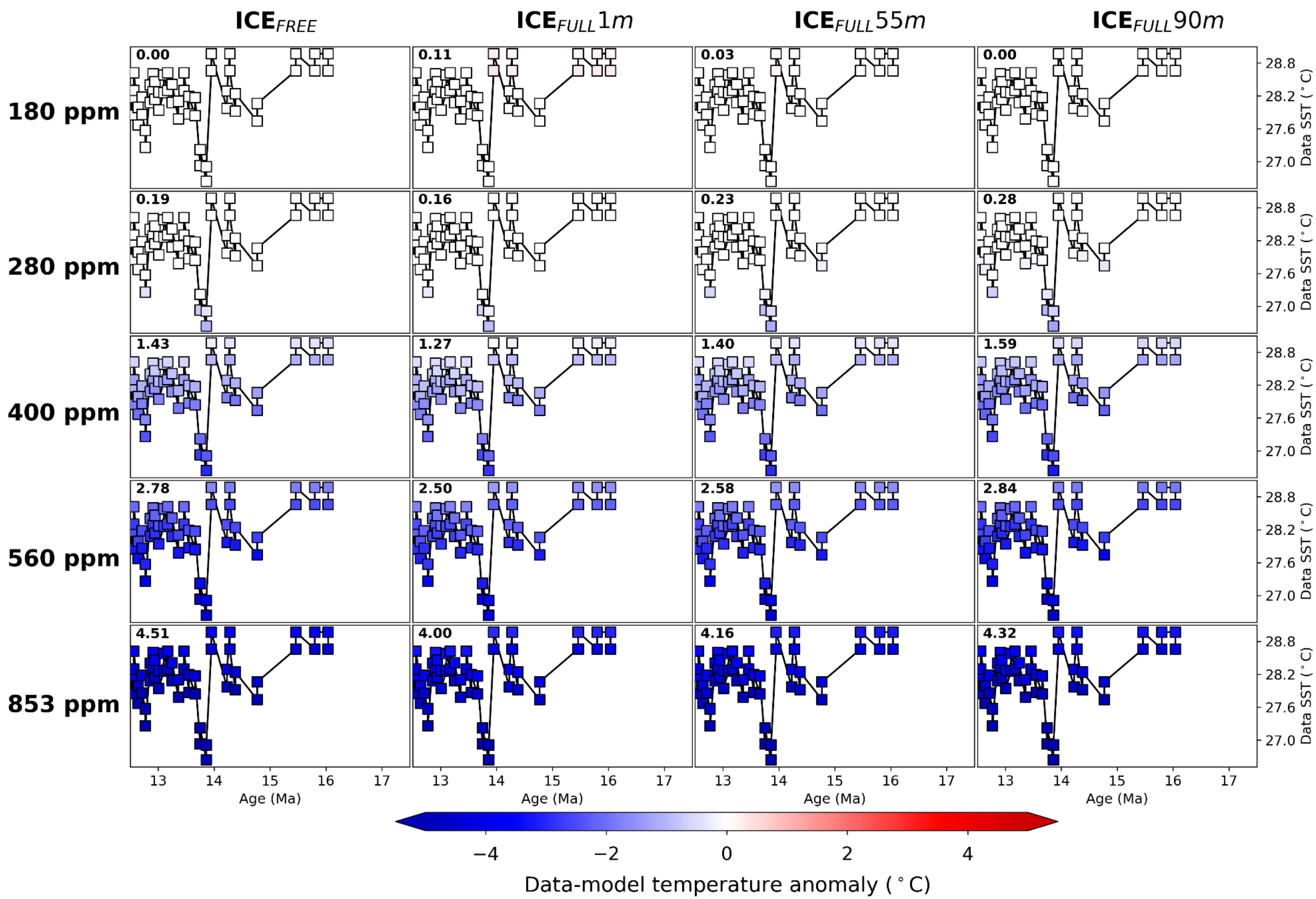

Supplementary Figure S20. Annual mean sea surface temperature model-data comparison for Site U1338 in the Tropical Pacific ($U^{K'}_{37}$). Data from Rousselle et al., 2013[18] as given in Supplementary Table S10. Legend information as in Supplementary Figure S2.

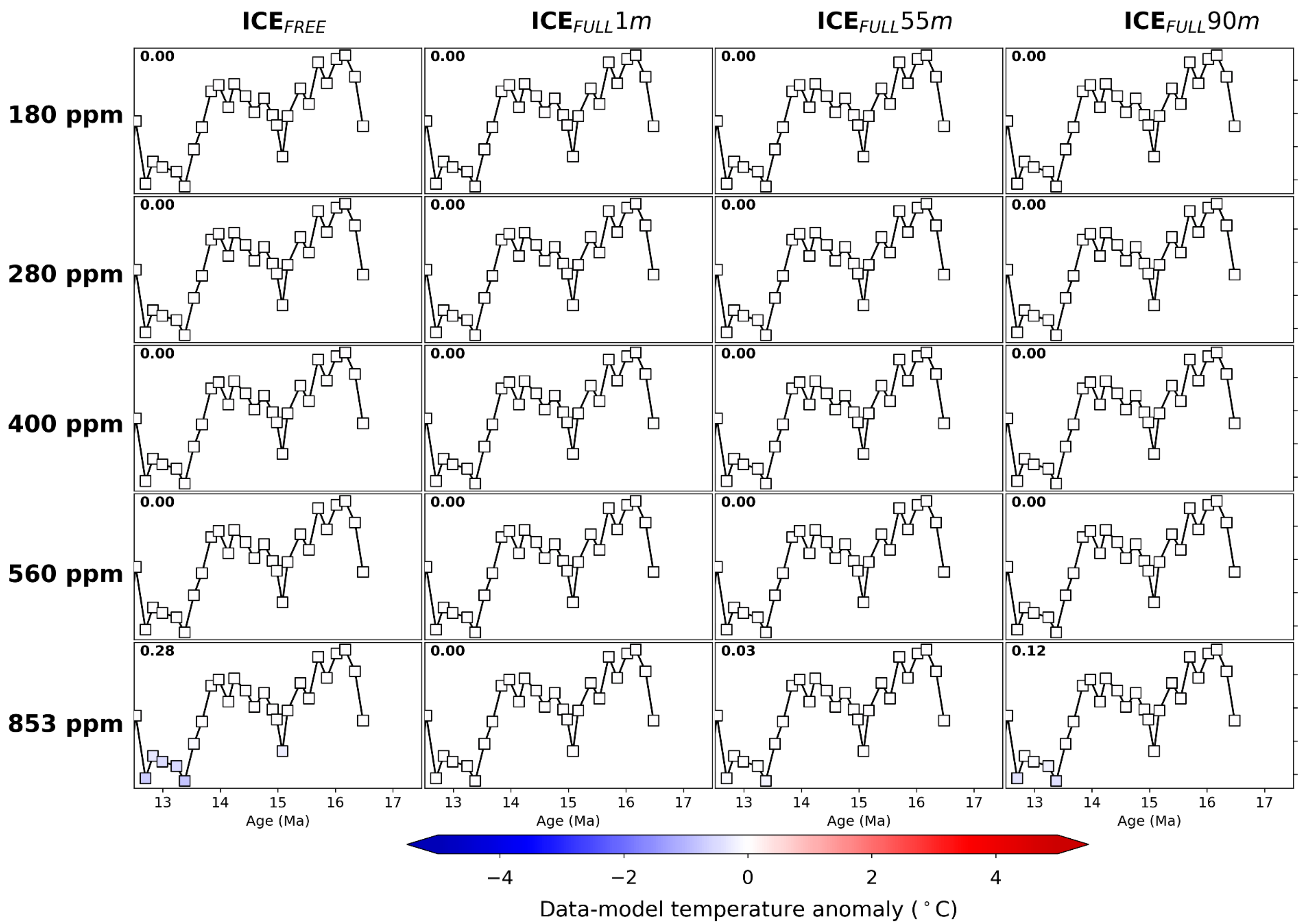

Supplementary Figure S21. Annual mean sea surface temperature model-data comparison for Site 806 in the Tropical Pacific (Mg/Ca). Data from Sosdian and Lear, submitted as given in Supplementary Table S10. Legend information as in Supplementary Figure S2.

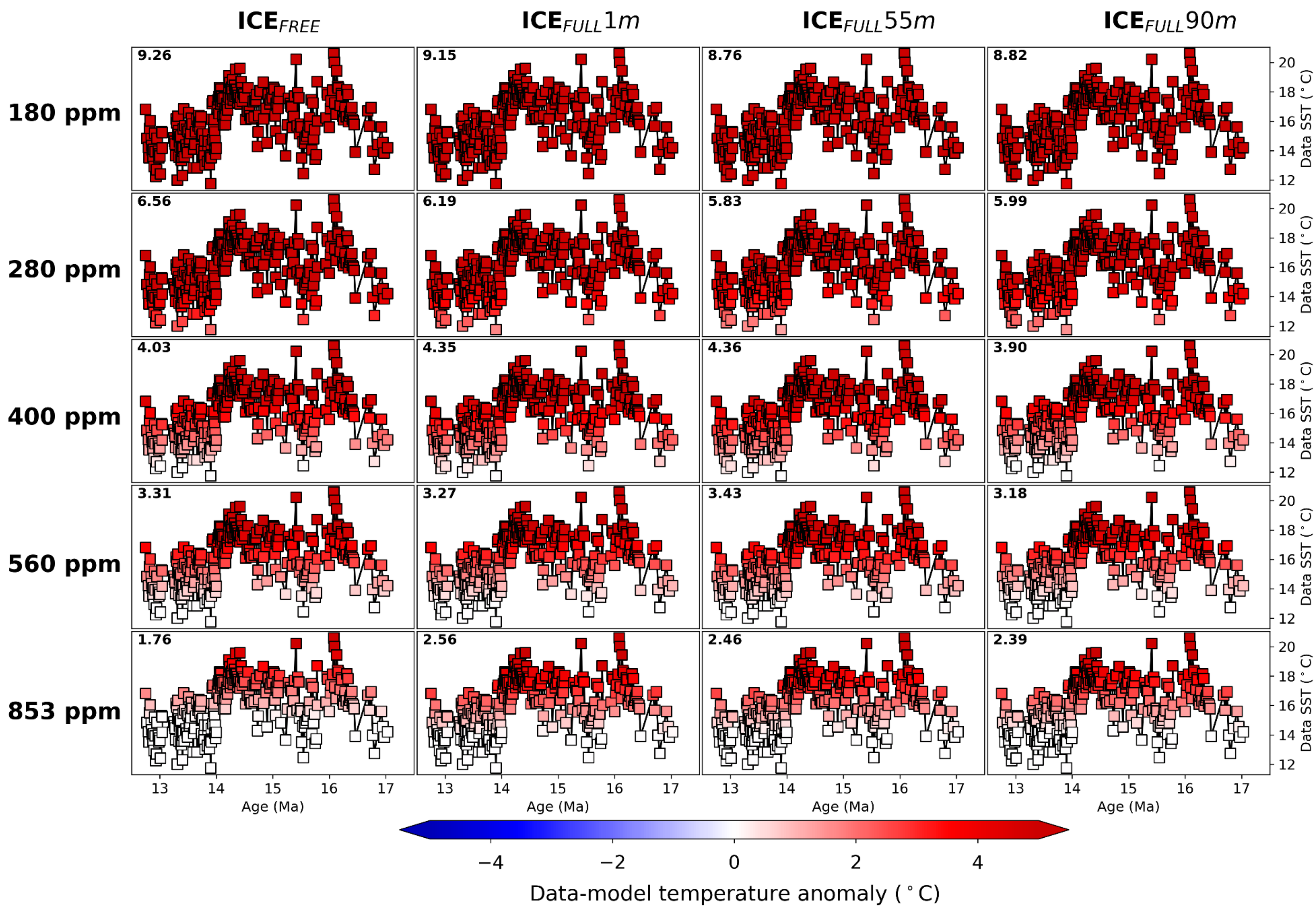

Supplementary Figure S22. Annual mean sea surface temperature model-data comparison for Site 1171 in the Southern Ocean (Mg/Ca). Data from Shevenell et al., 2004[19] as given in Supplementary Table S10. Legend information as in Supplementary Figure S2.

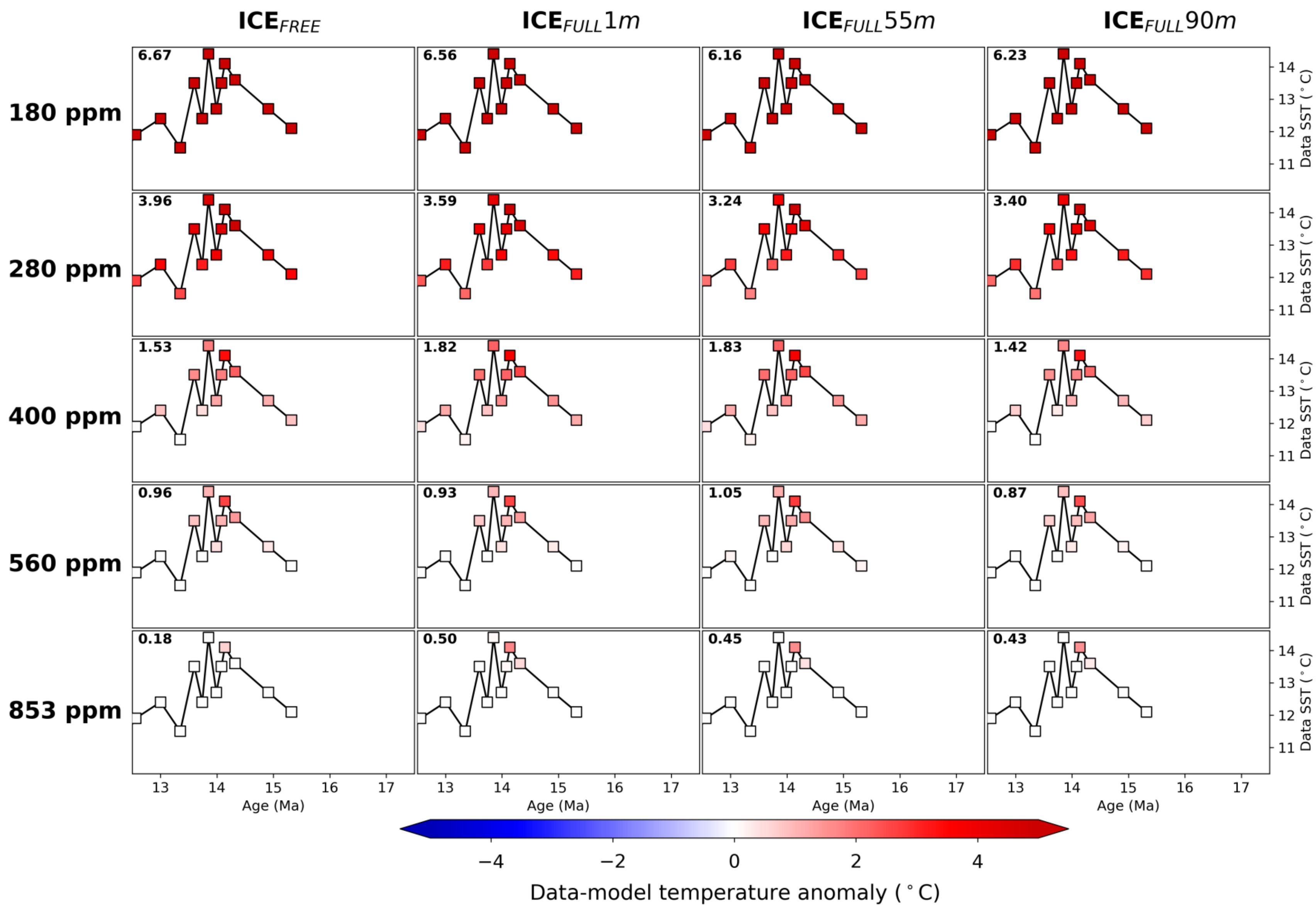

Supplementary Figure S23. Annual mean sea surface temperature model-data comparison for Site 1171 in the Southern Ocean (Δ47). Data from Leutert et al., 2020[20] as given in Supplementary Table S10. Legend information as in Supplementary Figure S2.

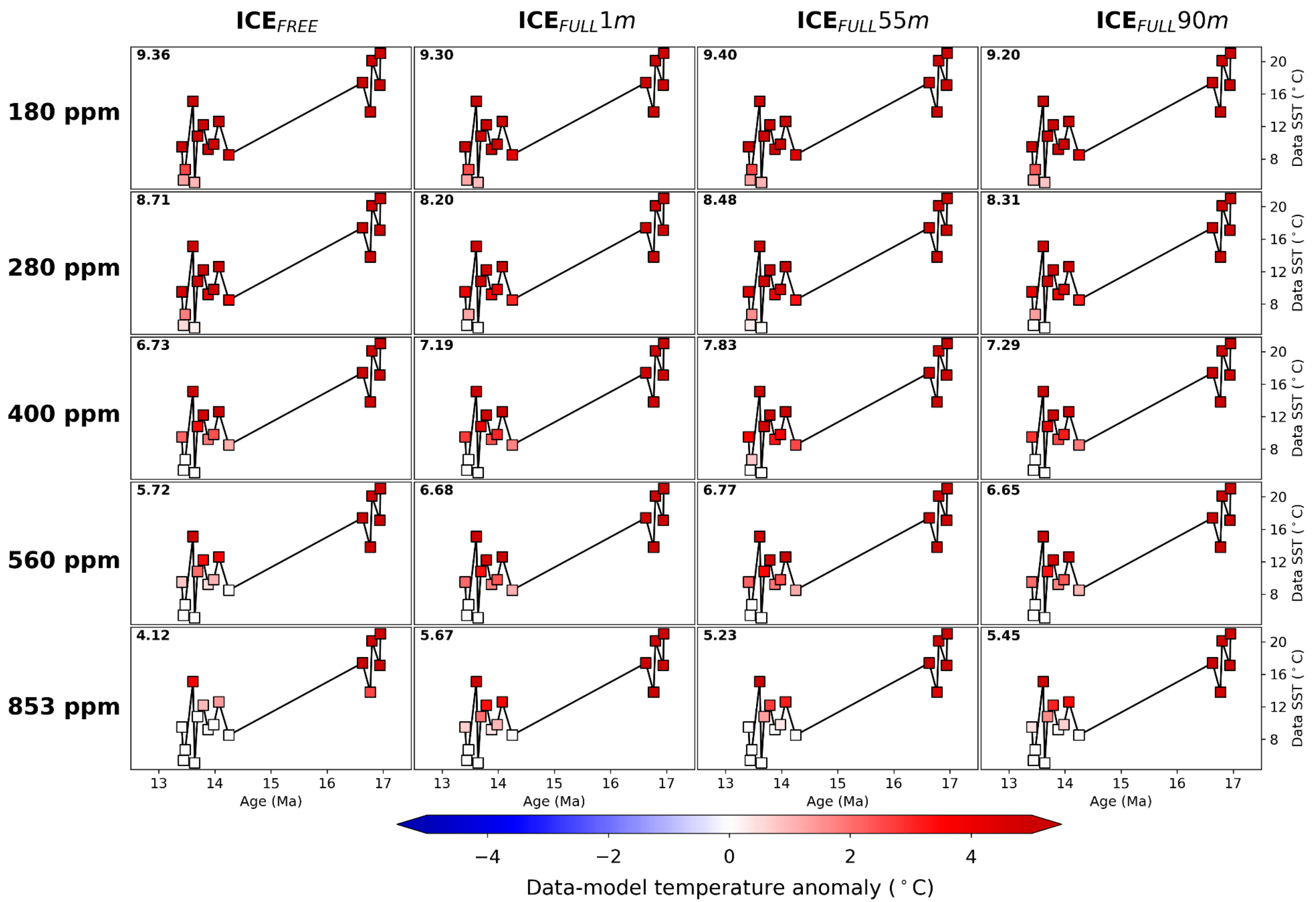

Supplementary Figure S24. Annual mean sea surface temperature model-data comparison for Site U1356 in the Southern Ocean (TEX^{L}_{86}). Data from Sangiorgi et al., 2018[13] as given in Supplementary Table S10. Legend information as in Supplementary Figure S2.

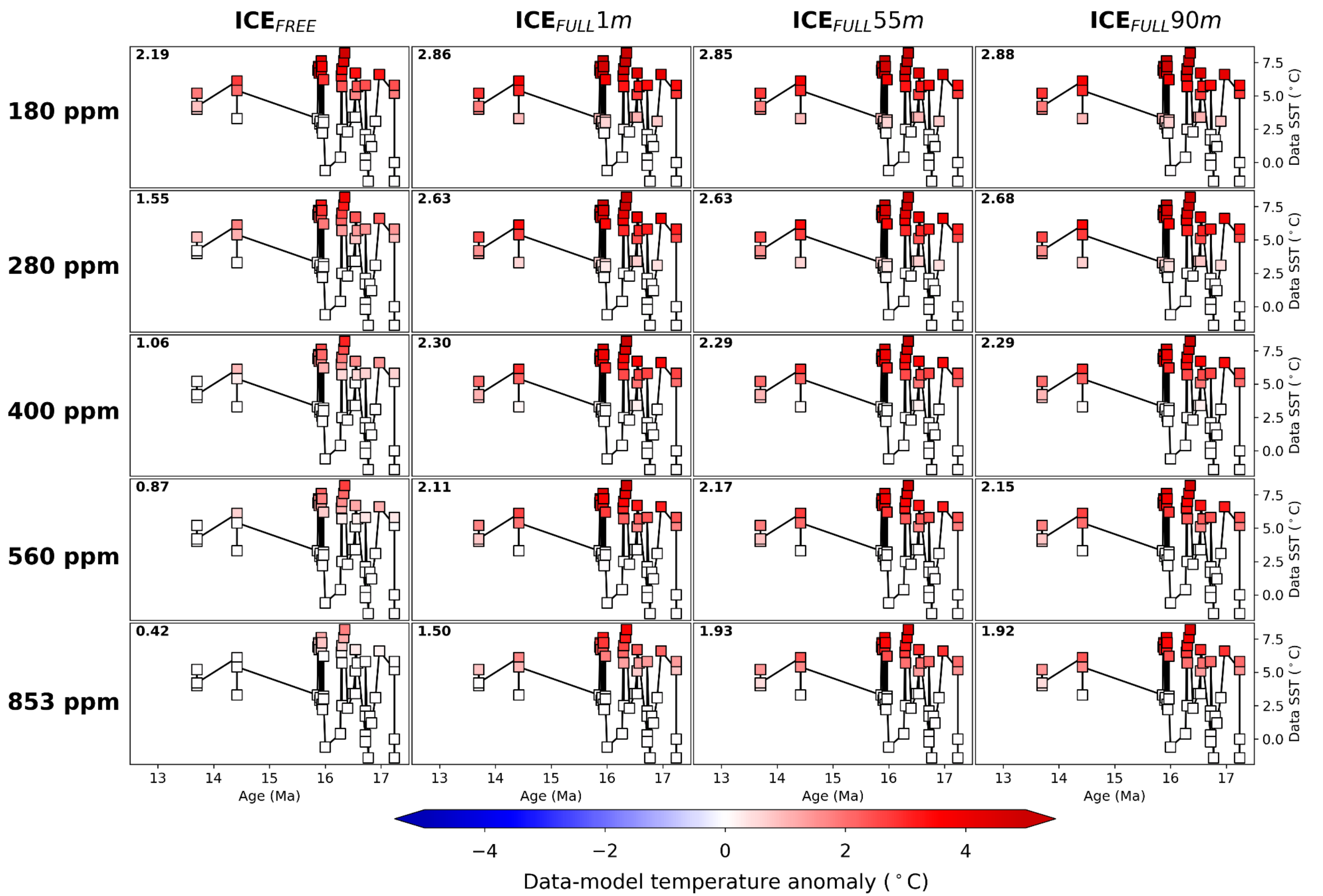

Supplementary Figure S25. Annual mean sea surface temperature model-data comparison for Site AND-2A in the Ross Sea (TEX$^{L}_{86}$). Data from Levy et al., 2016[21] as given in Supplementary Table S10. Legend information as in Supplementary Figure S2.

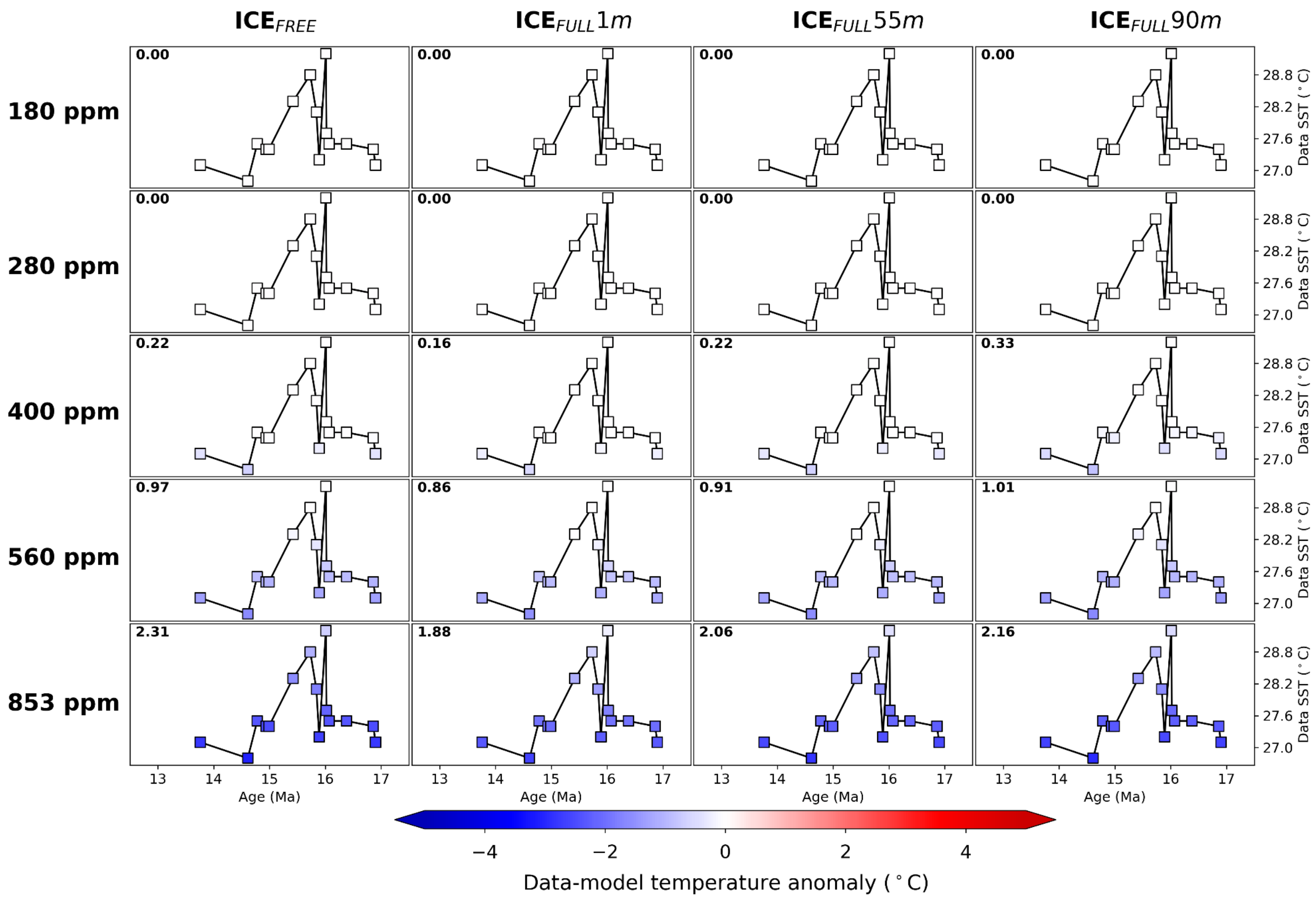

Supplementary Figure S26. Annual mean sea surface temperature model-data comparison for Site 926 in the Tropical Atlantic (Mg/Ca). Data from Sosdian et al., 2018[22] and Foster et al., 2012[23] as given in Supplementary Table S10. Legend information as in Supplementary Figure S2.

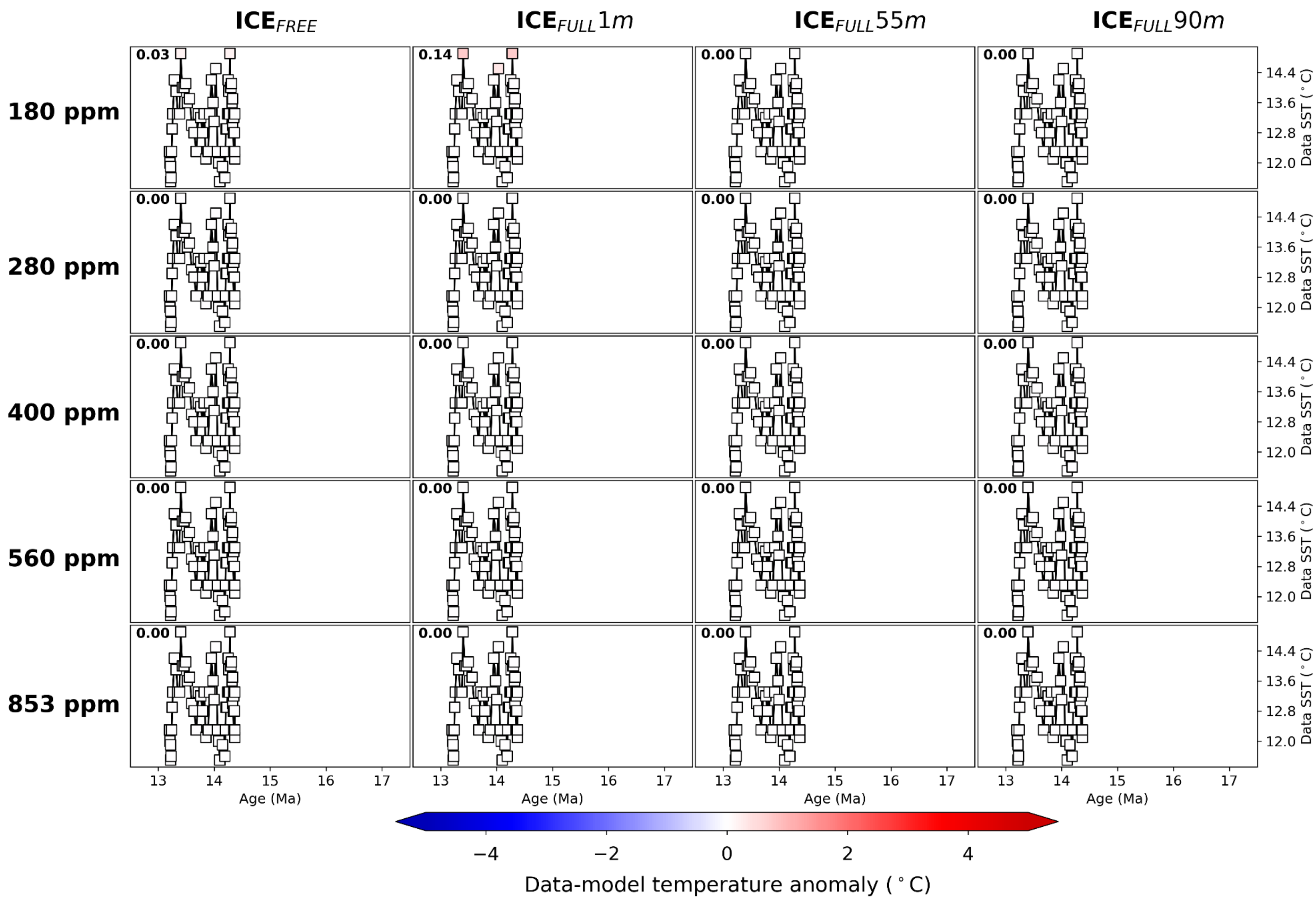

Supplementary Figure S27. Annual mean sea surface temperature model-data comparison for Site 1092 in the Southern Ocean (Mg/Ca). Data from Kuhnert et al., 2009[24] as given in Supplementary Table S10. Legend information as in Supplementary Figure S2.

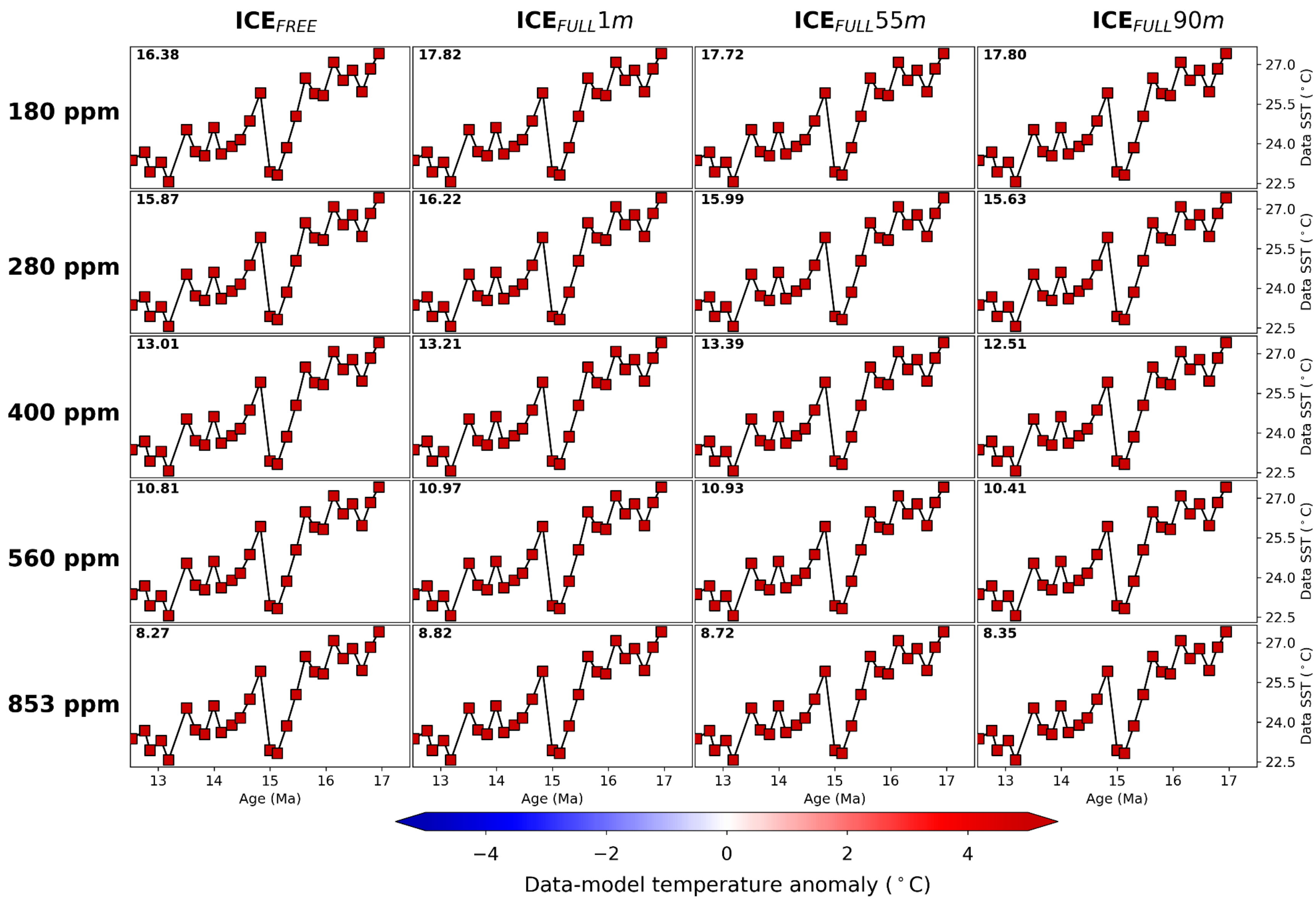

Supplementary Figure S28. Annual mean sea surface temperature model-data comparison for Site 982 in the North Atlantic (TEX$_{86}$). Data from Super et al., 2020[25] as given in Supplementary Table S10. Legend information as in Supplementary Figure S2.

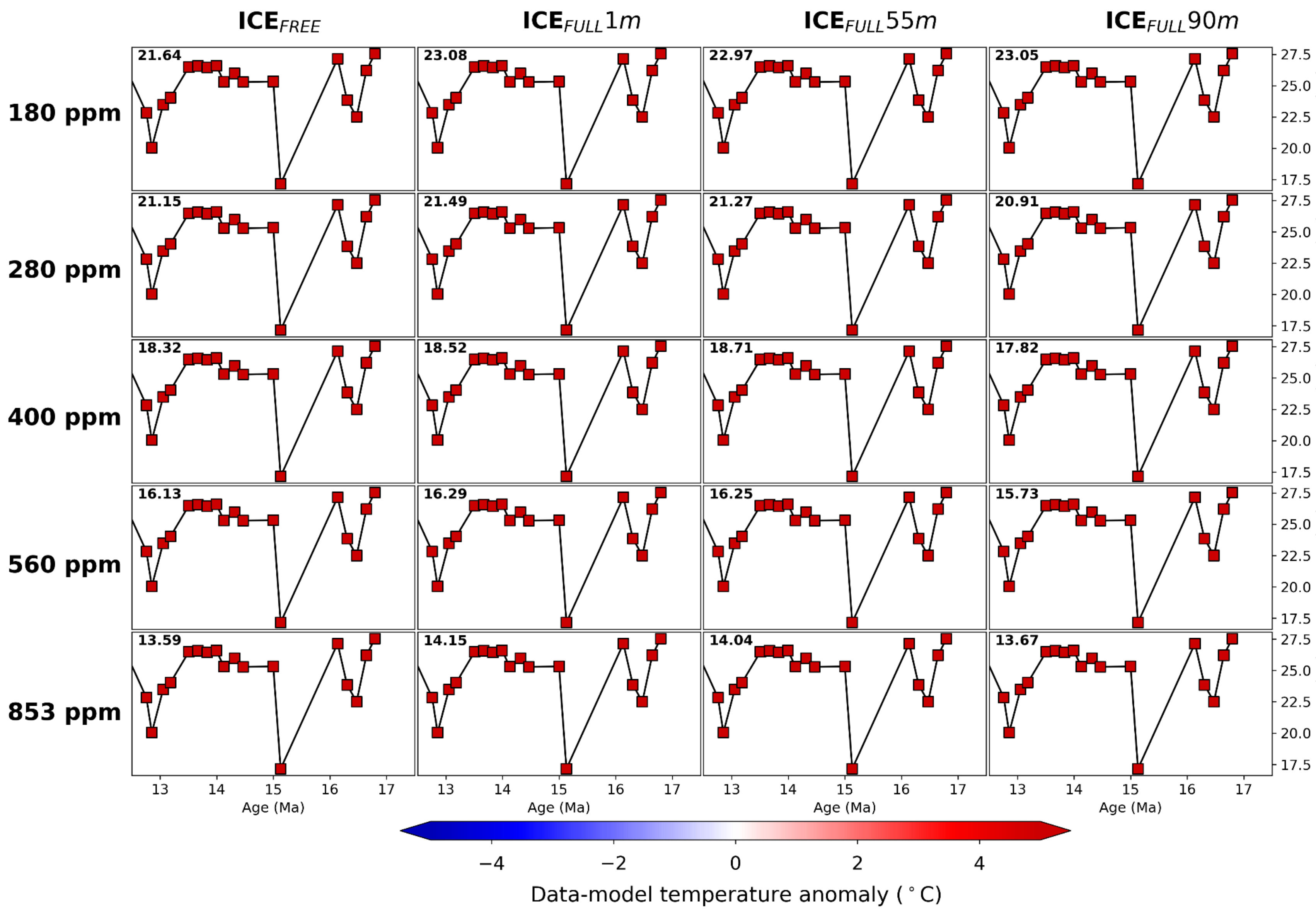

Supplementary Figure S29. Annual mean sea surface temperature model-data comparison for Site 982 in the North Atlantic ($U^{K'}_{37}$). Data from Super et al., 2020[25] as given in Supplementary Table S10. Legend information as in Supplementary Figure S2.

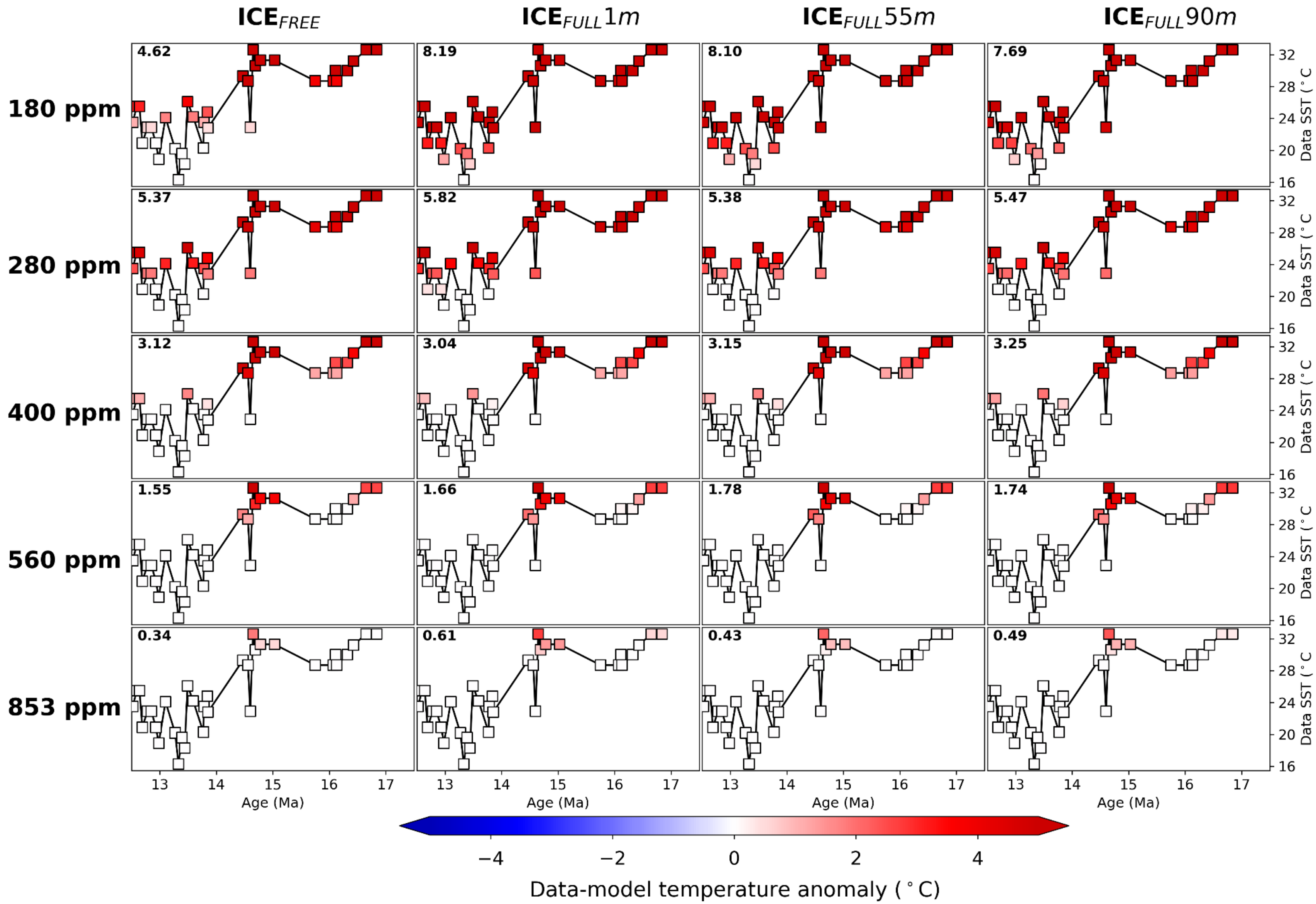

Supplementary Figure S30. Maximum sea surface temperature model-data comparison for Site 608 in the North Atlantic (TEX$_{86}$). Data from Super et al., 2018[15] as given in Supplementary Table S10. Legend information as in Supplementary Figure S2.

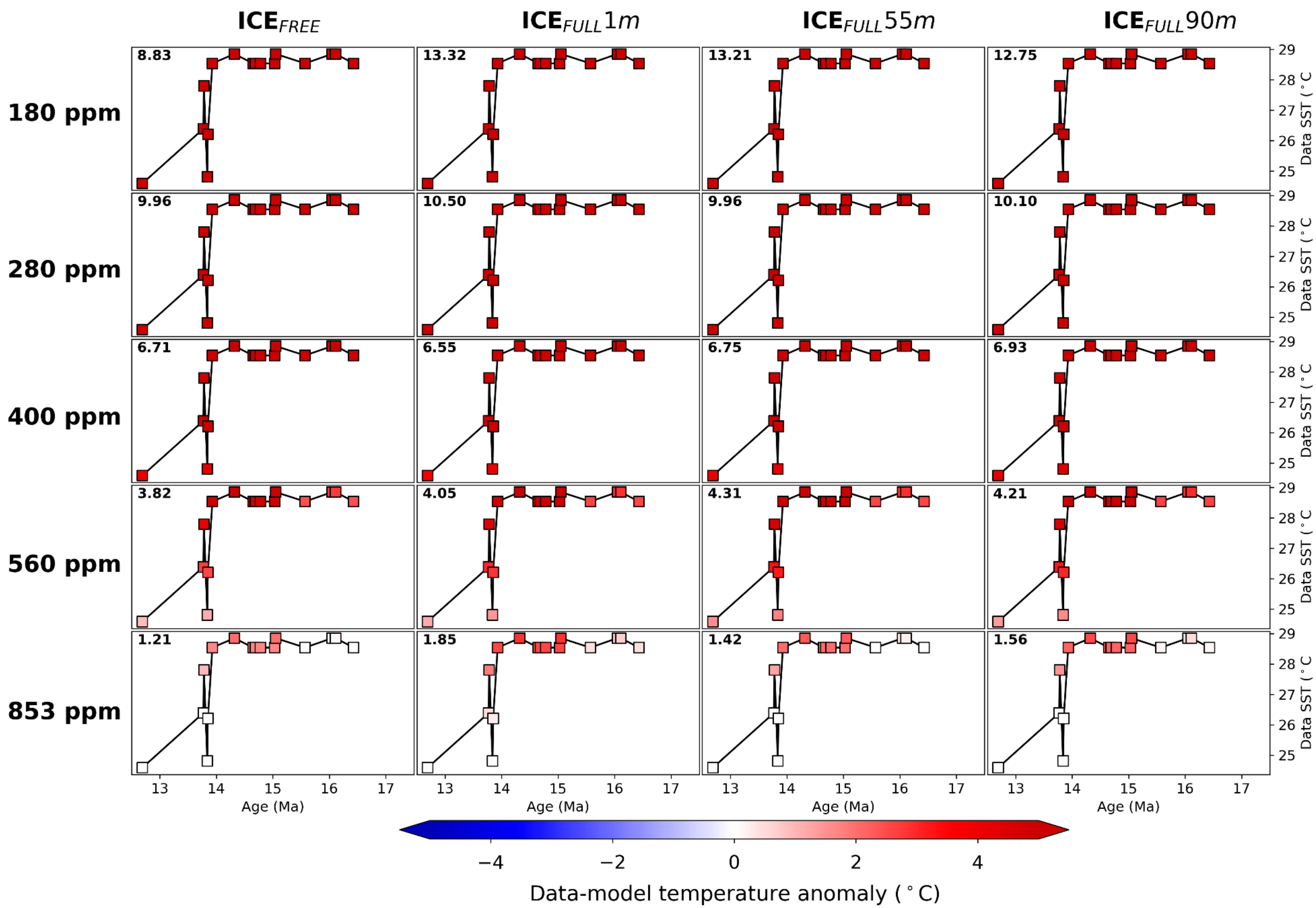

Supplementary Figure S31. Maximum sea surface temperature model-data comparison for Site 608 in the North Atlantic ($U^{K'}_{37}$). Data from Super et al., 2018[15] as given in Supplementary Table S10. Legend information as in Supplementary Figure S2

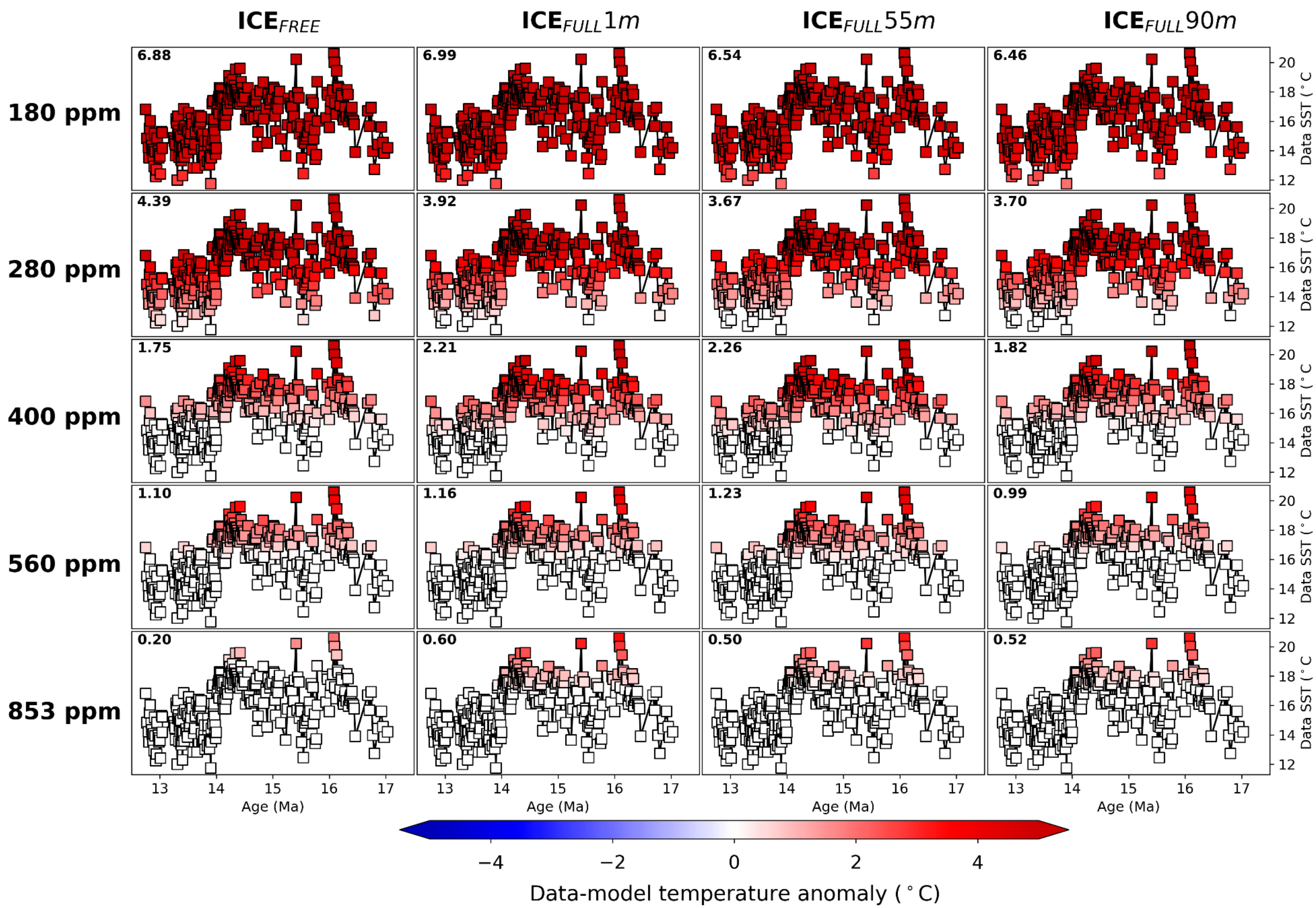

Supplementary Figure S32. Maximum sea surface temperature model-data comparison for Site 1171 in the Southern Ocean (Mg/Ca). Data from Shevenell et al., 2004[19] as given in Supplementary Table S10. Legend information as in Supplementary Figure S2.

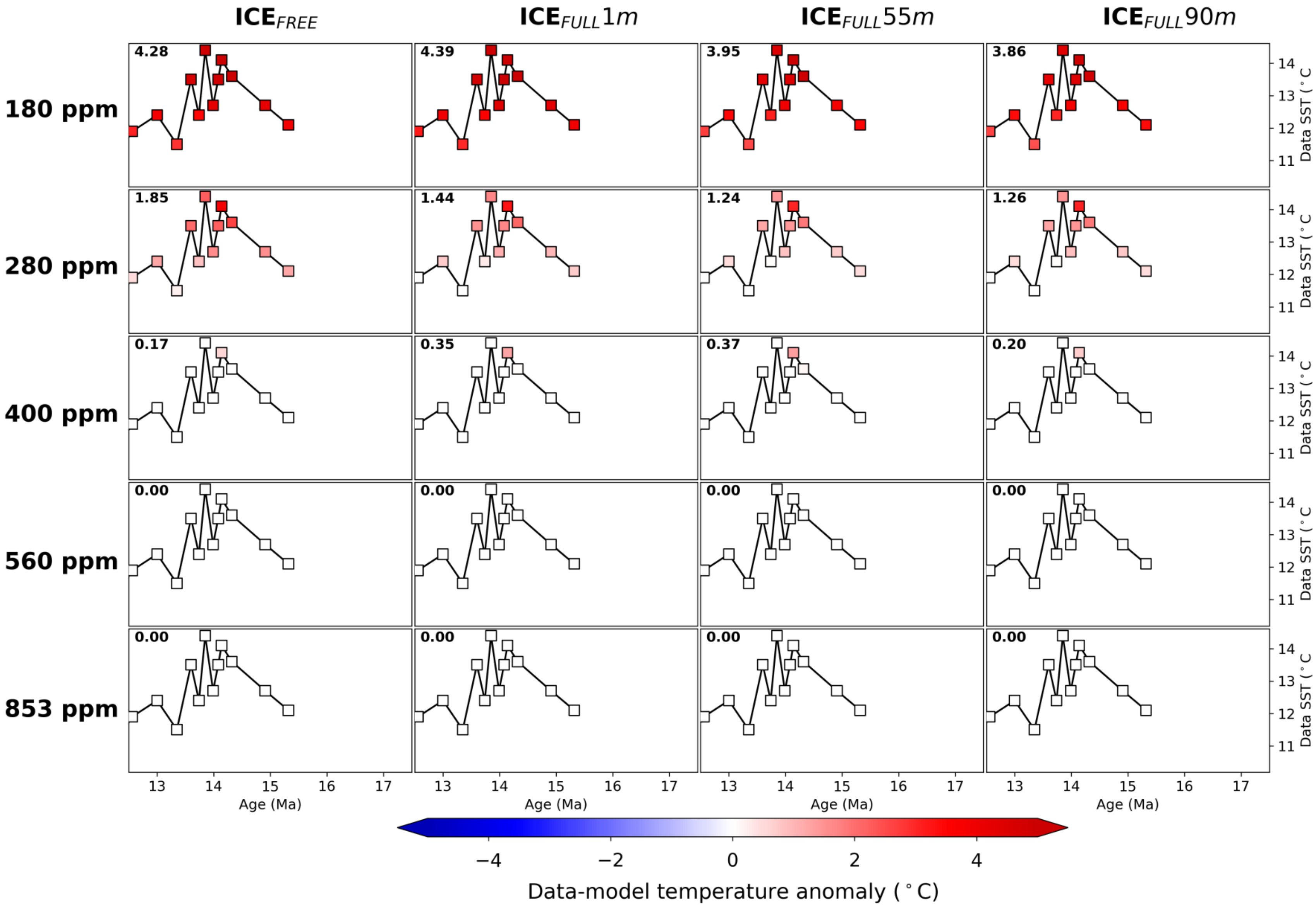

Supplementary Figure S33. Maximum sea surface temperature model-data comparison for Site 1171 in the Southern Ocean (Δ47). Data from Leutert et al., 2020[20] as given in Supplementary Table S10. Legend information as in Supplementary Figure S2.

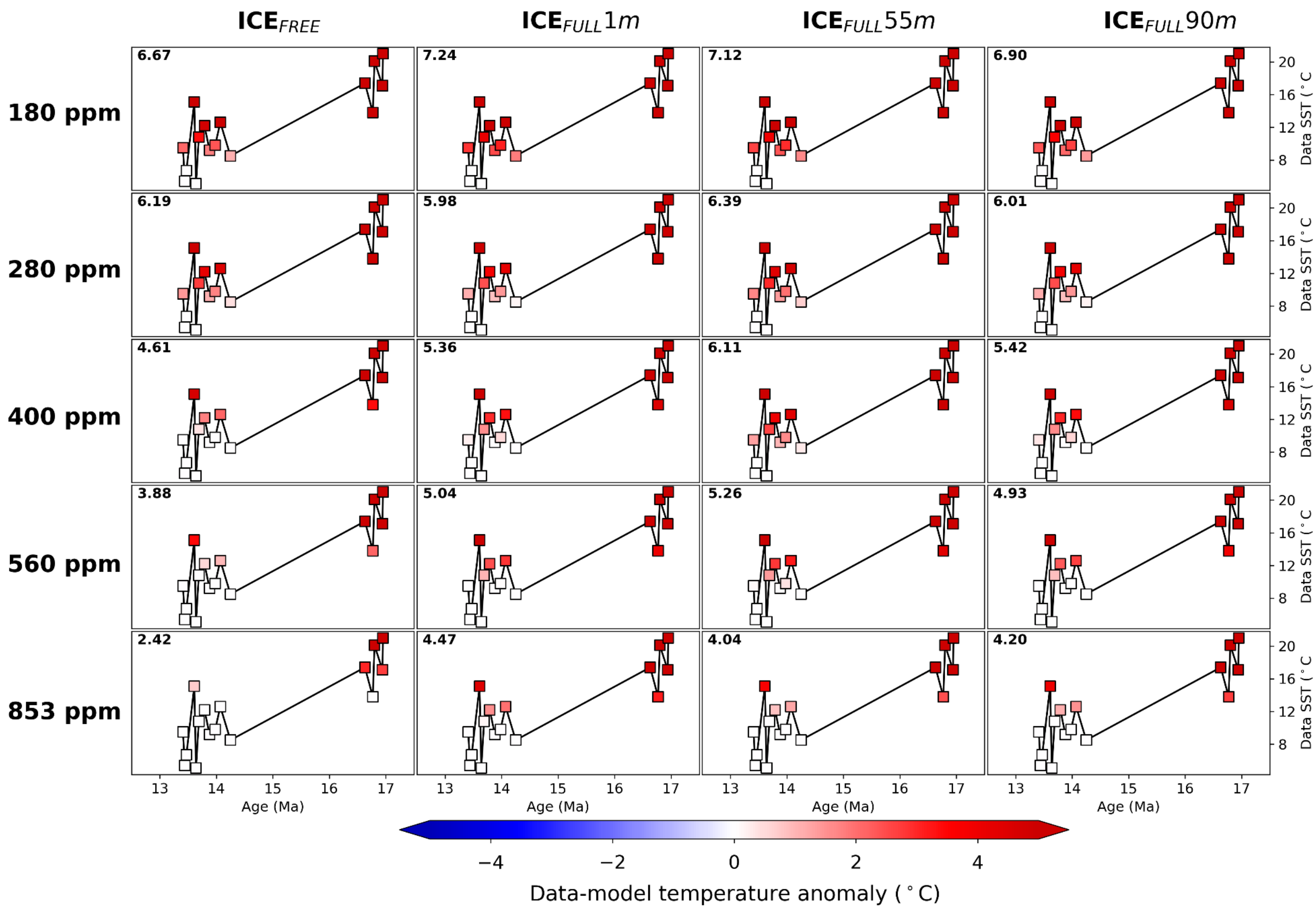

Supplementary Figure S34. Maximum sea surface temperature model-data comparison for Site U1356 in the Southern Ocean (TEX$^{L}_{86}$). Data from Sangiorgi et al., 2018[13] as given in Supplementary Table S10. Legend information as in Supplementary Figure S2.

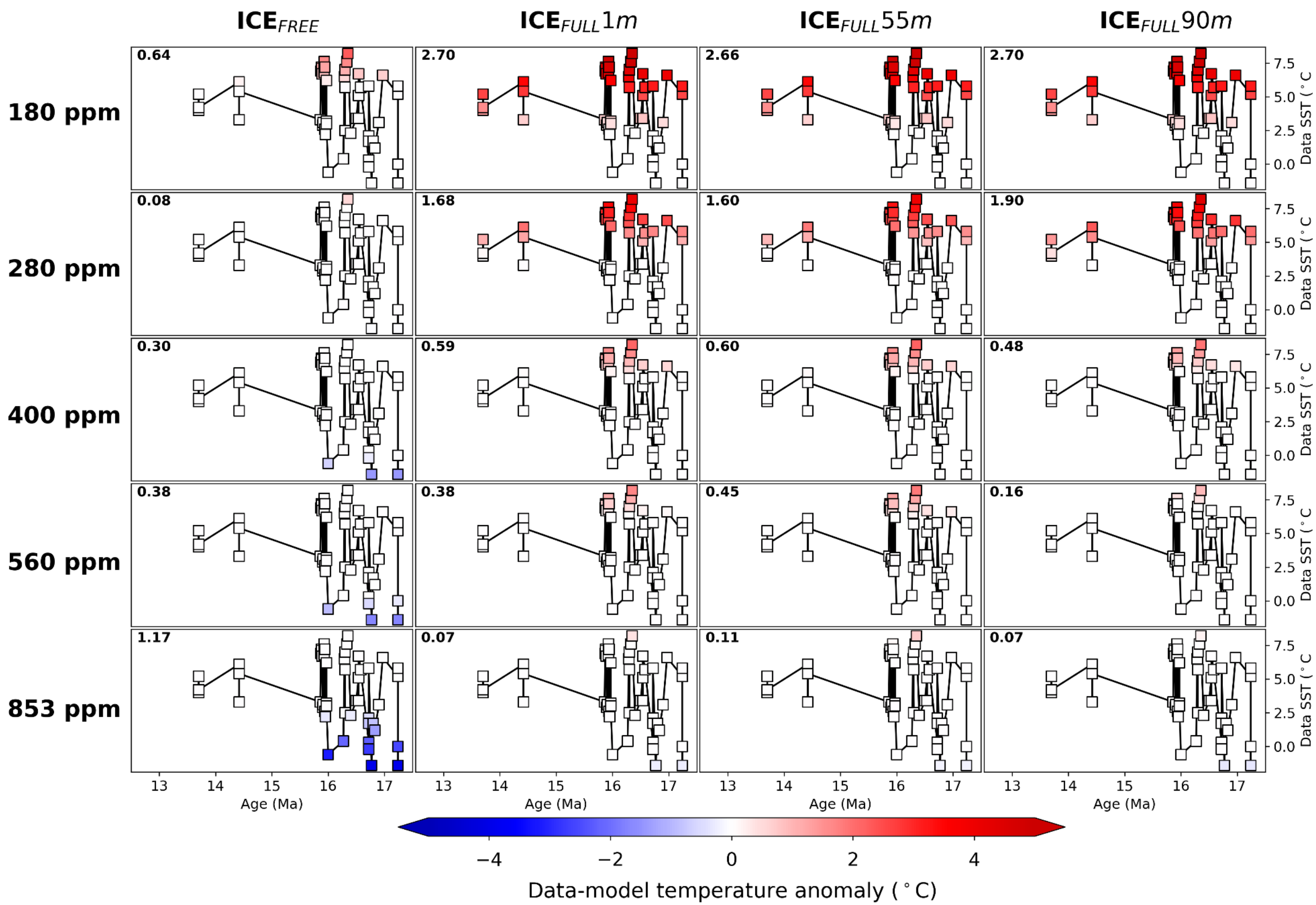

Supplementary Figure S35. Maximum sea surface temperature model-data comparison for Site AND-2A in the Southern Ocean (TEX$^{L}_{86}$). Data from Levy et al., 2016[21] as given in Supplementary Table S10. Legend information as in Supplementary Figure S2.

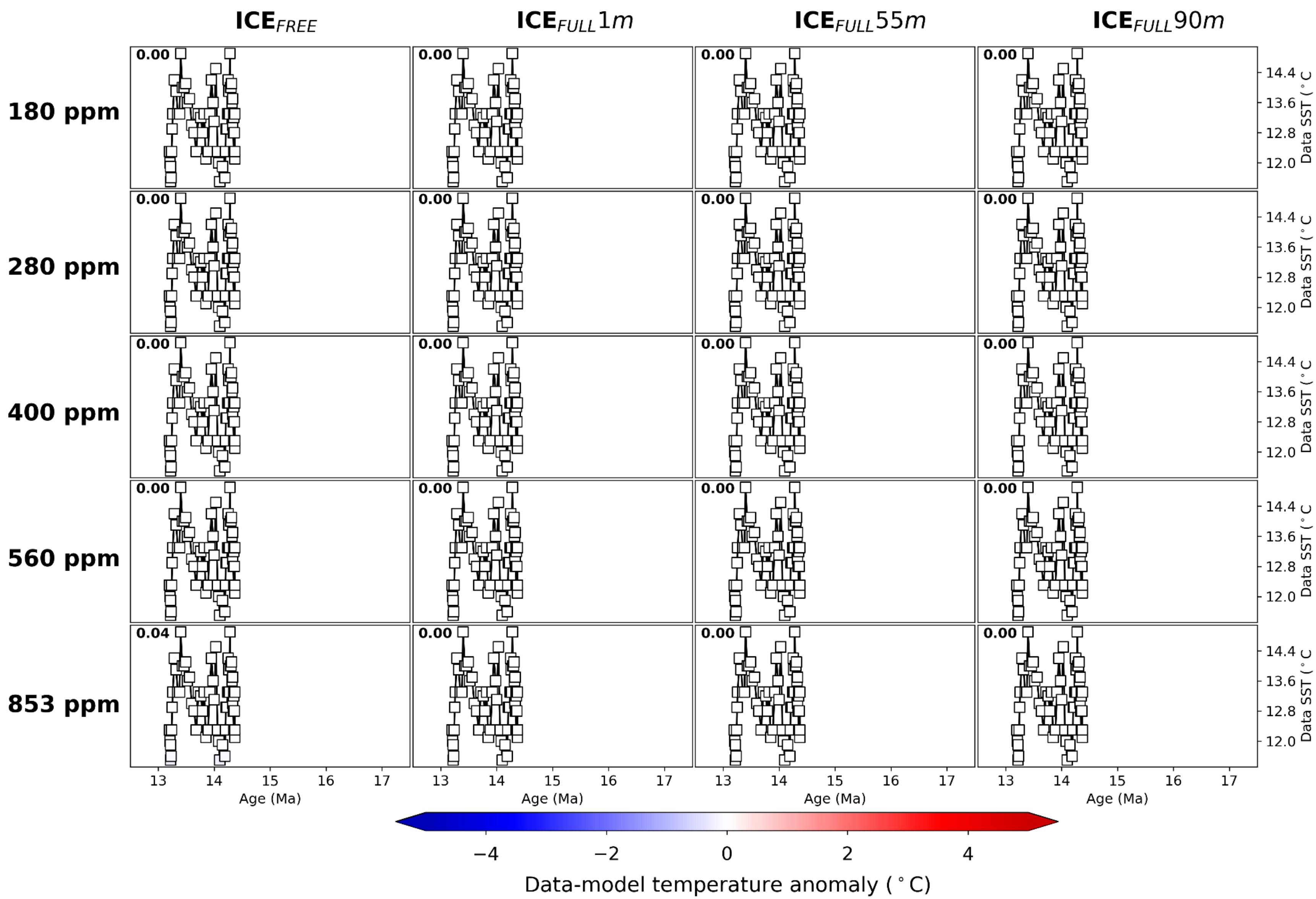

Supplementary Figure S36. Maximum sea surface temperature model-data comparison for Site 1092 in the Southern Ocean (Mg/Ca). Data from Kuhnert et al., 2009[24] as given in Supplementary Table S10. Legend information as in Supplementary Figure S2.

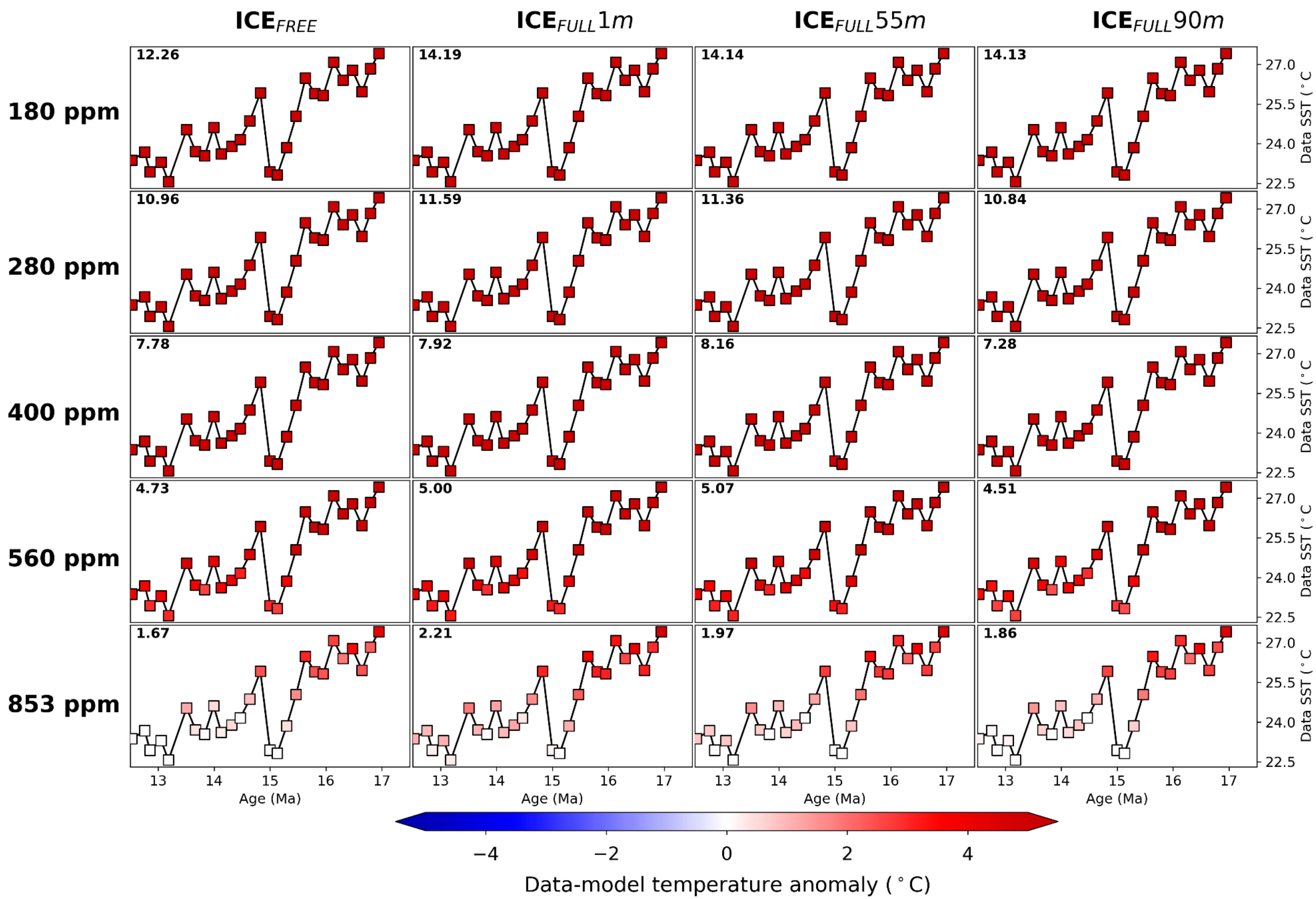

Supplementary Figure S37. Maximum sea surface temperature model-data comparison for Site 982 in the North Atlantic (TEX_{86}). Data from Super et al., 2020[25] as given in Supplementary Table S10. Legend information as in Supplementary Figure S2.

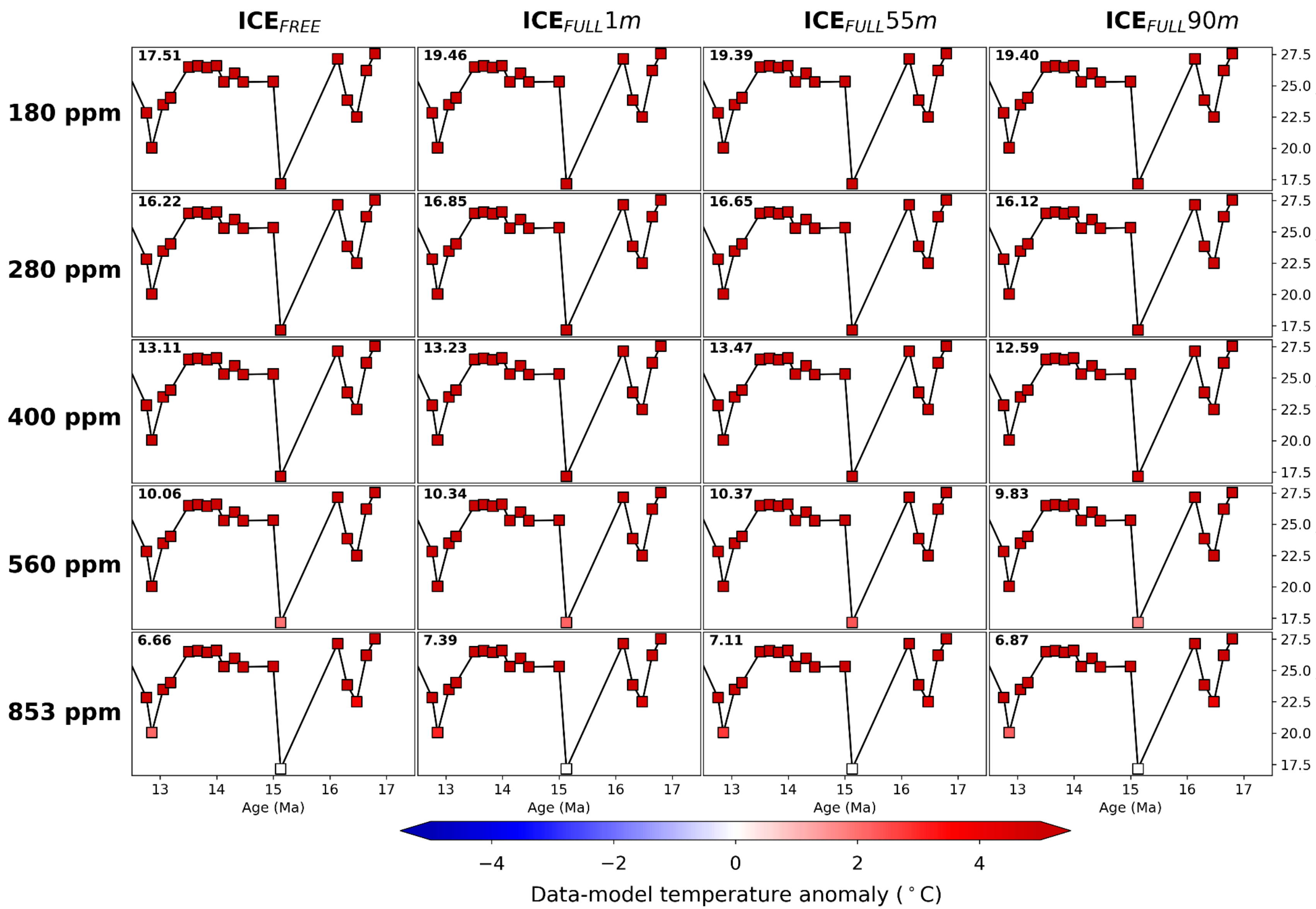

Supplementary Figure S38. Maximum sea surface temperature model-data comparison for Site 982 in the North Atlantic ($U^{K'}_{37}$). Data from Super et al., 2020[25] as given in Supplementary Table S10. Legend information as in Supplementary Figure S2.

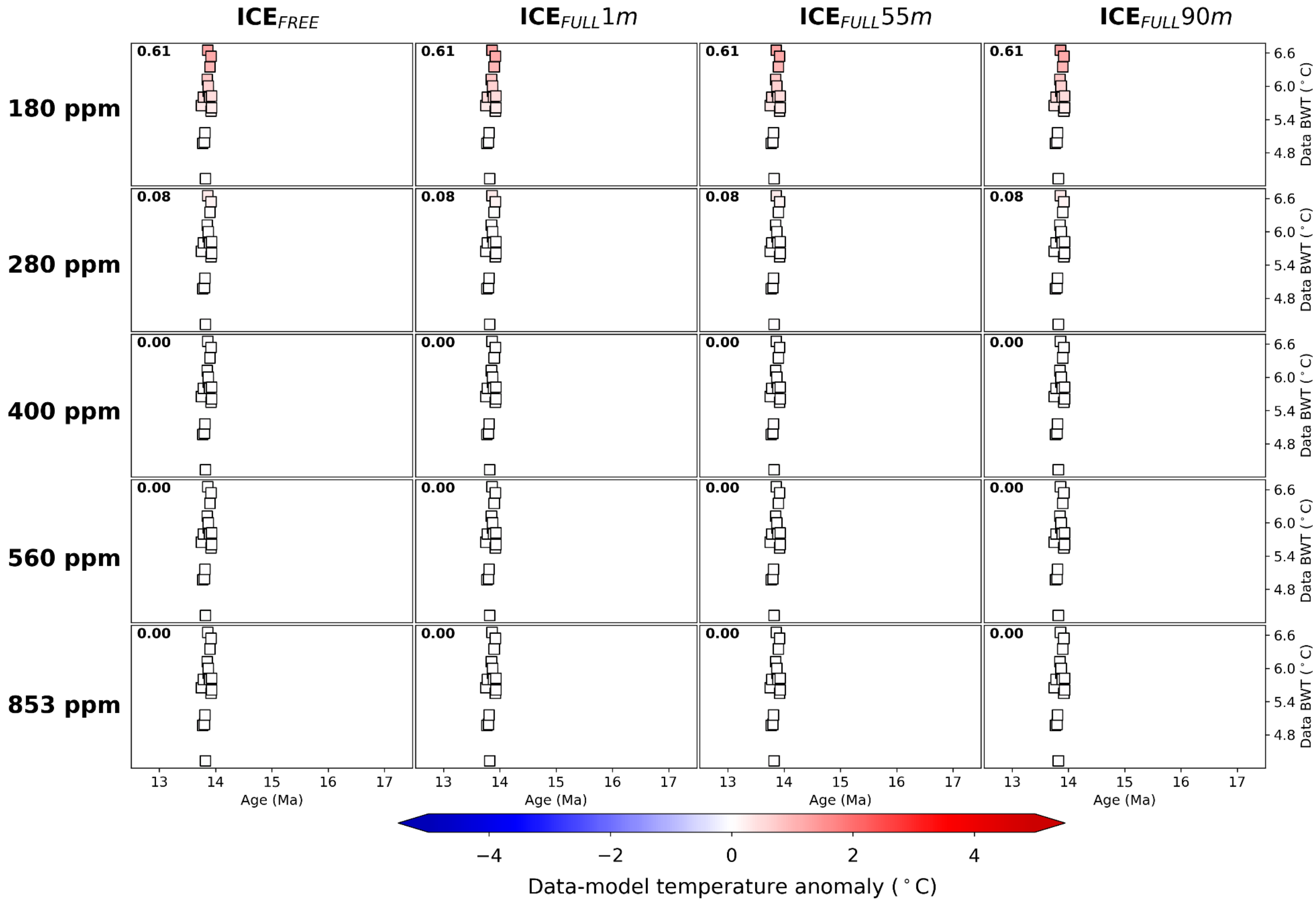

Supplementary Figure S39. Annual mean deep water temperature model-data comparison for Site 1146 in the South China Sea (Mg/Ca). Data from Kochhann et al., 2017[26] as given in Supplementary Table S11. Legend information as in Supplementary Figure S2.

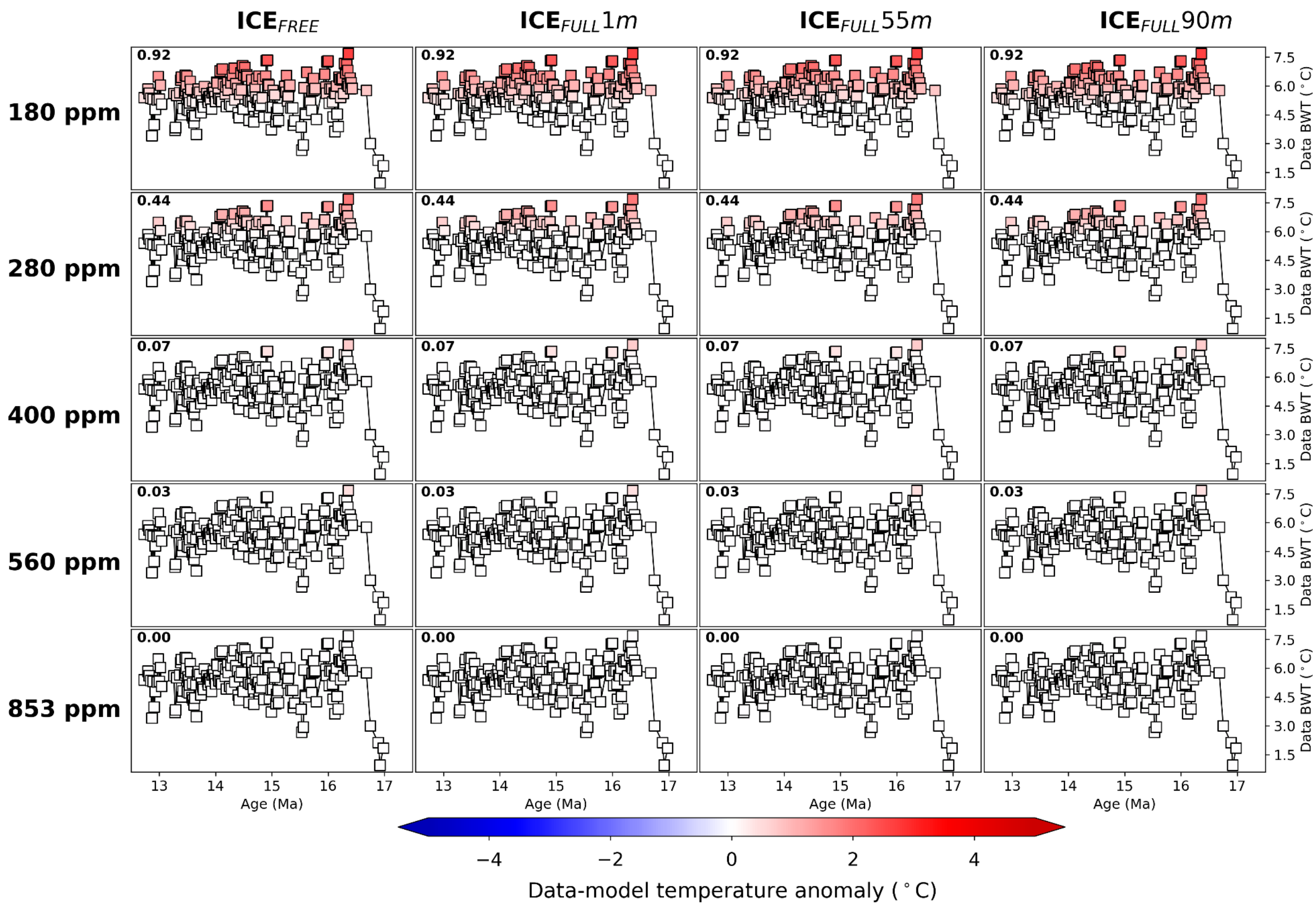

Supplementary Figure S40. Annual mean deep water temperature model-data comparison for Site 1171 in the Southern Ocean (Mg/Ca). Data from Shevenell et al., 2008[5] as given in Supplementary Table S11. Legend information as in Supplementary Figure S2.

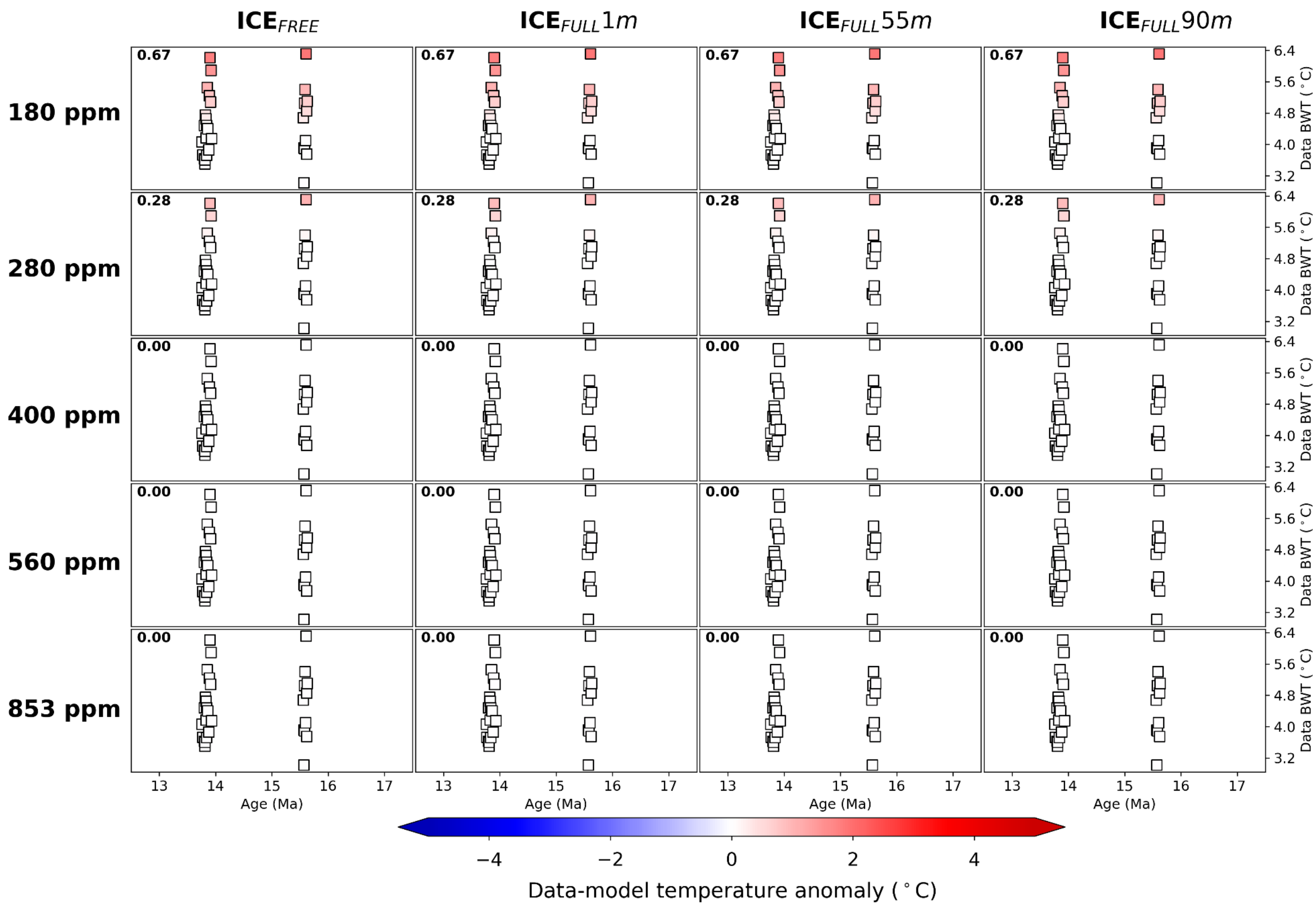

Supplementary Figure S41. Annual mean deep water temperature model-data comparison for Site U1338 in the Tropical Pacific (Mg/Ca). Data from Kochhann et al., 2017[26] as given in Supplementary Table S11. Legend information as in Supplementary Figure S2.

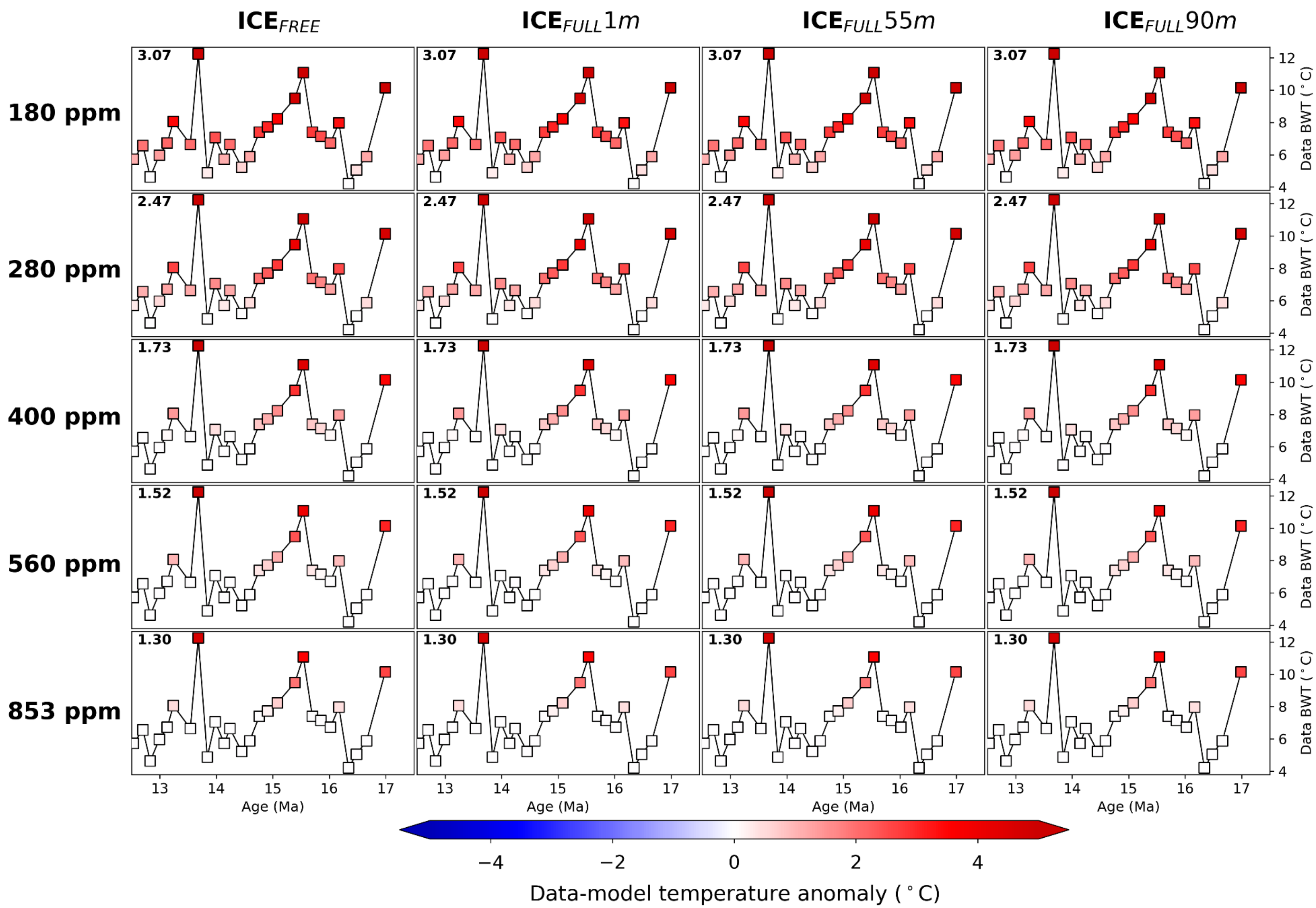

Supplementary Figure S42. Annual mean deep water temperature model-data comparison for Site 806 in the Tropical Pacific (Mg/Ca). Linear-fit data from Lear et al., 2015[9] as given in Supplementary Table S11. Legend information as in Supplementary Figure S2.

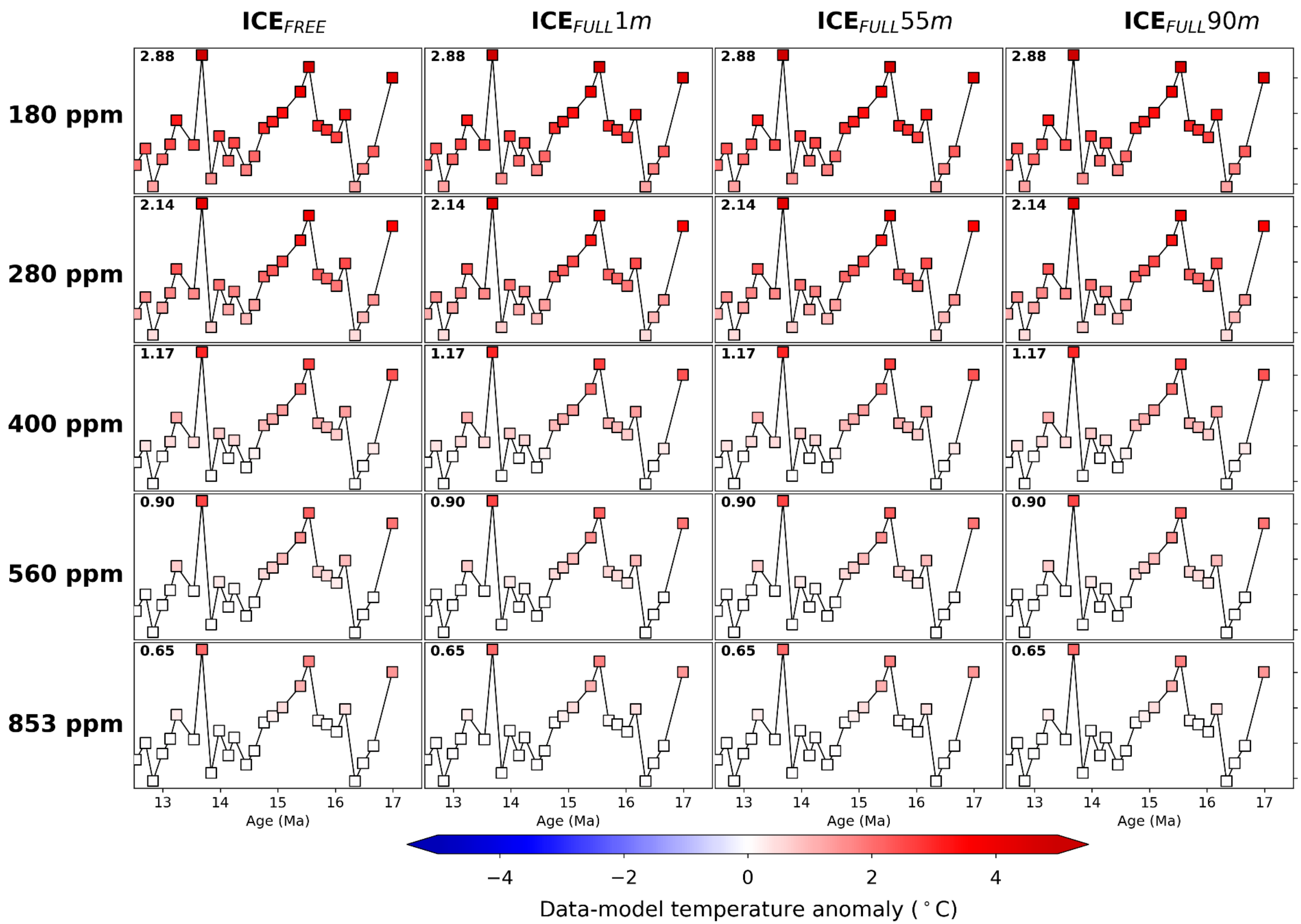

Supplementary Figure S43. Annual mean deep water temperature model-data comparison for Site 806 in the Tropical Pacific (Mg/Ca). Exponential-fit data from Lear et al., 2015[9] as given in Supplementary Table S11. Legend information as in Supplementary Figure S2.

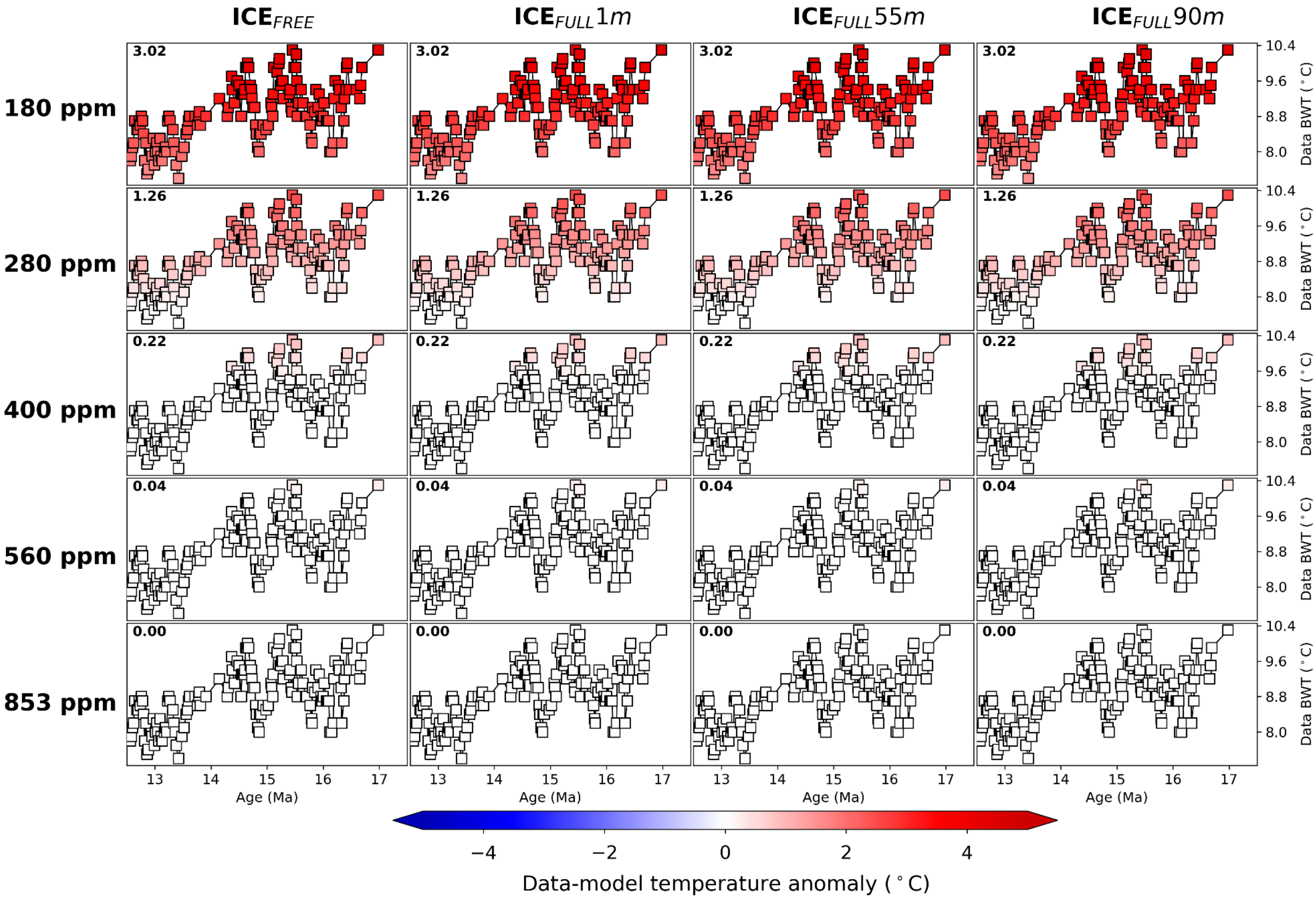

Supplementary Figure S44. Annual mean deep water temperature model-data comparison for Site 761 in the Indian Ocean (Mg/Ca). Unadjusted-data from Lear et al., 2010[8] as given in Supplementary Table S11. Legend information as in Supplementary Figure S2.

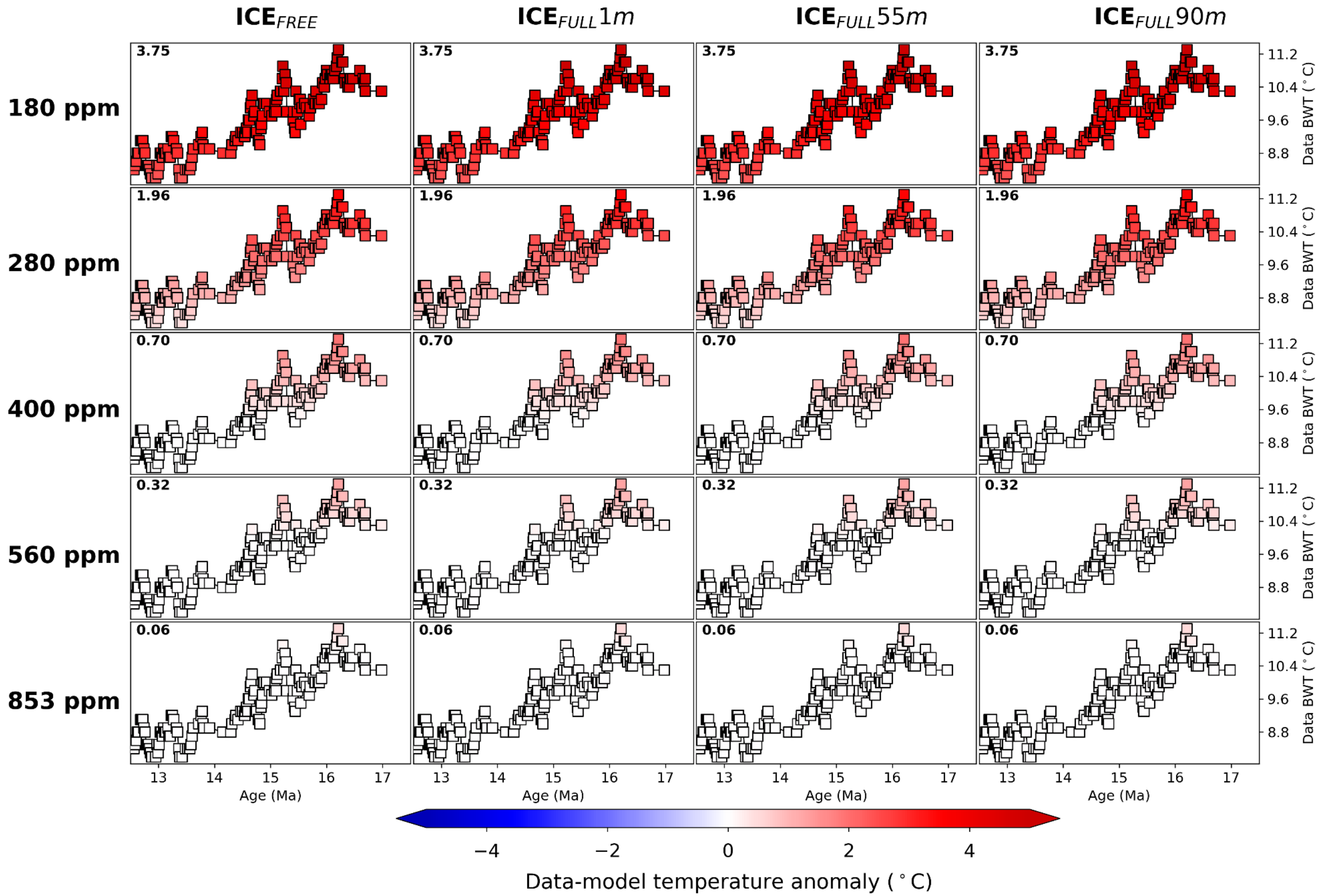

Supplementary Figure S45. Annual mean deep water temperature model-data comparison for Site 761 in the Indian Ocean (Mg/Ca). Adjusted -data from Lear et al., 2010[8] as given in Supplementary Table S11. Legend information as in Supplementary Figure S2.

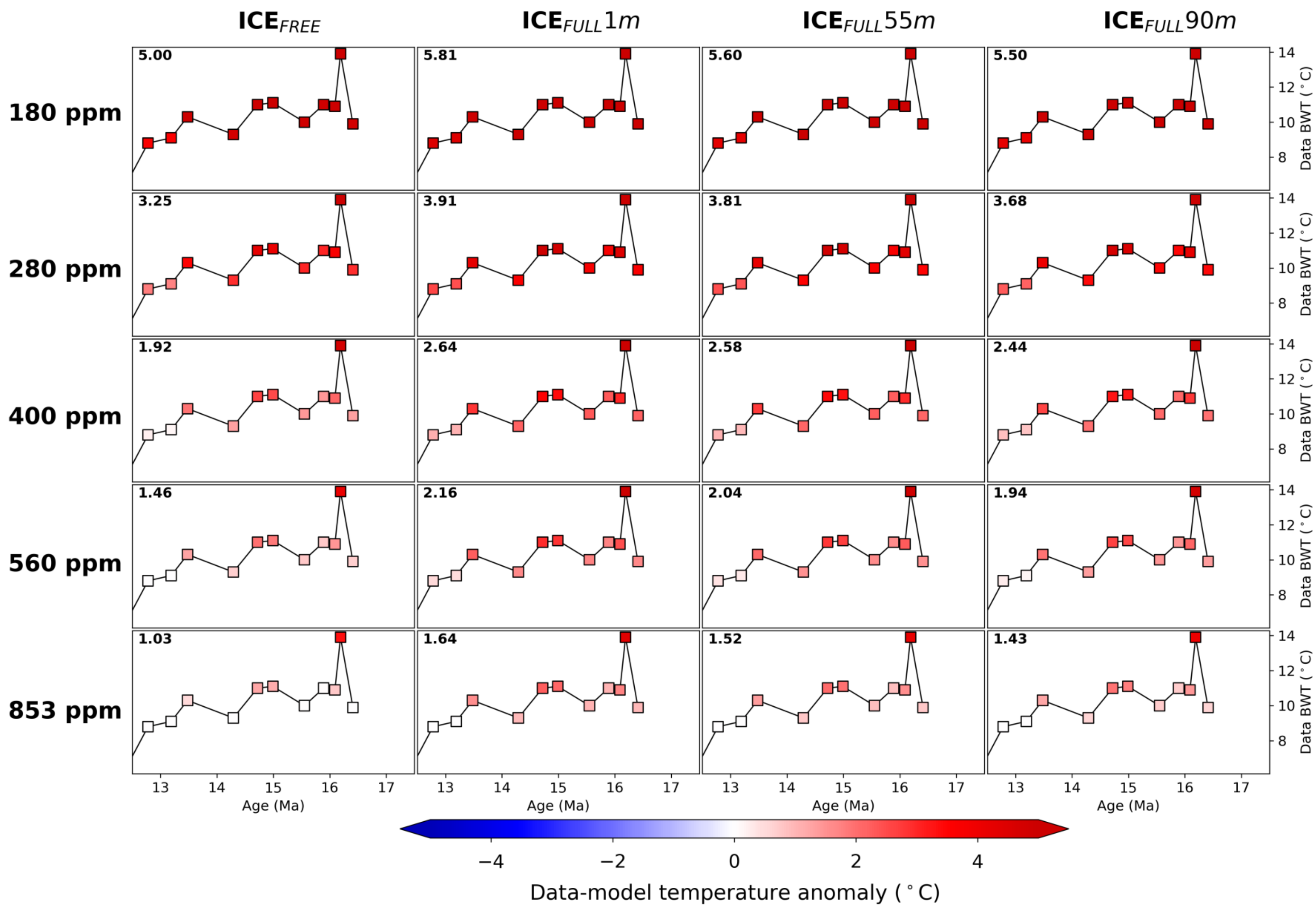

Supplementary Figure S46. Annual mean deep water temperature model-data comparison for Site 761 in the Indian Ocean (Δ47). Data from Modestou et al., 2020[37] as given in Supplementary Table S11. Legend information as in Supplementary Figure S2.

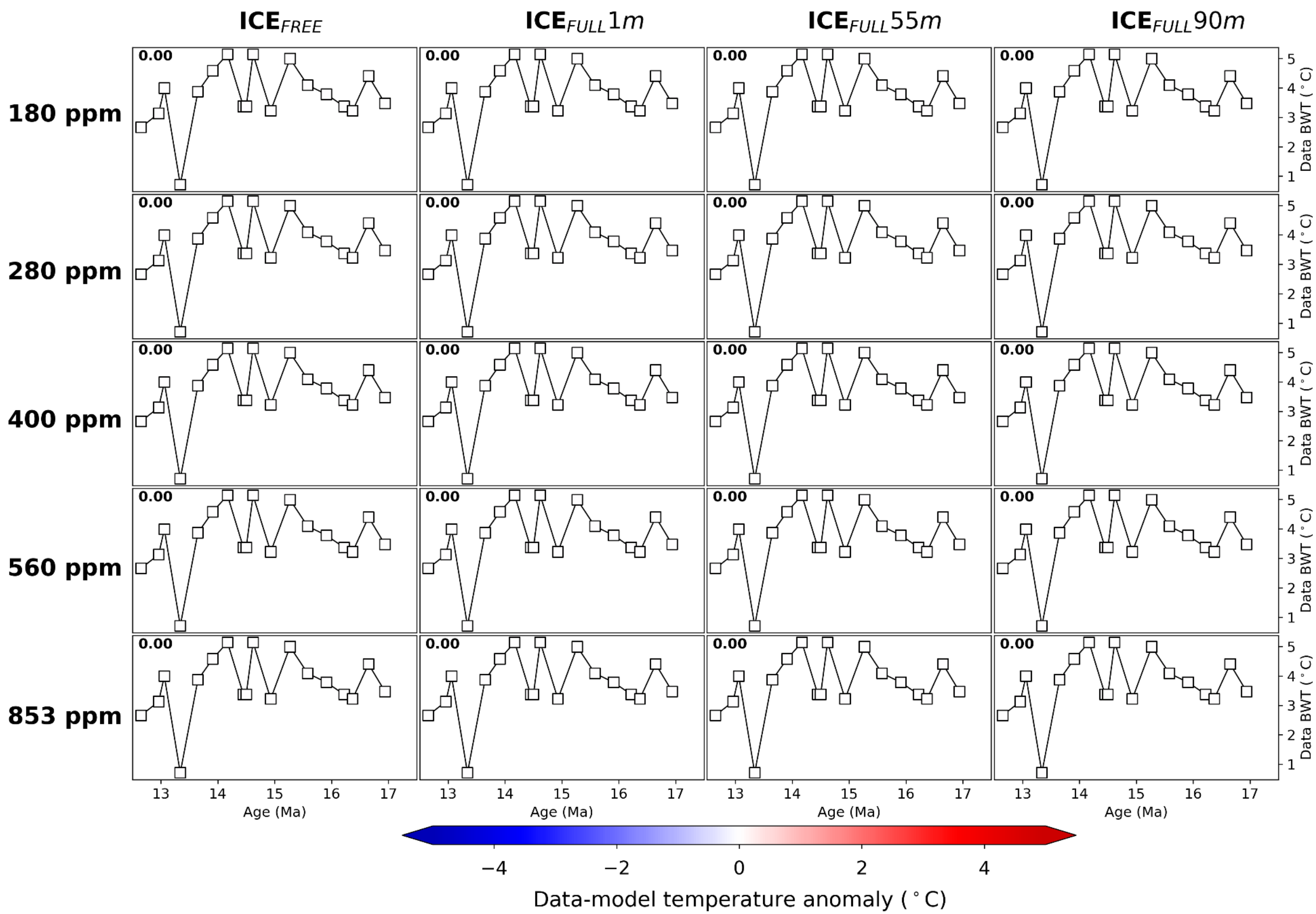

Supplementary Figure S47. Annual mean deep water temperature model-data comparison for Site 747 in the Southern Ocean (Mg/Ca). Data from Billups and Schrag, 2002[27] as given in Supplementary Table S11. Legend information as in Supplementary Figure S2.

S2. Supplementary Discussion

A. Ocean response to glaciation

Although the broad features of our mechanism appear insensitive to the CO_2 concentration (Supplementary Figure S48), we do find evidence that the Southern Ocean sea surface temperature response to glaciation is very sensitive to the underlying CO_2 concentration, and that the relationship is non-linear (Supplementary Figures S49 to S51). In our model, glaciation-driven topographic forcing (ICE_{FULL}1m to ICE_{FULL}55m) results generally in sea surface warming at the global scale, as also found with a similar scenario using the ECHAM5-MPIOM model[28], but we also find divergent trends as the CO_2 concentration either increases or decreases away from our mid-range concentration of 400 ppm (Supplementary Figure S49). This is because of the non-linearities of the winds and sea ice response to CO_2 forcing (Supplementary Figures S52 to S57). We find these non-linearities arise in both summer and winter when we consider just the albedo/surface roughness change (ICE_{FREE} to ICE_{FULL}1m; Supplementary Figures S54 and S56) but only during the summer for winds and winter for sea ice when we consider just the topographic change (ICE_{FULL}1m to ICE_{FULL}55m; Supplementary Figures S51 and S55). When both aspects are combined (ICE_{FREE} to ICE_{FULL}55m), the sea surface temperature responses to glaciation at different CO_2 concentrations become quite complex (Supplemetary Figure S51).

The result of these different surface responses to glaciation results in some differing responses in the deep ocean too. Firstly, although we see a slight cooling of deep waters close to Antarctica in the Ross Sea sector in reponse to topographic change, the Weddell Sea and most of the deep ocean actually warms slightly (ICE_{FULL}1m to ICE_{FULL}55m; Supplementary Figures S58 and S61a). This is the opposite result to that found for the similar scenario with the ECHAM5-MPIOM model[28]. The topopgraphy-driven DWT changes, although small in magnitude, do show some non-linearities as well. The 400 ppm CO_2 scenario shows the most cooling in the Ross Sea sector and the 853 ppm CO_2 scenario showing a patch in this region ~120°W with the opposite sign of change. Although the albedo/surface roughness change (ICE_{FREE} to ICE_{FULL}1m, Supplementary Figures S59 and S61b) also shows some non-linear behaviour in the magnitude of the DWT response, the direction of the changes is consistent. Because the response to albedo/surface roughness changes dominates the combined DWT response to Antarctic glaciation (topography, albedo and surface roughness together), this pattern looks very similar to the albedo/surface roughness response (Supplementary Figures S60 compared to S59, Supplementary Figure S61c compared to S61b). We suggest therefore, that the reason our mechanism operates in the same way between our 280 ppm and 853 ppm longitudinal ice growth scenarios is because the mechanism is largely independent of sea ice concentration.

However, there are now two mechanisms capable of explaining the decoupling of ice volume and DWT at the MMCT glaciation; one involving winds and sea ice[28] and our new mechanism involving precipitation and runoff. The fact these two mechanisms result in the opposite sign of change for DWTs for a similar scenario, and of course the fact that both are likely important and interact, suggests there is a need for a Miocene model intercomparison project to establish to the importance of the different boundary conditions versus the different models used. Scenarios to test alternative regional scale ice sheet configurations at higher CO_2 are recommended, and to consider ice shelf and meltwater processes not included in our model.

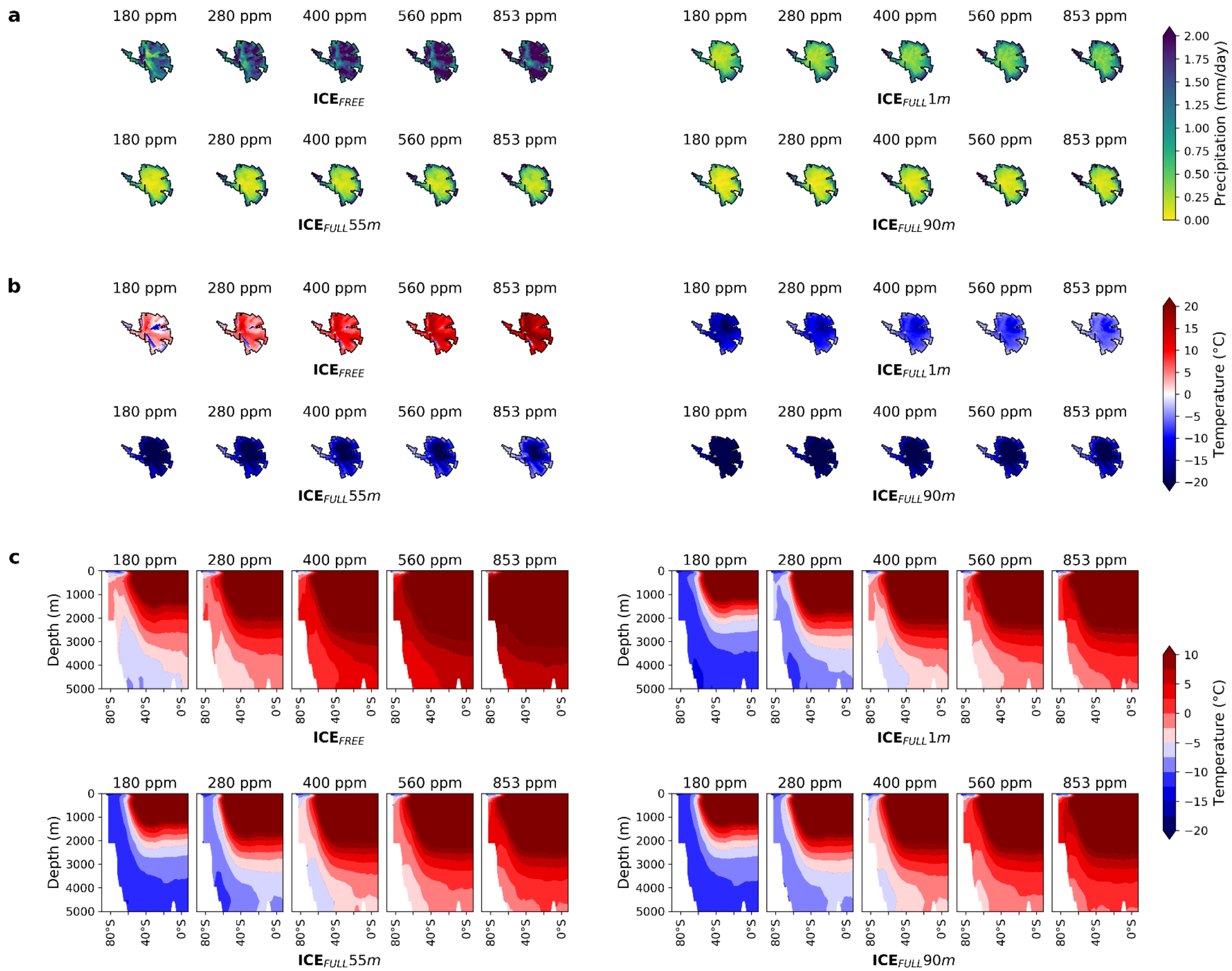

Supplementary Figure S48. Simulated atmospheric and oceanographic conditions in response to changes in CO_2 for different Antarctic ice sheet configurations. (a) Antarctic summer (DJF) precipitation, **(b)**, Antarctic summer air temperature, **(c)**, Annual mean Southern Hemisphere meridional mean ocean temperature. Refer to Fig. 2 for more details of the boundary conditions used.

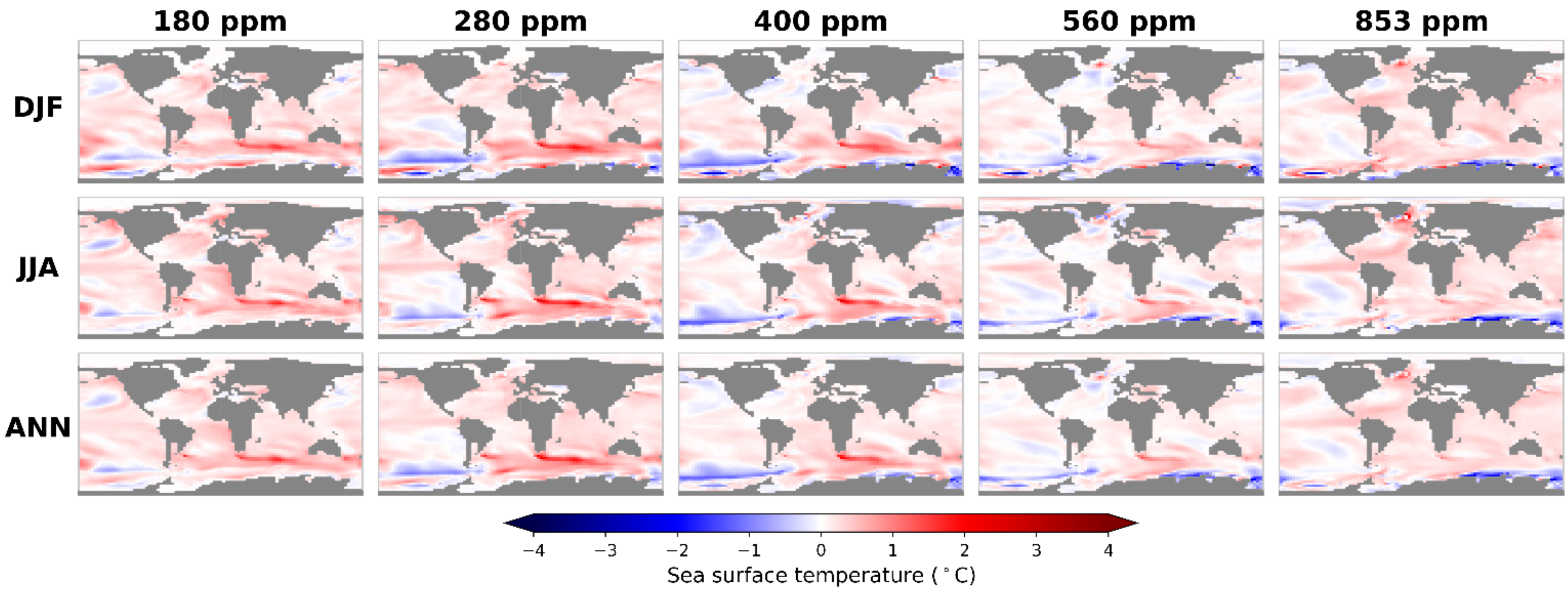

Supplementary Figure S49. Simulated sea surface temperatures in response to glaciation (topography changes only) for different CO_2 concentrations (ICE$_{FULL}$55m – ICE$_{FULL}$1m). Refer to Fig. 2 for more details of the boundary conditions used.

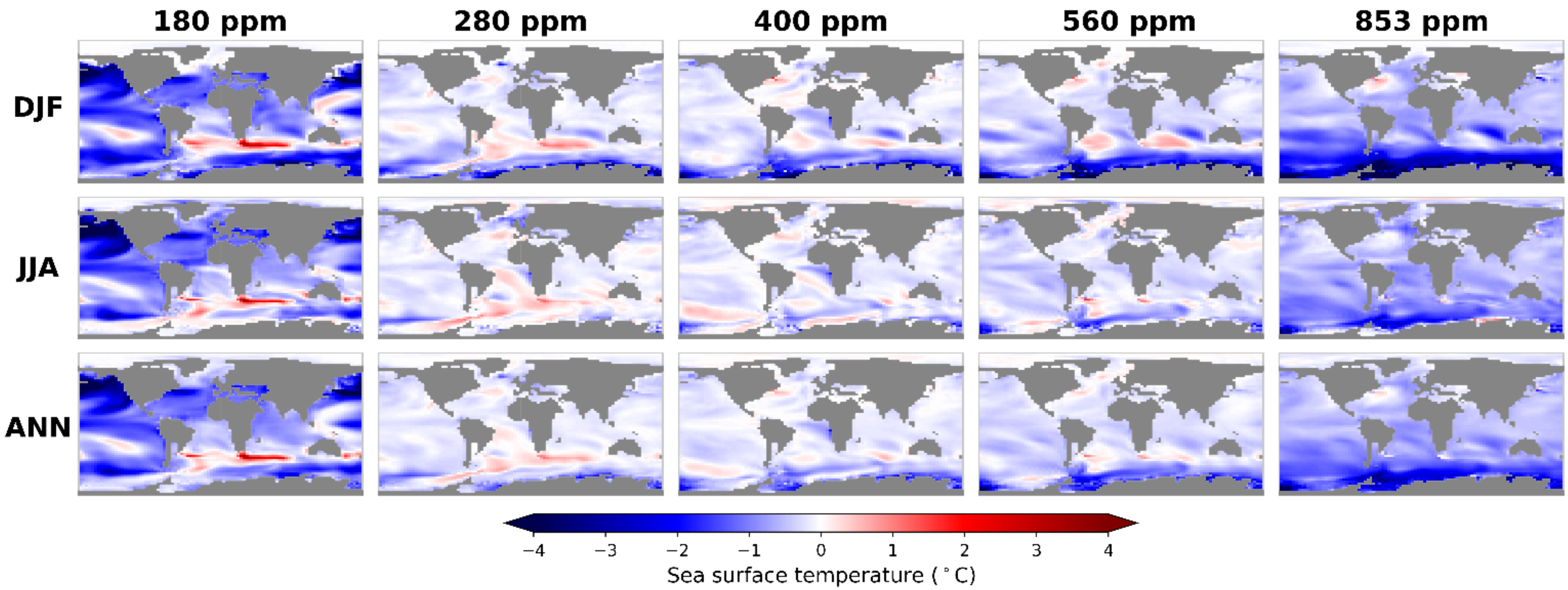

Supplementary Figure S50. Simulated sea surface temperatures in response to glaciation (albedo and surface roughness changes only) for different CO_2 concentrations (ICE$_{FULL}$1m – ICE$_{FREE}$). Refer to Fig. 2 for more details of the boundary conditions used.

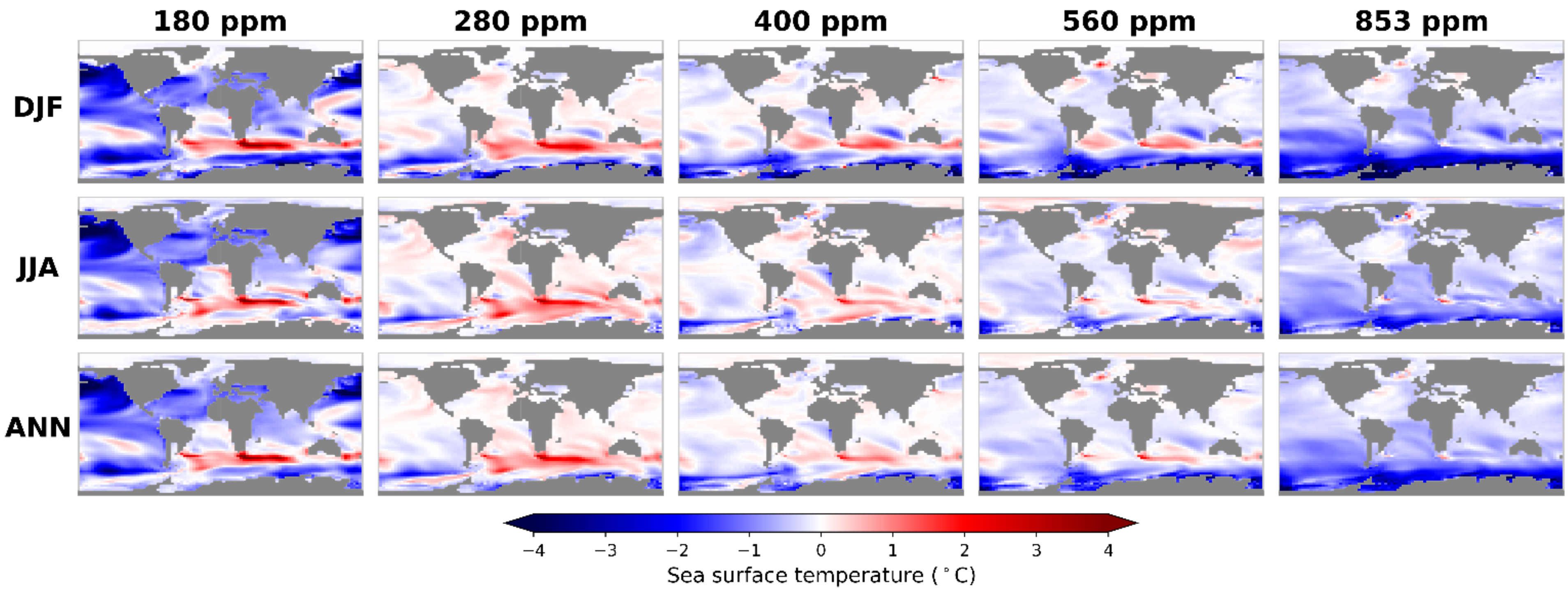

Supplementary Figure S51. Simulated sea surface temperatures in response to glaciation (albedo, surface roughness and topography changes) for different CO_2 concentrations ($ICE_{FULL}55m – ICE_{FREE}$). Refer to Fig. 2 for more details of the boundary conditions used.

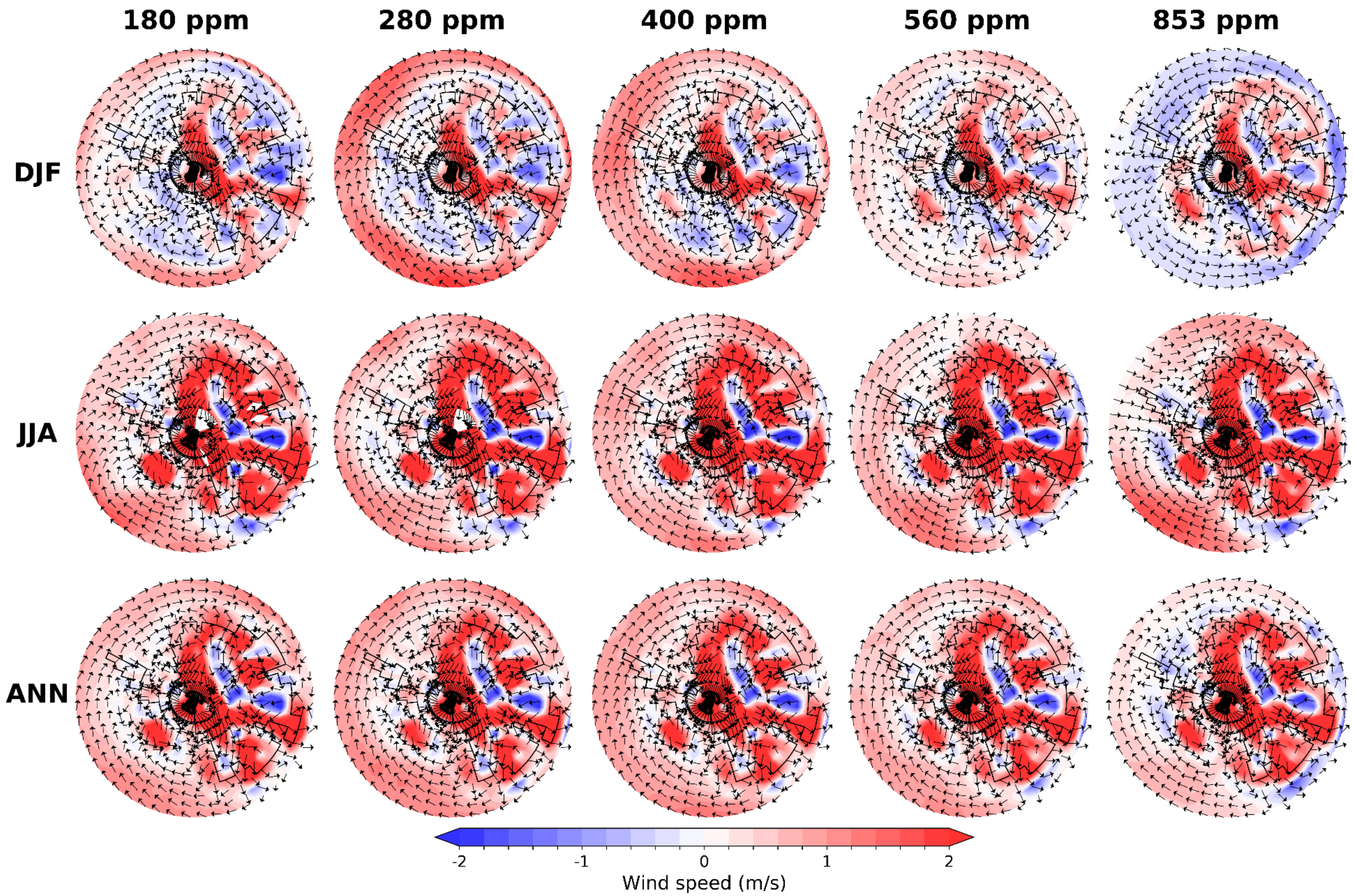

Supplementary Figure S52. Simulated 10m wind response to glaciation (topography changes only) for different CO_2 concentrations (ICE_{FULL}55m – ICE_{FULL}1m). Refer to Fig. 2 for more details of the boundary conditions used.

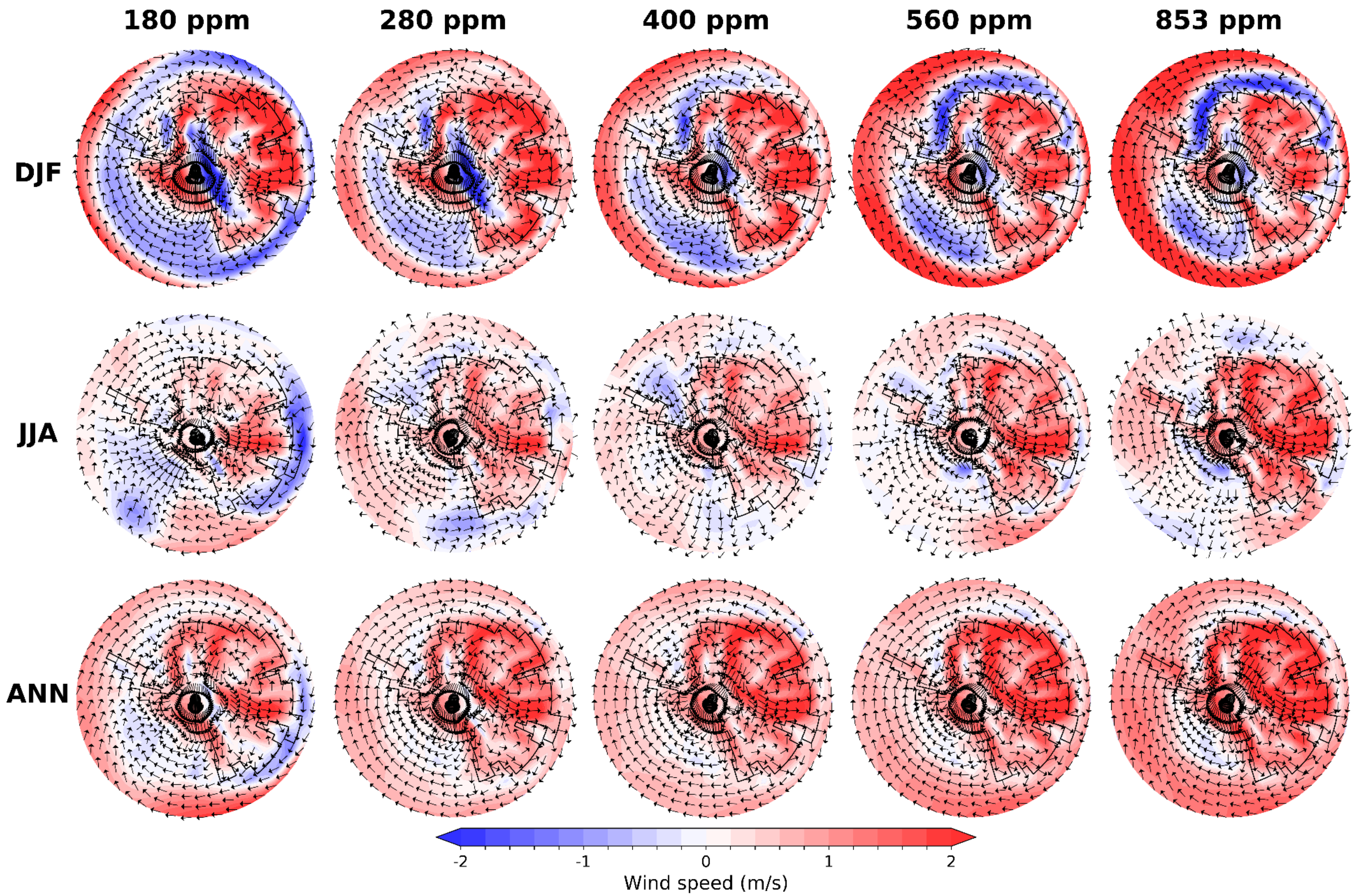

Supplementary Figure S53. Simulated 10m wind response to glaciation (albedo and surface roughness changes only) for different CO_2 concentrations (ICE_{FULL}1m – ICE_{FREE}). Refer to Fig. 2 for more details of the boundary conditions used.

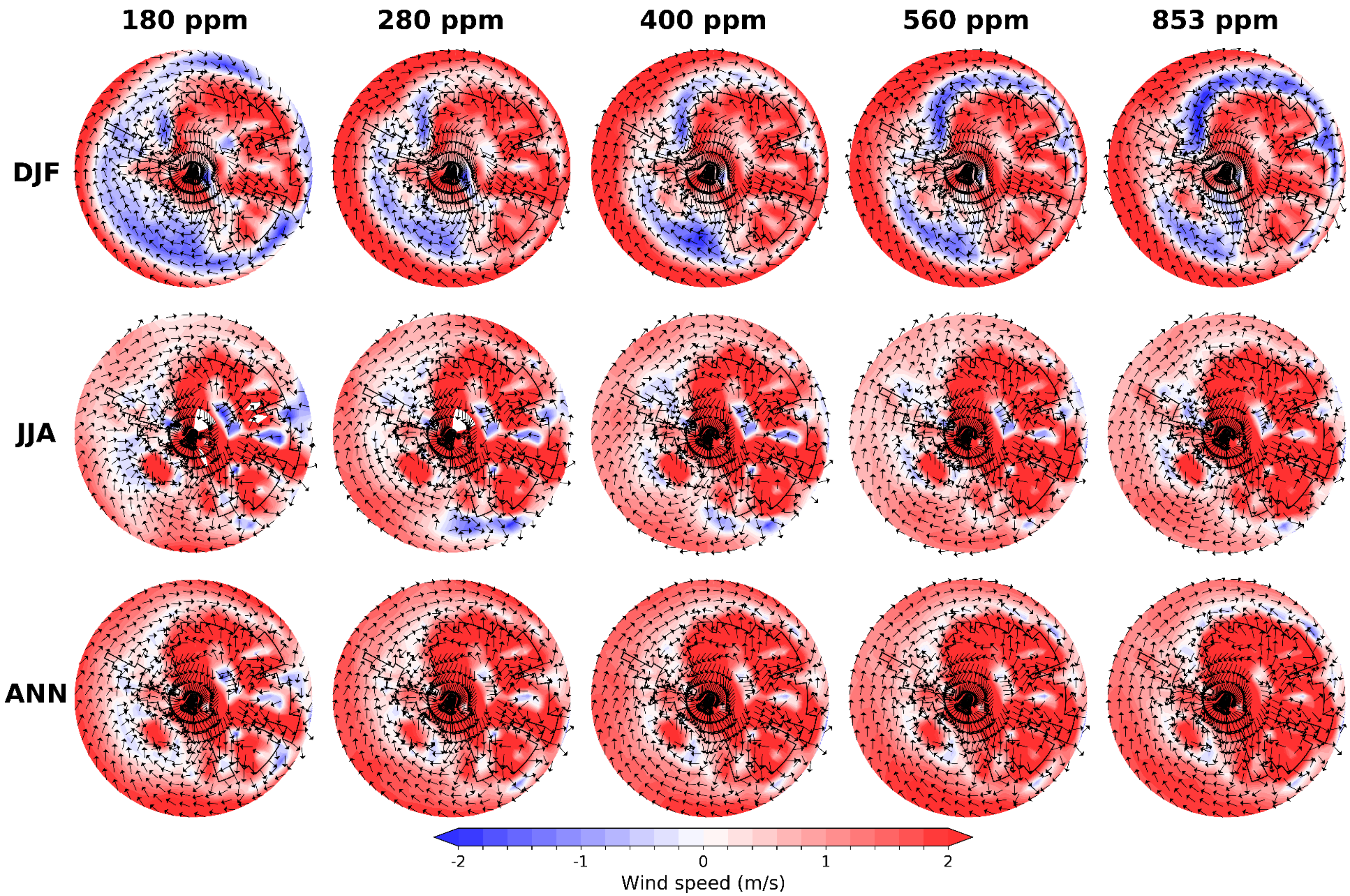

Supplementary Figure S54. Simulated 10m wind response to glaciation (albedo, surface roughness and topography changes) for different CO_2 concentrations ($ICE_{FULL}55m - ICE_{FREE}$). Refer to Fig. 2 for more details of the boundary conditions used.

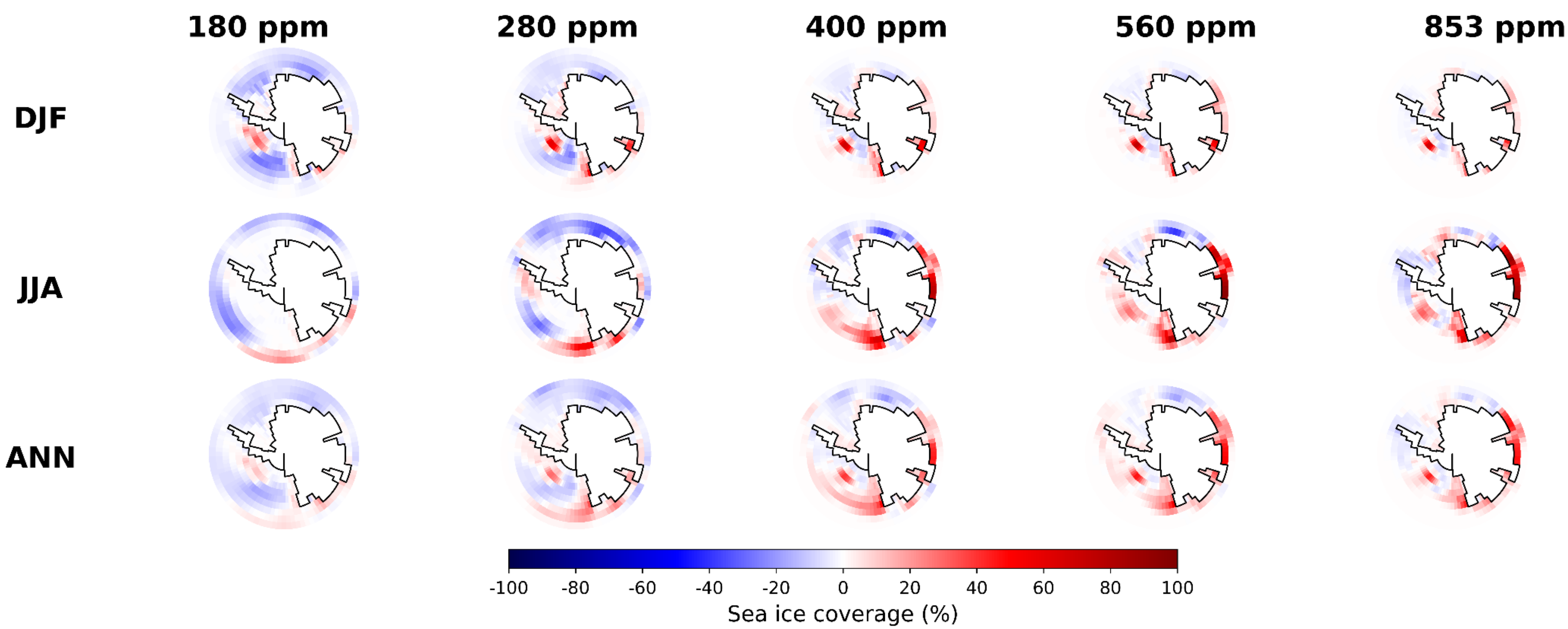

Supplementary Figure S55. Simulated sea ice concentration in response to glaciation (topography changes only) for different CO_2 concentrations ($ICE_{FULL}55m - ICE_{FULL}1m$). Refer to Fig. 2 for more details of the boundary conditions used.

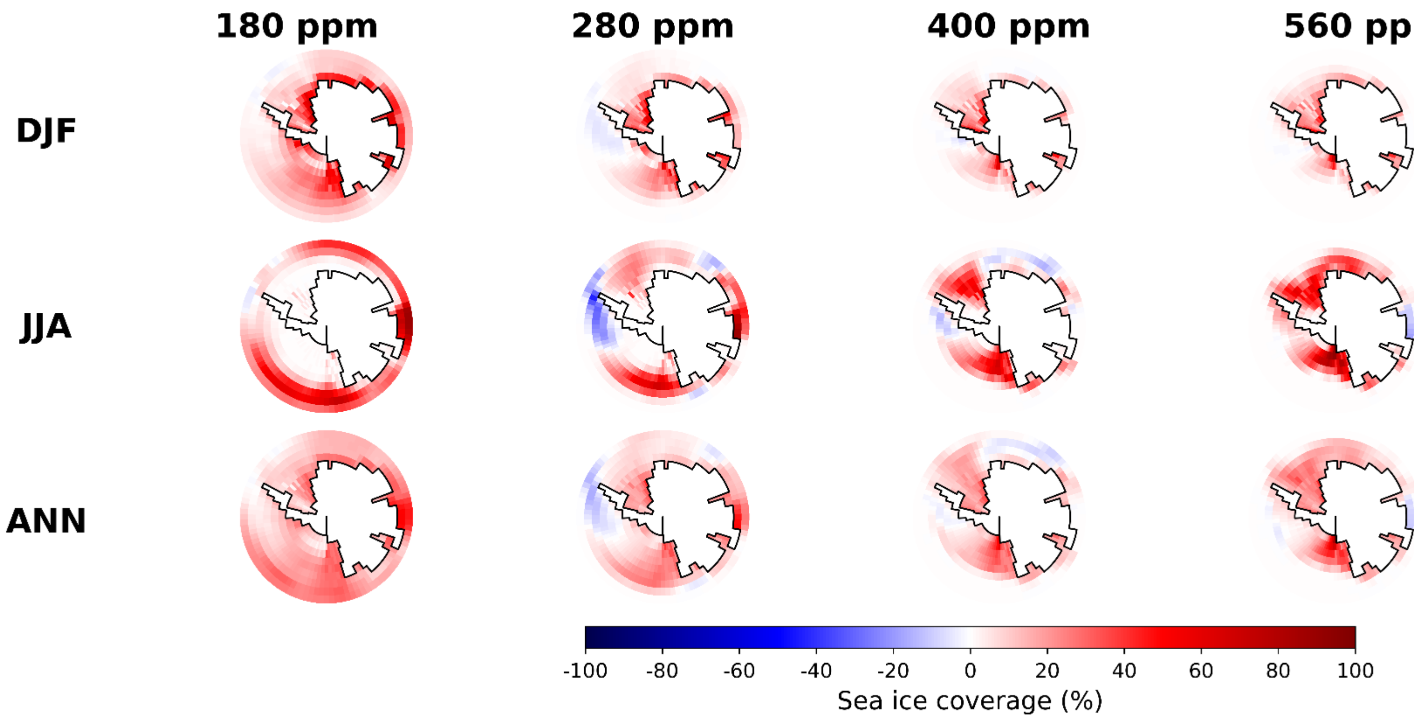

Supplementary Figure S56. Simulated sea ice concentration in response to glaciation (albedo and surface roughness changes only) for different CO_2 concentrations ($ICE_{FULL}1m – ICE_{FREE}$). Refer to Fig. 2 for more details of the boundary conditions used.

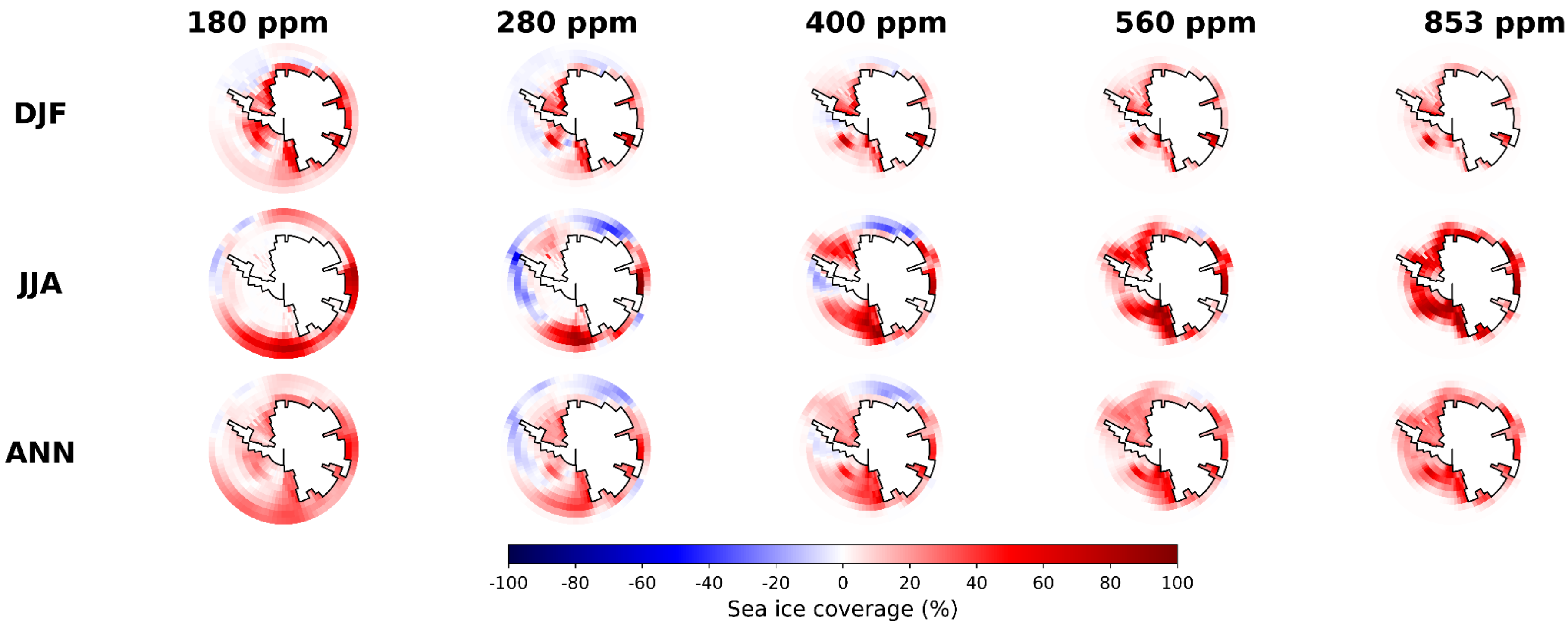

Supplementary Figure S57. Simulated sea ice concentration in response to glaciation (albedo, surface roughtness and topography changes) for different CO_2 concentrations (ICE$_{FULL}$55m –ICE$_{FREE}$). Refer to Fig. 2 for more details of the boundary conditions used.

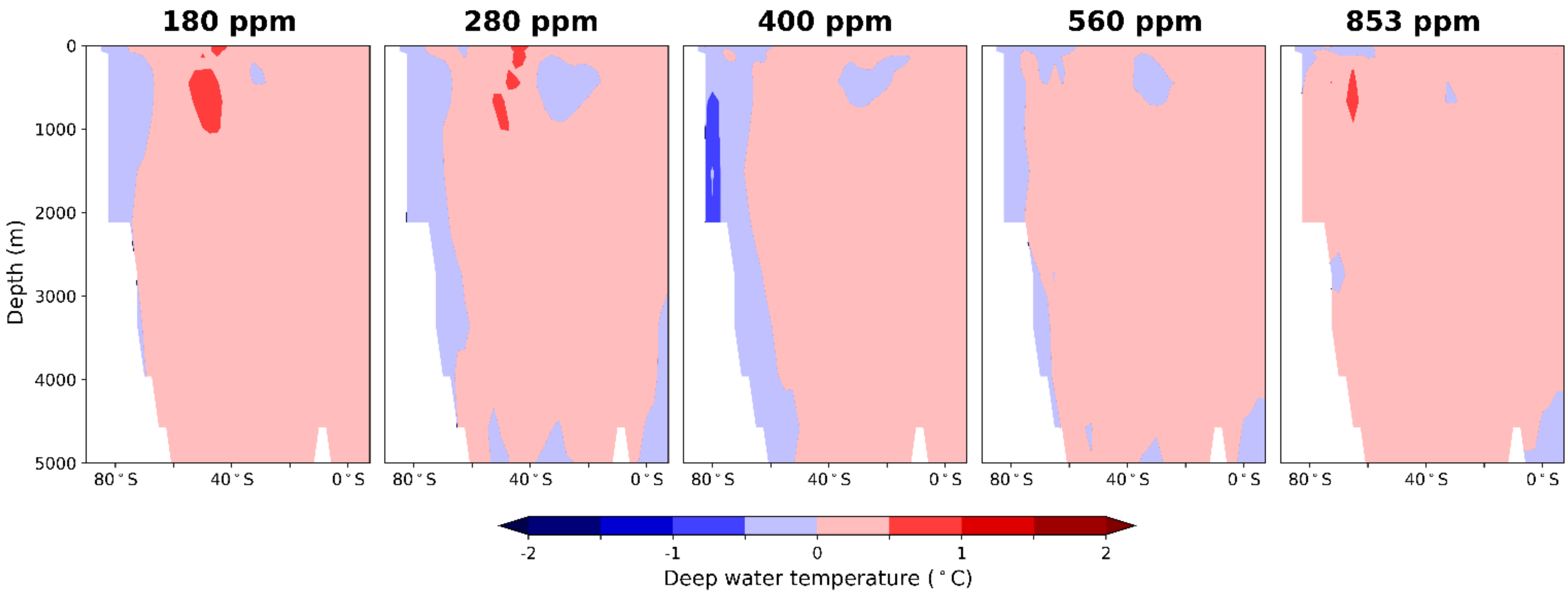

Supplementary Figure S58. Simulated deep water temperatures in response to glaciation (topography changes only) for different CO_2 concentrations (ICE_{FULL}55m – ICE_{FULL}1m). Refer to Fig. 2 for more details of the boundary conditions used.

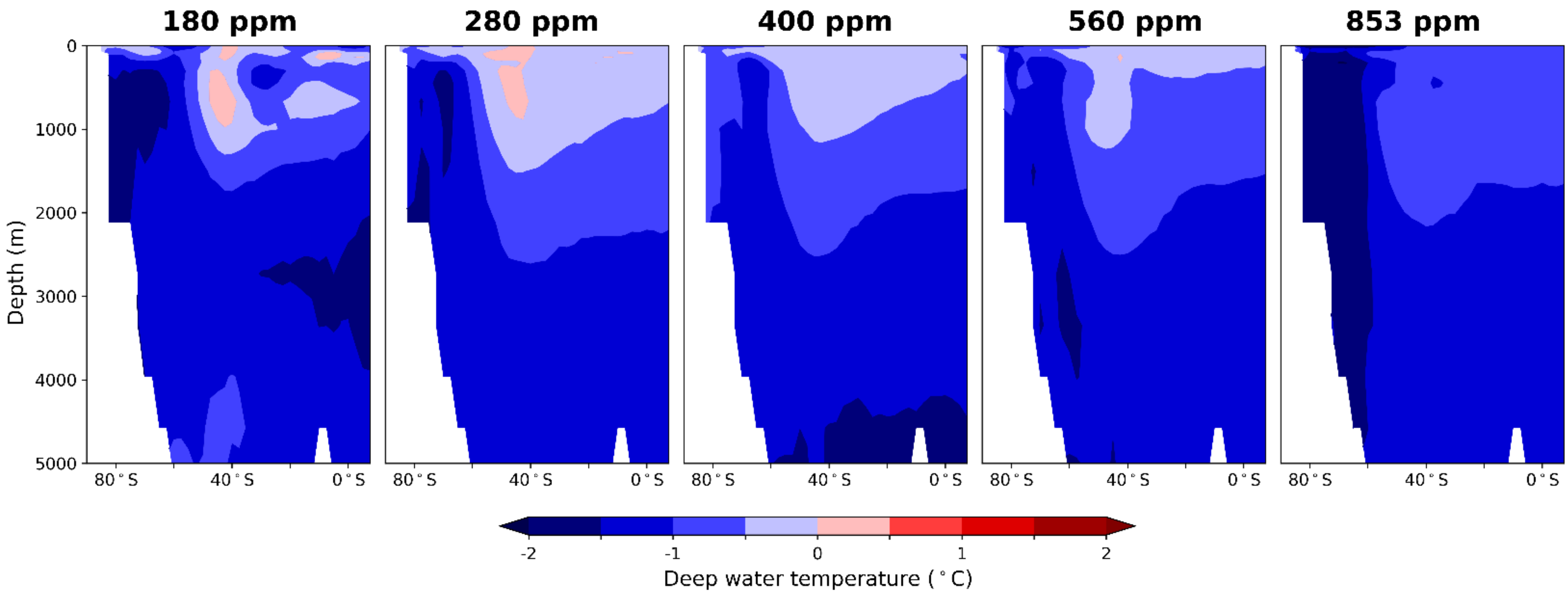

Supplementary Figure S59. Simulated deep water temperatures in response to glaciation (albedo and surface roughness changes only) for different CO_2 concentrations (ICE_{FULL}1m – ICE_{FREE}). Refer to Fig. 2 for more details of the boundary conditions used.

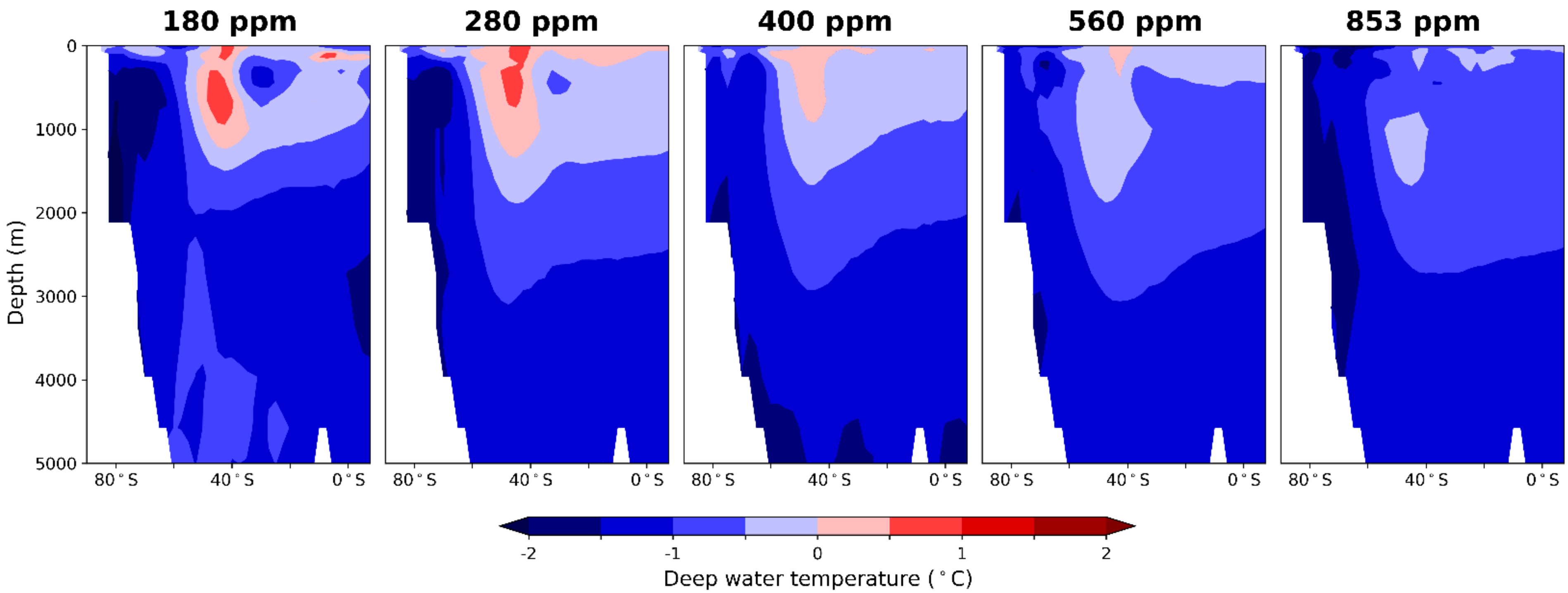

Supplementary Figure S60. Simulated deep water temperature in response to glaciation (albedo, surface roughness and topography changes) for different CO_2 concentrations ($ICE_{FULL}55m – ICE_{FREE}$). Refer to Fig. 2 for more details of the boundary conditions used.

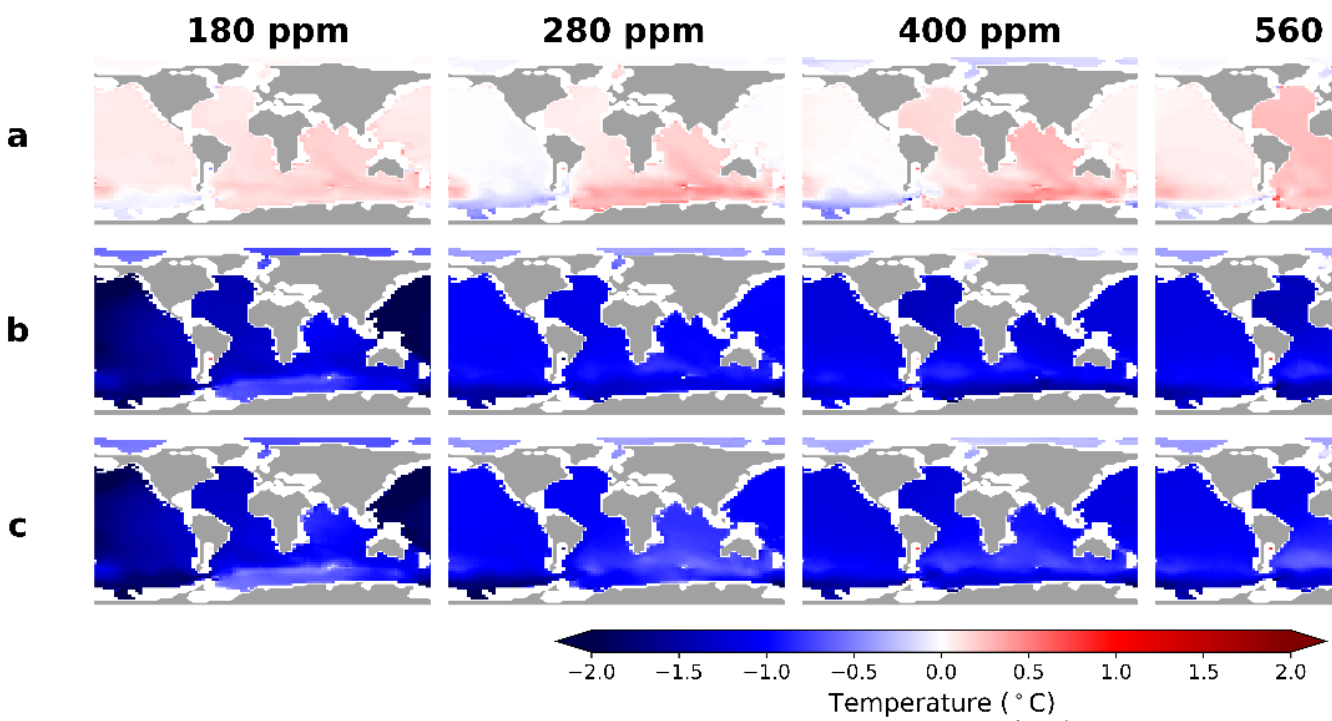

Supplementary Figure S61. Simulated deep water temperatures (2-3km depth) in response to glaciation for different CO_2 concentrations. (a). Topography changes only ($ICE_{FULL}55m - ICE_{FULL}1m$), **(b)**. Albedo/surface roughness changes only ($ICE_{FULL}1m - ICE_{FREE}$) and **(c)**. Albedo, surface roughness and topography changes ($ICE_{FULL}55m - ICE_{FREE}$). Refer to Fig. 2 for more details of the boundary conditions used.

B. Middle Miocene deep water production

In all of our middle Miocene simulations, deep water is in all cases primarily produced in the south; Atlantic Meridional Overturning Circulation in the Northern Hemisphere is weak (i.e. <3Sv, as compared to 18Sv for a pre-industrial simulation using the same model[2]) and there is no deep water production in the North Pacific (except for our ice-free 180 ppm CO_2 scenario, which is perhaps one of the most unrealistic). Modern North Atlantic Deep Water (NADW) is comprised of deep waters formed in both the Nordic seas and the Labrador Sea. Whilst there is evidence for the onset of deep convection in the Nordic Seas by the middle Miocene[29–31], the role of NADW (or its precursor, Northern Component Water, NCW) in the global ocean at this time is an open question. Benthic foraminifera carbon isotope compilations show similar values in all basins during the middle Miocene, interpreted to indicate that deep water formation came from a common southern source[32,33]. However, recent work has shown that the geochemical signature of ancient NCW differed from modern values[31], which implies that this interpretation may not be robust. Opal deposition, however, is a process indicating the presence of older less corrosive deep waters rather than NADW/NCW. Therefore, the fact that opal deposition at Site 642 in the Nordic Seas did not collapse until 14Ma[34] provides support for a minor role for NCW in global ocean circulation during the MCO. Hence, we are confident that our model results are robust for the middle Miocene.

C. Relationship between ice sheet volume and ice sheet area

The relationship between ice volume and ice area for the ice sheet model used in Gasson et al., 2016[35] is approximately linear for ice sheet retreat (Supplementary Figure S62). Ice sheet growth simulations show a similar linear relationship (not shown).

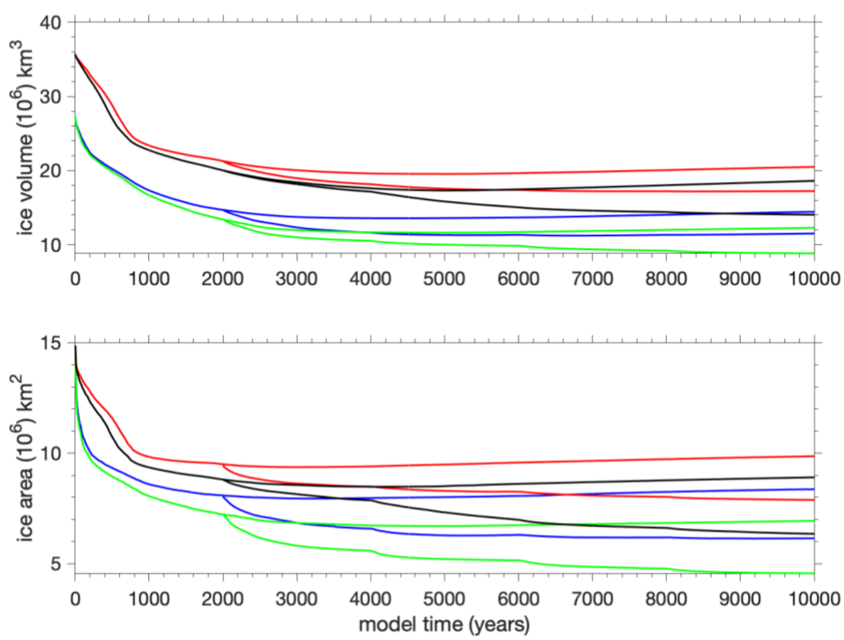

Supplementary Figure S62. Timeseries of ice sheet volume and ice sheet area. Values are taken from the ice model simulations of Gasson et al., 2016[35] and the plot was provided by Edward Gasson. The similations are blue (500ppm, bedmap2), green (840 ppm, bedmap2), red (500 ppm, 'Miocene' topography), black (840 ppm, 'Miocene' topography). The plots show the simulations both with and without asynchronous coupling of the ice sheet to the climate model.

D. Deep water temperature changes that can be accounted for from CO_2 forcing alone

In order to assess the contribution made from CO_2 forcing alone to the overall reported temperature changes at Site 1171 and Site 761 during the MCO and the MMCT glaciation, we perform linear interpolation of the results for the different CO_2 simulations conducted.

Average CO_2 variability during the MCO were of the order 630 - 470 ppm[22]. Supplementary Table S1 documents the DWT changes linearly interpolated for these CO_2 concentrations and suggest that CO_2 forcing accounts for between 0.5 and 0.6°C of temperature change.

	ICE_{FREE}	ICE_{FULL}1m	ICE_{FULL}55m	ICE_{FULL}90m
Site 1171	0.6	0.6	0.5	0.5
Site 761	0.5	0.5	0.5	0.5

Supplementary Table S1. Simulated deep water temperatures (°C) for CO_2 changes estimated during the MCO (630-470 ppm[22]) at Site 1171 in the Southern Ocean and at at Site 761 in the Indian Ocean. Temperatures for the 630 ppm CO_2 scenarios are linearly interpolated between the 853 ppm and the 560 ppm CO_2 equivalent scenarios. Temperatures for the 470 ppm CO_2 scenarios are linearly interpolated between the 560 ppm and the 400 ppm CO_2 equivalent scenarios.

The magnitude of the CO_2 decline during the MMCT glaciation was at most 570-400 ppm[22]. Supplementary Table S2 documents the DWT changes linearly interpolated for these CO_2 concentrations and suggest that CO_2 forcing accounts for between 0.5 and 0.8°C of temperature change. These results therefore suggest a more important role for CO_2 changes in determining the DWT during the MMCT glaciation than the MCO (Supplementary Table S2 compared to S1), consistent with the results of a new study, which concluded that CO_2 has a direct role in driving the MMCT ice growth event[20].

	ICE_{FREE}	ICE_{FULL}1m	ICE_{FULL}55m	ICE_{FULL}90m
Site 1171	0.6	0.8	0.6	0.5
Site 761	0.6	0.6	0.6	0.5

Supplementary Table S2. Simulated deep water temperatures (°C) for CO_2 changes estimated during the MMCT glaciation (570-400 ppm[22]) at Site 1171 in the Southern Ocean and at at Site 761 in the Indian Ocean. Temperatures for the 570 ppm CO_2 scenarios are linearly interpolated between the 853 ppm and the 560 ppm CO_2 equivalent scenarios.

E. Deep water temperature changes that can be accounted for from surface albedo and roughness forcing alone

In order to assess the contribution made to the overall reported temperature changes at Site 1171 and Site 761 from our mechanism during the MCO, we compare the deep water temperature changes between our ICE_{FREE} and our ICE_{FULL}1m scenarios for the different CO_2 concentrations simulated. Supplementary Table S3 shows that these surface albedo and roughness changes account for between 0.9 and 1.9°C of temperature change.

	CO_2 concentration				
	180 ppm	280 ppm	400 ppm	560 ppm	853 ppm
Site 1171	1.5	1.0	1.2	1.1	1.4
Site 761	1.9	0.9	1.1	1.2	1.1

Supplementary Table S3. Simulated deep water temperature changes (°C) due to surface albedo and roughness changes estimated during the MCO (anomaly between ICE_{FULL}1m and ICE_{FREE}).

In order to assess the contribution made to the overall reported temperature changes at Site 1171 and Site 761 from our mechanism during the MMCT glaciation, we compare the deep water temperature changes between our ICE_{FULL}1m and our ICE_{FULL}55m scenarios for the different CO_2 concentrations simulated. Supplementary Table S4 shows that these topographic changes result in temperature changes spanning no change at all, up to 0.5°C of warming.

	CO_2 concentration				
	180 ppm	280 ppm	400 ppm	560 ppm	853 ppm
Site 1171	-0.4	-0.5	-0.4	-0.2	-0.3
Site 761	0.0	-0.1	-0.2	-0.3	-0.2

Supplementary Table S4. Simulated deep water temperature changes (°C) due to topographic changes estimated during the MMCT glaciation (anomaly between ICE_{FULL}55m and ICE_{FULL}1m).

F. Sensitivity to orbital configuration

In further orbital forcing sensitivity tests (refer to Methods), we find a minimal effect on DWT: the anomaly between extreme Southern Hemisphere warm and cold orbit conditions is just 0.2-0.3°C (Supplementary Figure S63). In the ICE_{FREE} extreme cold orbit scenario, interior continental temperatures become cold enough to likely support an ice sheet. Coastal surface temperatures, however, remain above zero meaning that snowfall melts, runoff occurs and our mechanism reducing AABW production still operates. DWT changes in the extreme warm orbit ICE_{FULL}55m scenario relate to significant sea ice reductions (not shown).

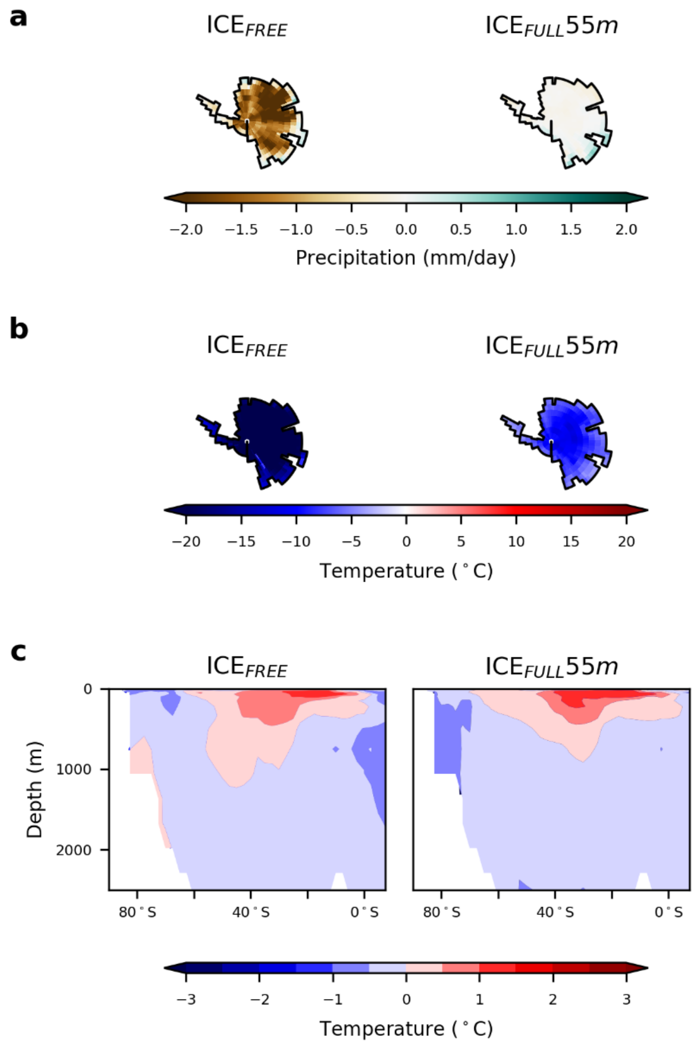

Supplementary Figure S63. Simulated atmospheric and oceanographic conditions in response to changes in orbital configuration for different Antarctic ice sheet configurations. **(a)** Antarctic summer (DJF) precipitation, **(b)**, Antarctic summer air temperature, **(c)**, Annual mean Southern Hemisphere meridional mean ocean temperature. The left panels show the model results for the anomaly between the extreme cold orbit configuration and the extreme warm orbit configuration for an ice-free Antarctica. The right panels show the model results for the anomaly between the extreme cold orbit configuration and the extreme warm orbit configuration for 55m sea level equivalent scenario. Refer to Fig. 2 for more details of the boundary conditions used.

G. A potential mechanism for asynchronous advance of different ice sheet catchments

Major ice advance onto the continental shelf in the Ross Sea[21,36] occurred at the same time as the presence of open water and woody vegetation in the Wilkes Land[13] during the MCO (locations shown in Supplementary Figure S64). Although our climate model resolution is too coarse to examine these catchments in detail, our mechanism could provide an explanation for both of these records. On the basis of inference from our model results, and from discussions with a Chief Operational Meteorologist from the Met Office, we suggest that a) the warm vegetated Wilkes Land could have caused the grounded ice sheet in the Ross Sea and that b) a large ice sheet in the Ross Sea could have helped to maintain the vegetated Wilkes Land. We have shown in our model results how the presence of a warm vegetated Antarctic surface will draw moisture in from the Southern Ocean (Fig. 5c). If this warm moist air is drawn in over the Wilkes Land, when reaches the Transantarctic Mountains, it would likely lift and fall as snow into the Ross Sea catchments. Cold katabatic winds could then form from the top of the Transantarctic Mountains and flow over the growing Ross Sea sector ice sheet and complete the localized circulation of air. As ice in one catchment retreats, therefore, ice in another could advance, and vice versa. The resolution of the data from Site U1356 in the Wilkes Land[13] is not sufficient to compare directly with the extreme shifts in environmental motif documented in the AND-2A core in the Ross Sea between ~16.4 and 15.9 Ma[21]. However, changes in the extent of ice cover in the Wilkes Land vicinity could have been the trigger. Although evidence from other coastal catchments during the MCO is limited, we further suggest that such inter-catchment relationships could have also existed elsewhere since ice sheet advance requires a moisture supply, which our mechanism can provide. The record from Site 1171 in the Southern Ocean shows periods of ice sheet advance coincident with the warmest deep ocean temperatures[5], which we infer from our model results to indicate large ice-free vegetated areas, not just that of the Wilkes Land. Higher resolution modelling than performed in the present study would be needed to confirm or reject these ideas.

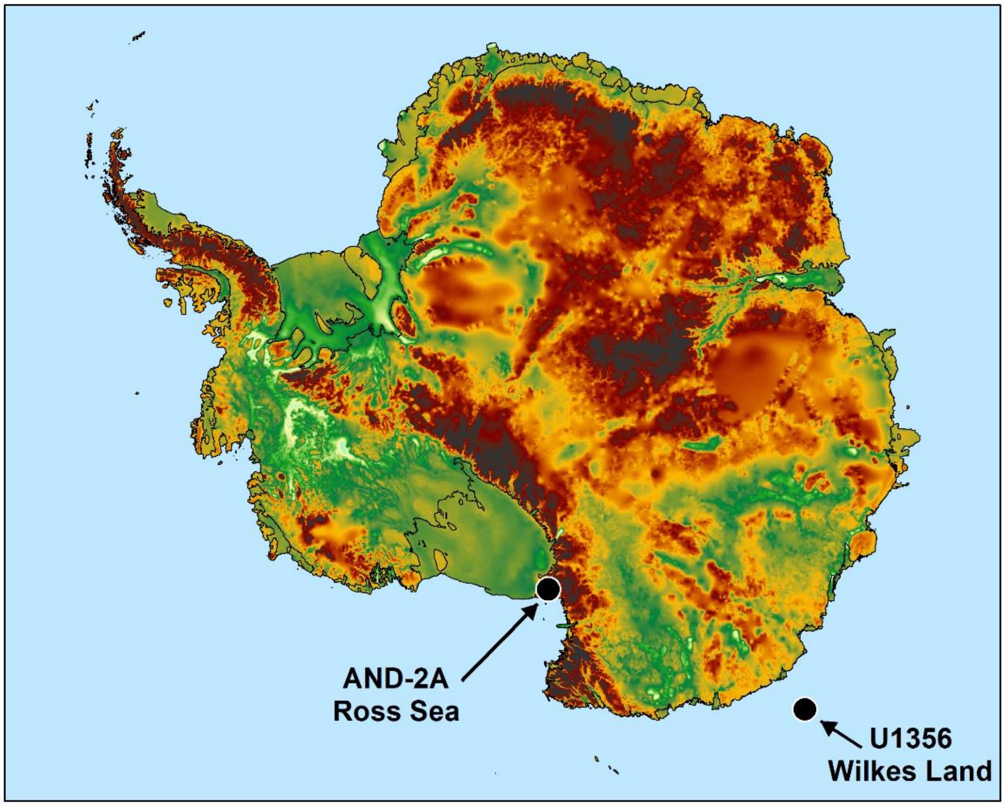

Supplementary Figure S64. Location of core sites. Basemap shown is the bed elevation from Bedmap2[38]

H. Model spinup

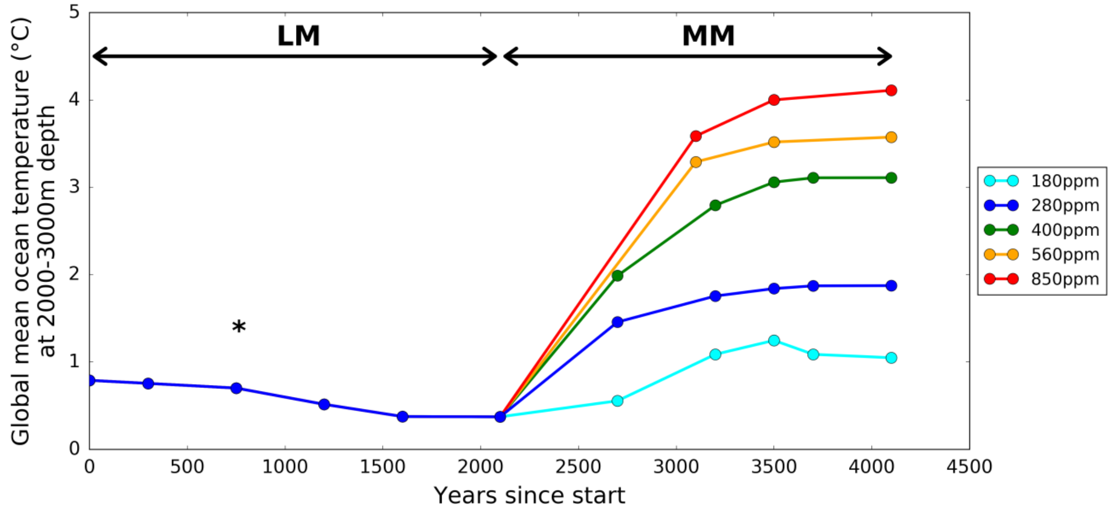

Supplementary Figure S65. Deep ocean temperature evolution through the simulations for the 0m sea level equivalent ice sheet Antarctic boundary condition. LM =late Miocene boundary conditions[4], MM=middle Miocene boundary conditions (refer to Fig. 2). *The change in the deep ocean temperatures under the late Miocene boundary conditions at this step in the simulations is as a result of a significant change in the overall model setup onto a different computer.

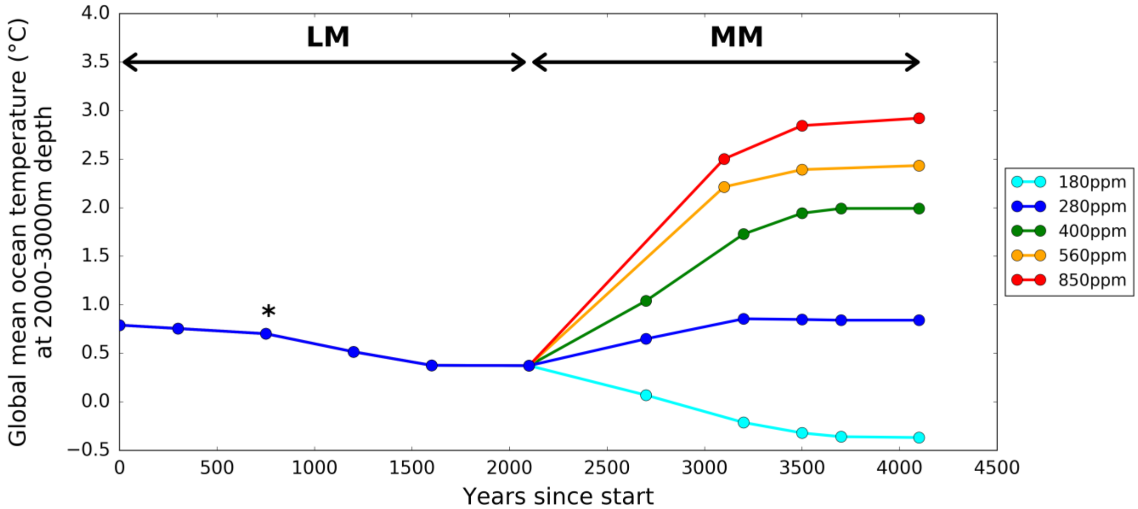

Supplementary Figure S66. Deep ocean temperature evolution through the simulations for the 1m sea level equivalent ice sheet Antarctic boundary condition. LM =late Miocene boundary conditions[4], MM=middle Miocene boundary conditions (refer to Fig. 2). *The change in the deep ocean temperatures under the late Miocene boundary conditions at this step in the simulations is as a result of a significant change in the overall model setup onto a different computer.

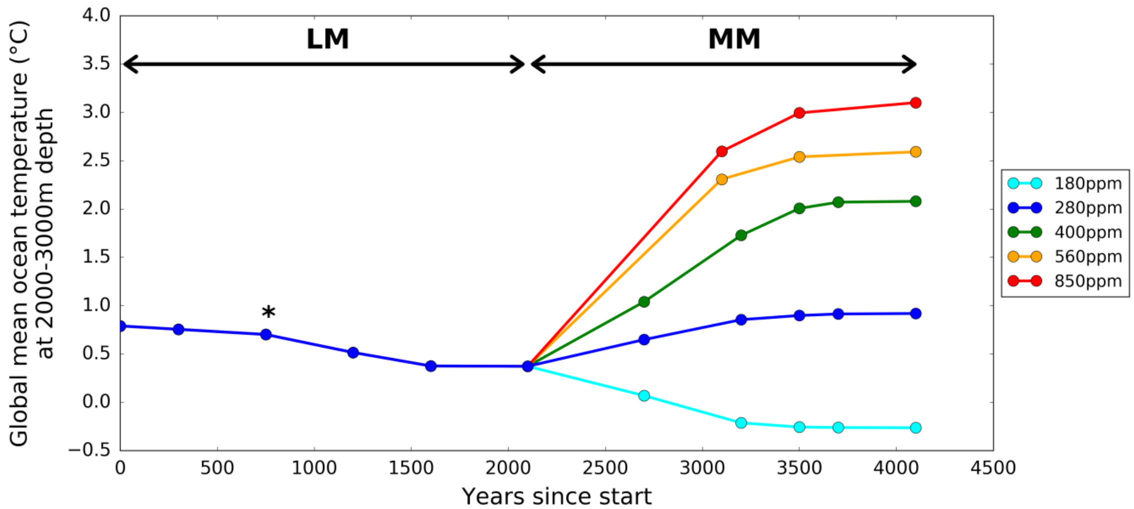

Supplementary Figure S67. Deep ocean temperature evolution through the simulations for the 55m sea level equivalent ice sheet Antarctic boundary condition. LM =late Miocene boundary conditions[4], MM=middle Miocene boundary conditions (refer to Fig. 2). *The change in the deep ocean temperatures under the late Miocene boundary conditions at this step in the simulations is as a result of a significant change in the overall model setup onto a different computer.

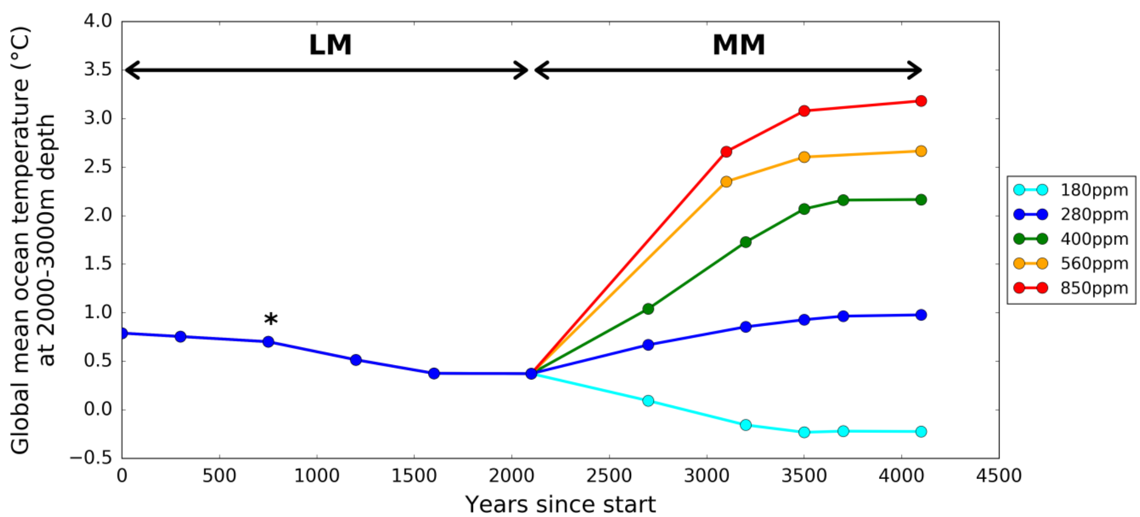

Supplementary Figure S68. Deep ocean temperature evolution through the simulations for the 90m sea level equivalent ice sheet Antarctic boundary condition. LM =late Miocene boundary conditions[4], MM=middle Miocene boundary conditions (refer to Fig. 2). *The change in the deep ocean temperatures under the late Miocene boundary conditions at this step in the simulations is as a result of a significant change in the overall model setup onto a different computer.

S3. Supplementary Information References

1. Bradshaw, C. D., Lunt, D. J., Flecker, R. & Davies-Barnard, T. Disentangling the roles of late Miocene palaeogeography and vegetation--Implications for climate sensitivity. *Palaeogeogr. Palaeoclimatol. Palaeoecol.* **417**, 17–34 (2015).

2. Bradshaw, C. D. *et al.* The relative roles of CO_2 and palaeogeography in determining late Miocene climate: results from a terrestrial model-data comparison. *Clim. Past* **8**, 715–786 (2012).

3. Goldner, A., Herold, N. & Huber, M. The Challenge of Simulating the Warmth of the Mid-Miocene Climatic Optimun in CESM1. *Clim. Past* (2014).

4. Markwick, P. J. The palaeogeographic and palaeoclimatic significance of climate proxies for data-model comparisons. in *Deep-Time Perspectives on Climate Change: Marrying the Signal from Computer Models and Biological Proxies* 251–312 (The Geological Society, 2007).

5. Shevenell, A. E., Kennett, J. P. & Lea, D. W. Middle Miocene ice sheet dynamics, deep-sea temperatures, and carbon cycling: A Southern Ocean perspective. *Geochemistry, Geophys. Geosystems* **9**, (2008).

6. Elderfield, H., Yu, J., Anand, P., Kiefer, T. & Nyland, B. Calibrations for benthic foraminiferal Mg/Ca paleothermometry and the carbonate ion hypothesis. *Earth Planet. Sci. Lett.* **250**, 633–649 (2006).

7. Gray, W. R. & Evans, D. Nonthermal influences on Mg/Ca in planktonic foraminifera: a review of culture studies and application to the Last Glacial Maximum. *Paleoceanogr. Paleoclimatology* **34**, 306–315 (2019).

8. Lear, C. H., Mawbey, E. M. & Rosenthal, Y. Cenozoic benthic foraminiferal Mg/Ca and Li/Ca records: Toward unlocking temperatures and saturation states. *Paleoceanography* **25**, (2010).

9. Lear, C. H. *et al.* Neogene ice volume and ocean temperatures: Insights from infaunal

foraminiferal Mg/Ca paleothermometry. *Paleoceanography* **30**, 1437–1454 (2015).

10. You, Y., Huber, M., Müller, R. D., Poulsen, C. J. & Ribbe, J. Simulation of the middle Miocene climate optimum. *Geophys. Res. Lett.* **36**, (2009).

11. Herold, N., Huber, M., Müller, R. D. & Seton, M. Modeling the Miocene climatic optimum: Ocean circulation. *Paleoceanography* **27**, (2012).

12. Passchier, S. *et al.* Early Eocene to middle Miocene cooling and aridification of East Antarctica. *Geochemistry, Geophys. Geosystems* **14**, 1399–1410 (2013).

13. Sangiorgi, F. *et al.* Southern Ocean warming and Wilkes Land ice sheet retreat during the mid-Miocene. *Nat. Commun.* **9**, 317 (2018).

14. Feakins, S. J., Warny, S. & Lee, J.-E. Hydrologic cycling over Antarctica during the middle Miocene warming. *Nat. Geosci.* **5**, 557 (2012).

15. Super, J. R. *et al.* North Atlantic temperature and pCO_2 coupling in the early-middle Miocene. *Geology* **46**, 519–522 (2018).

16. Zhang, Y. G., Pagani, M., Liu, Z., Bohaty, S. M. & DeConto, R. A 40-million-year history of atmospheric CO_2. *Philos. Trans. R. Soc. A Math. Phys. Eng. Sci.* **371**, 20130096 (2013).

17. Scheiner, F., Holcová, K., Milovsk\`y, R. & Kuhnert, H. Temperature and isotopic composition of seawater in the epicontinental sea (Central Paratethys) during the Middle Miocene Climate Transition based on Mg/Ca, $\delta^{18}O$ and $\delta^{13}C$ from foraminiferal tests. *Palaeogeogr. Palaeoclimatol. Palaeoecol.* **495**, 60–71 (2018).

18. Rousselle, G., Beltran, C., Sicre, M.-A., Raffi, I. & De Rafélis, M. Changes in sea-surface conditions in the Equatorial Pacific during the middle Miocene--Pliocene as inferred from coccolith geochemistry. *Earth Planet. Sci. Lett.* **361**, 412–421 (2013).

19. Shevenell, A. E., Kennett, J. P. & Lea, D. W. Middle Miocene southern ocean cooling and Antarctic cryosphere expansion. *Science (80-.).* **305**, 1766–1770 (2004).

20. Leutert, T. J., Auderset, A., Martínez-García, A., Modestou, S. & Meckler, A. N. Coupled Southern Ocean cooling and Antarctic ice sheet expansion during the middle Miocene.

Nat. Geosci. (2020). doi:10.1038/s41561-020-0623-0

21. Levy, R. *et al.* Antarctic ice sheet sensitivity to atmospheric CO_2 variations in the early to mid-Miocene. *Proc. Natl. Acad. Sci.* **113**, 3453–3458 (2016).

22. Sosdian, S. M. *et al.* Constraining the evolution of Neogene ocean carbonate chemistry using the boron isotope pH proxy. *Earth Planet. Sci. Lett.* **498**, 362–376 (2018).

23. Foster, G. L., Lear, C. H. & Rae, J. W. B. The evolution of pCO_2, ice volume and climate during the middle Miocene. *Earth Planet. Sci. Lett.* **341**, 243–254 (2012).

24. Kuhnert, H., Bickert, T. & Paulsen, H. Southern Ocean frontal system changes precede Antarctic ice sheet growth during the middle Miocene. *Earth Planet. Sci. Lett.* **284**, 630–638 (2009).

25. Super, J. R., Thomas, E., Pagani, M. & Huber, M. Miocene Evolution of North Atlantic Sea Surface Temperature. *Paleoceanogr. Paleoclimatology* **Accepted**, (2020).

26. Kochhann, K. G. D., Holbourn, A., Kuhnt, W. & Xu, J. Eastern equatorial Pacific benthic foraminiferal distribution and deep water temperature changes during the early to middle Miocene. *Mar. Micropaleontol.* **133**, 28–39 (2017).

27. Billups, K. & Schrag, D. P. Paleotemperatures and ice volume of the past 27 Myr revisited with paired Mg/Ca and $^{18}O/^{16}O$ measurements on benthic foraminifera. *Paleoceanography* **17**, 1–3 (2002).

28. Knorr, G. & Lohmann, G. Climate warming during Antarctic ice sheet expansion at the Middle Miocene transition. *Nat. Geosci.* **7**, 376 (2014).

29. Via, R. K. & Thomas, D. J. Evolution of Atlantic thermohaline circulation: Early Oligocene onset of deep-water production in the North Atlantic. *Geology* **34**, 441–444 (2006).

30. Davies, R., Cartwright, J., Pike, J. & Line, C. Early Oligocene initiation of North Atlantic deep water formation. *Nature* **410**, 917 (2001).

31. Coxall, H. K. *et al.* Export of nutrient rich Northern Component Water preceded early

Oligocene Antarctic glaciation. *Nat. Geosci.* **11**, 190 (2018).

32. Poore, H. R., Samworth, R., White, N. J., Jones, S. M. & McCave, I. N. Neogene overflow of northern component water at the Greenland-Scotland Ridge. *Geochemistry, Geophys. Geosystems* **7**, (2006).

33. Cramer, B. S., Toggweiler, J. R., Wright, J. D., Katz, M. E. & Miller, K. G. Ocean overturning since the Late Cretaceous: Inferences from a new benthic foraminiferal isotope compilation. *Paleoceanography* **24**, (2009).

34. Cortese, G., Gersonde, R., Hillenbrand, C.-D. & Kuhn, G. Opal sedimentation shifts in the World Ocean over the last 15 Myr. *Earth Planet. Sci. Lett.* **224**, 509–527 (2004).

35. Gasson, E., DeConto, R. M., Pollard, D. & Levy, R. H. Dynamic Antarctic ice sheet during the early to mid-Miocene. *Proc. Natl. Acad. Sci.* **113**, 3459–3464 (2016).

36. Colleoni, F. *et al.* Spatio-temporal variability of processes across Antarctic ice-bed--ocean interfaces. *Nat. Commun.* **9**, 2289 (2018).

37. Modestou, S., Leutert, T. J., Fernandez, A., Lear, C.H., Neckler, A.N. Warm middle Miocene Indian Ocean bottom water temperatures: comparison of clumped isotope and Mg/Ca records. *Paleoceanography and Paleoclimatology* **35(11)** e2020PA003927 (2020)

38. Fretwell, P., Pritchard, H.D., Vaughan, D.G., Bamber, J.L., Barrand, N.E., Bell, R., Bianchi, C., Bingham, R.G., Blankenship, D.D., Casassa, G. and Catania, G., Bedmap2: improved ice bed, surface and thickness datasets for Antarctica. *The Cryosphere*, **7(1)**, pp.375-393. (2013)